

MULTISPECTRAL SUPERCONDUCTING QUANTUM DETECTORS

FINAL REPORT

PERIOD OF PERFORMANCE 6-92 TO 8-95

CONTRACT No. DASG60-92-C-0140

AUGUST 1995

AUTHORS

NATHAN BLUZER and MARTIN G. FORRESTER

PRESENTED TO
UNITED STATES ARMY
STRATEGIC DEFENCE COMMAND
ADVANCED TECHNOLOGY DIRECTORATE (CSSD-AT-E)
P. O. BOX 1500
HUNTSVILLE, ALABAMA 35807

BY

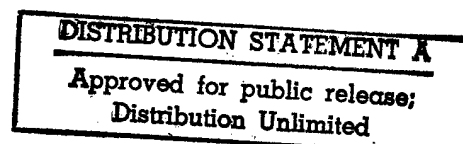
DTIC QUALITY INSPECTED 4

WESTINGHOUSE ELECTRIC CORPORATION
ADVANCED TECHNOLOGY CENTER
WINTERSON and NURSERY ROADS
LINTHICUM, MARYLAND 21090

PLEASE RETURN TO:

BMD TECHNICAL INFORMATION CENTER
BALLISTIC MISSILE DEFENSE ORGANIZATION
7100 DEFENSE PENTAGON
WASHINGTON D.C. 20301-7100

MSQD_IDOC



46020

REPRODUCTION QUALITY NOTICE

This document is the best quality available. The copy furnished to DTIC contained pages that may have the following quality problems:

- **Pages smaller or larger than normal.**
- **Pages with background color or light colored printing.**
- **Pages with small type or poor printing; and or**
- **Pages with continuous tone material or color photographs.**

Due to various output media available these conditions may or may not cause poor legibility in the microfiche or hardcopy output you receive.



If this block is checked, the copy furnished to DTIC contained pages with color printing, that when reproduced in Black and White, may change detail of the original copy.

Accession Number: 6020

Publication Date: Aug 01, 1995

Title: Multispectral Superconducting Quantum Detectors

Personal Author: Bluzer, N.; Forrester, M.G.

Corporate Author Or Publisher: Westinghouse Electric Corp., Winterson & Nursery Rds., Linthicum MD

Descriptors, Keywords: Superconducting Quantum Photodetector Multispectral

Pages: 00100

Cataloged Date: Feb 12, 1996

Document Type: HC

Number of Copies In Library: 000001

Record ID: 40637

MULTISPECTRAL SUPERCONDUCTING QUANTUM DETECTORS

FINAL REPORT

PERIOD OF PERFORMANCE 6-92 TO 8-95

CONTRACT No. DASG60-92-C-0140

AUGUST 1995

AUTHORS

NATHAN BLUZER and MARTIN G. FORRESTER

PRESENTED TO
UNITED STATES ARMY
STRATEGIC DEFENCE COMMAND
ADVANCED TECHNOLOGY DIRECTORATE (CSSD-AT-E)
P. O. BOX 1500
HUNTSVILLE, ALABAMA 35807

BY

WESTINGHOUSE ELECTRIC CORPORATION
ADVANCED TECHNOLOGY CENTER
WINTERSON and NURSERY ROADS
LINTHICUM, MARYLAND 21090

Unclassified

SECURITY CLASSIFICATION OF THIS PAGE

REPORT DOCUMENTATION PAGE				
1a. Report Security Classification Unclassified		1b. Restrictive Markings		
2a. Security Classification Authority		3. Distribution/Availability of Report		
2b. Declassification/Downgrading Schedule				
4. Performing Organization Report Number (s)		5. Monitoring Organization report Numbers		
6a. Name of Performing Organization Westinghouse Electric Corp.	6b. Office Symbol (If applicable) Elec. Sys. Grp.	7a. Name of Monitoring Organization		
6c. Address (City, State and Zip Code) Winterson and Nursery Rds. Linthicum, MD 21090		7b. Address (City, State and Zip Code)		
8a. Name of Funding/Sponsoring Organization United States Army	8b. Office Symbol (If applicable)	9. Procurement Instrument Identification Number DASG60-92-C-0140		
8c. Address (City, State, and Zip Code) Strategic Defense Command (CSSD-H-D) P.O. Box 1500 Huntsville, AL 35807		10. Source of Funding Nos.		
		Program Element No.	Project No.	Task No.
11. Title (Include Security Classification) Multispectral Superconducting Quantum Detectors				
12. Personal Author(s) Nathn Bluzer and Martin G. Forrester				
13a. Type of Report Technical, Final	13b. Time Covered 6/92 - 8/95	14. Date of Report (Yr,Mo, Day) August 1995	15. Page Count	
16. Supplementary Notation				
17. Cosatl Codes			18. Subject Terms (Continue on reverse if necessary and identify a block number. Superconducting, Quantum Photodetectors	
Field	Group	Sub. Gr.		
19. Abstract (Continue on reverse if necessary and identify by block number. A superconducting quantum photodetector is described and analyzed. The YBCO photodetector and YBCO readout SQUID form an integrated circuit. The photoresponse is based on the Kinetic Inductance of the superconducting condensate. Predicted value for NEP $\approx 10^{-15}$ Watt/√Hz.				
20. Distribution/Availability of Abstract Unclassified/Unlimited <input checked="" type="checkbox"/> Same as Rpt. <input type="checkbox"/> DTIC Users <input type="checkbox"/>		21. Abstract Security Classification Unclassified		
22a. Name of Responsible Individual Mr. Dimitrios Lianos	22b. Telephone Number (Include Area Code) (202) 955-3223	22c. Office Symbol CSSD-M-D		

Unclassified

SECURITY CLASSIFICATION OF THIS PAGE

MULTISPECTRAL SUPERCONDUCTING QUANTUM PHOTODETECTORS

1.0	Executive Summary	1
2.0	Quantum Superconducting Kinetic Inductance Photodetectors	3
2.1	Background	3
2.2	Theory of Operations	5
2.2.1	The QSKIP Energy Minimum	8
2.2.2	The QSKIP Photoresponse	11
2.2.2.1	Photocurrent Calculations	12
2.2.2.2	Photoinduced Quasiparticle Population ΔN_Q	14
2.2.2.3	Effective Quasiparticle Lifetime	17
2.2.3	Noise Level in QSKIP	20
2.2.4	QSKIP Performance Characteristics	24
2.2.5	YBCO QSKIP Responsivity and Frequency Bandwidth	25
2.2.6	Sensitivity of a YBCO QSKIP Sensor	26
2.2.6.1	Noise in QSKIP	29
2.2.6.2	Electronic removal of DC Offsets, SQUID Nonlinearities, and 1/f Noise	30
2.2.6.3	YBCO QSKIP Noise Equivalent Power	31
2.2.7	Competing LWIR Semiconductor Based Quantum Detectors	33
2.2.8	Conclusions on Operation of QSKIP	36
2.3	Detector Fabrication	37
2.3.1	Magnetically Coupled Detector	37
2.3.2	Directly Coupled Detector	41

2.4	References	42
3.0	Experimental Approach and Measurements	48
3.1	Optical Setup	48
3.2	Electrical Setup	57
3.3	Cryogenic Setup	64
3.4	Detector Packaging	68
3.5	Detector Testing and Results	73
4.0	Published/Submitted Papers	80
4.1	Photoresponse Mechanisms of Thin Superconducting Films and Superconducting Detectors	
4.2	Superconducting Quantum Detectors	
4.3	Superconducting Quantum Detectors in YBCO	
4.4	Quantum Detectors in Superconducting YBCO	

1.0 EXECUTIVE SUMMARY

Infrared sensors offer the ability for passive detection of targets on earth, under ambient conditions, and in space, against a cold background. Hence, DoD has sponsored the development of very sensitive midwave and long wave infrared photodetectors. Theoretically, above 1K quantum photodetectors offer superior performance over thermal photodetectors (bolometers). Accordingly, much effort and development has gone into developing semiconductor based quantum detectors, including, PV and PC HgCdTe, InSb, Extrinsic Silicon, Platinum Silicides, and III-V quantum well detectors. These efforts reflect the technological difficulty and high cost of making IR photodetectors in semiconductors. With the discovery of high temperature superconductivity (HTS) efforts were started to use these new materials, with the expectation of realizing sensitive midwave and long wave Infrared quantum photodetectors. In particular, given the small energy gap of HTS relative to IR semiconductor materials, it follows that superconductor materials should produce photodetectors with longer cut-off wavelength.

This program was started with the goal of demonstrating multispectral quantum photodetectors with very long cut-off wavelength using the newly discovered HTS materials. Given the relative immaturity of the HTS field, we formulate a very simple detector structure. The formulated multispectral quantum photodetector (about $100 \times 100 \mu\text{m}$) is based on the kinetic inductance of a superconductor and thus is named a Quantum Superconducting Kinetic Inductance Photodetector (QSKIP). The performance of this QSKIP is analyzed in section 2.2. The analysis reveals that the QSKIP photoresponse will be limited by the Cooper pair binding energy 2Δ , believed to be about $32 \mu\text{m}$ for YBCO. The QSKIP photoresponse and sensitivity are computed

from the minimum of the Hamiltonian energy functional and *linearized* Rothwarf-Taylor equations. Photoresponse and sensitivity expressions are computed in terms of the quasiparticle lifetime and indicate Background Limited Infrared Performance (BLIP) at very low photon flux levels. At low temperatures and under BLIP conditions, the photoresponse is proportional to the number of absorbed photons. Operating the QSKIP in the Meissner state and below 50% of I_C will limit the noise sources primarily to fluctuations in the condensate population. The Noise Equivalent Power for a YBCO QSKIP is dependent on the characteristic lifetimes for quasiparticle generation, quasiparticle recombination, anharmonic phonon decay, and phonon trapping in a BCS type superconductor. A Noise Equivalent Power estimate for a YBCO QSKIP is about 2.5×10^{-15} Watts/ $\sqrt{\text{Hz}}$ at 9K for a 10 μsec quasiparticle lifetime. With longer quasiparticle lifetimes and/or lower noise SQUID readout circuits, the projected NEP should directly improve.

The QSKIP fabrication is described in section 2.3. The experimental approach and measurements of the QSKIP are presented in section 3.0. To minimize development and fabrication risk, we decided to use a YBCO photodetector with a YBCO SQUID readout circuit, made on a bicrystal substrate. A generic experimental set up was developed for measuring photoresponse of superconducting photodetectors from 1 μm -100 μm over a very wide temperature range (5-300K) and this is presented in sections 3.1 through 3.4.

We have made and measured the characteristics of YBCO grain boundary SQUIDs, which operated at 5K with a critical current of about 60 μA . The YBCO photodetector material was superconducting with a reduced transition temperature. The as deposited YBCO had a transition temperature of about 90K and this was reduced to about 60K after the addition of a SiO_2 insulator needed to electrically isolate the QSKIP wiring. We have investigated the cause of reduction in the

transition temperature and concluded that the silicon dioxide insulators are leaching oxygen and poisoning the YBCO. Reoxygenation of the YBCO did not recover the 90K transition temperature. It is concluded that the quasiparticle lifetime in the processed YBCO was too degraded to show photoresponse. We are in the process of replacing the silicon dioxide insulator with epitaxial SrTiO_3 . This work is continuing on Westinghouse IR&D with the expectation that the new QSKIP structure will demonstrate excellent sensitivity over a very wide spectral range.

2.0 QUANTUM SUPERCONDUCTING KINETIC INDUCTANCE PHOTODETECTORS

In this chapter we provide a theoretical framework for superconducting quantum photodetectors and introduce a photodetector structure suitable for making superconducting quantum photodetectors.

2.1 BACKGROUND

The development of photodetectors is a very active area of research, covering a very broad spectral band, from γ -ray all the way up to very long wave infrared. The operating conditions and performance of photodetectors operating in these bands varies according to the photodetector materials, photodetection method, and the operating spectrum. Of particular interest are photodetectors operating in the midwave 3-5 μm (MWIR) and longwave 8-12 μm (LWIR) infrared spectra. Interest in these spectral bands is large because: (1) the atmosphere is transparent in these spectral bands, and (2) objects at 300K produce significant black body photon radiation in the MWIR and LWIR spectral bands. With a significant black body photon radiation, passive night imaging and target discrimination are possible, making MWIR and LWIR sensors very important for DoD and commercial applications.

Detectors fall into two broad categories:^{1,2} (1) thermal photodetectors and (2) quantum photodetectors. Thermal photodetectors absorb the incident photon flux energy with an optically "black" coating and hence are sensitive over a very broad spectral band. Thermal photodetectors are equilibrium photodetectors where the lattice and the electrons are in thermal equilibrium. The properties of the photodetector are very temperature dependent and photoabsorption produces a temperature change that generates a signal. Quantum photodetectors require a minimum energy quantum to produce each photoexcitation and photons with energy smaller than this minimum value are not detected, i.e. quantum photodetectors have a limited spectral photoresponse. Quantum photodetectors are nonequilibrium photodetectors where the electrons are not in thermal equilibrium with the lattice. The photodetector properties are not very temperature dependent and photoabsorption produces quantum excitations in the electronic states and thus a photosignal. Theoretically, above 1K, quantum photodetectors are more sensitive than thermal photodetectors because the noise level in quantum photodetectors is smaller. The noise in quantum photodetectors corresponds to Poisson fluctuations in the number of absorbed photons, whereas the noise in thermal photodetectors corresponds to fluctuations in the absorbed energy. This basic difference in noise mechanism can make quantum photodetectors potentially 10^5 more sensitive than thermal photodetectors.

The pursuit of better quantum photodetectors has been an ongoing endeavor. Just before the discovery of High Temperature Superconductivity (HTS), Enomoto and Murakami³ made photoresponse measurements on granular $\text{BaPb}_{0.7}\text{Bi}_{0.3}\text{O}_3$, and reported encouraging results. After the discovery of HTS by Bednorz and Muller⁴ in 1986, many proposals were offered for applying the new discovery to infrared (IR) detectors operating at liquid nitrogen temperatures. More

experimental results^{5,6,7,8,9,10,11} followed reporting on the photoresponse of various HTS detector structures. Forrester et al.¹² showed that the reported photoresponse signals were consistent with a bolometric response. However, because of technological limitations in existing semiconductor based quantum detectors, in particular beyond 12 μ m, the search for a superior superconducting detector persists.^{13,14,15} The cited approaches for realizing superconducting detectors have limitations that include poor area efficiency¹⁵ (or quantum efficiency), complicated readout circuits,¹⁴ and complicated¹⁶ photodetection mechanism.¹³ To overcome these limitations, a simple detector structure and readout circuit are needed. These issues were addressed in this program and are reported on in this final report.

2.2 THEORY OF OPERATION

We describe a detector structure which overcomes the aforementioned limitations and is projected to achieve Background Limited Infrared Performance (BLIP) for very low background radiation with an NEP of $\approx 10^{-15}$ Watts/ $\sqrt{\text{Hz}}$ for a 10 μ sec quasiparticle lifetime. The detectors photoresponse is based on the Cooper pairs' kinetic inductance and hence the label: Quantum Superconducting Kinetic Inductance Photodetector¹⁷ (QSKIP). *This detector's photoresponse is sensitive to photoinduced changes in the total Cooper pair population and is unlike Josephson junction based above-gap detectors that are only sensitive to changes in the condensate population within a coherence distance ξ from the Josephson junction.*

The QSKIP is intended to operate at: (1) low temperatures, (2) low background radiation, (3) below H_{C1} or in the Meissner state, (4) below 50% of the superconducting critical current I_C , (5) under static nonequilibrium conditions (achieved with constant photoillumination), and (6) not under pulsed laser radiation, as reported in many experiments^{5,6,7} The reasons for choosing such

operating conditions are several. In quantum detectors, the photoresponse increases with the effective quasiparticle lifetime. The effective quasiparticle lifetime is maximized by operating at low temperature and near thermal equilibrium. The lowest detector noise is achieved by operating below H_{C1} and at low temperatures ($T/T_C < 0.1$) because noise from the formation and movement of fluxons is severely inhibited. Finally, we predict excellent performance for the QSKIP when operating in a low background environment, i.e. detection of cold objects ($< 200K$) against a cold background ($< 200K$)

The QSKIP detector is made from a simple superconducting film patterned into a closed loop with input and output current leads. To facilitate the photoresponse and sensitivity calculation, the QSKIP is represented by a circular loop^{18,19} illustrated in Figure 2.1. For maximum coupling efficiency and sensitivity, the readout SQUID is directly coupled¹⁸ with the QSKIP, see Figure 2.2. In operation, the QSKIP is biased by a constant dc current I_0 , $I_0 < 0.5 I_C$. Current I_0 is divided by the QSKIP circuit into currents I_1 and I_2 . With photoabsorption, the division of I_0 into I_1 and I_2 changes and this change represents the QSKIP response.

The current division in the QSKIP is calculated from the minimum of the superconductor energy functional, the Hamiltonian. The condensate's Hamiltonian is expressed in terms of the operating currents, I_1 and I_2 , and the Cooper pair densities $\rho_{CP}(X)$, approximated to be constant and equal to ρ_{CP1} and ρ_{CP2} in branches 1 and 2, respectively. After incorporating the vector potential $A(X)$ into the Hamiltonian, we calculate the energy extrema in terms of currents I_1 and I_2 and under thermal equilibrium or static nonequilibrium conditions (achieved with constant photoillumination). Photoabsorption of a constant photon flux in only one branch reduces the number of Cooper pairs in that branch from the thermal equilibrium level, and this represents a new static nonequilibrium state

for the number of quasiparticles in that branch. With each new level of photoillumination, the current division changes in response to the new static nonequilibrium conditions (or number of quasiparticles in the illuminated branch). The QSKIP's performance is computed in terms of the Noise Equivalent Power²⁰ (NEP) that is calculated by combining the photoresponse expressions with equations representing the noise.

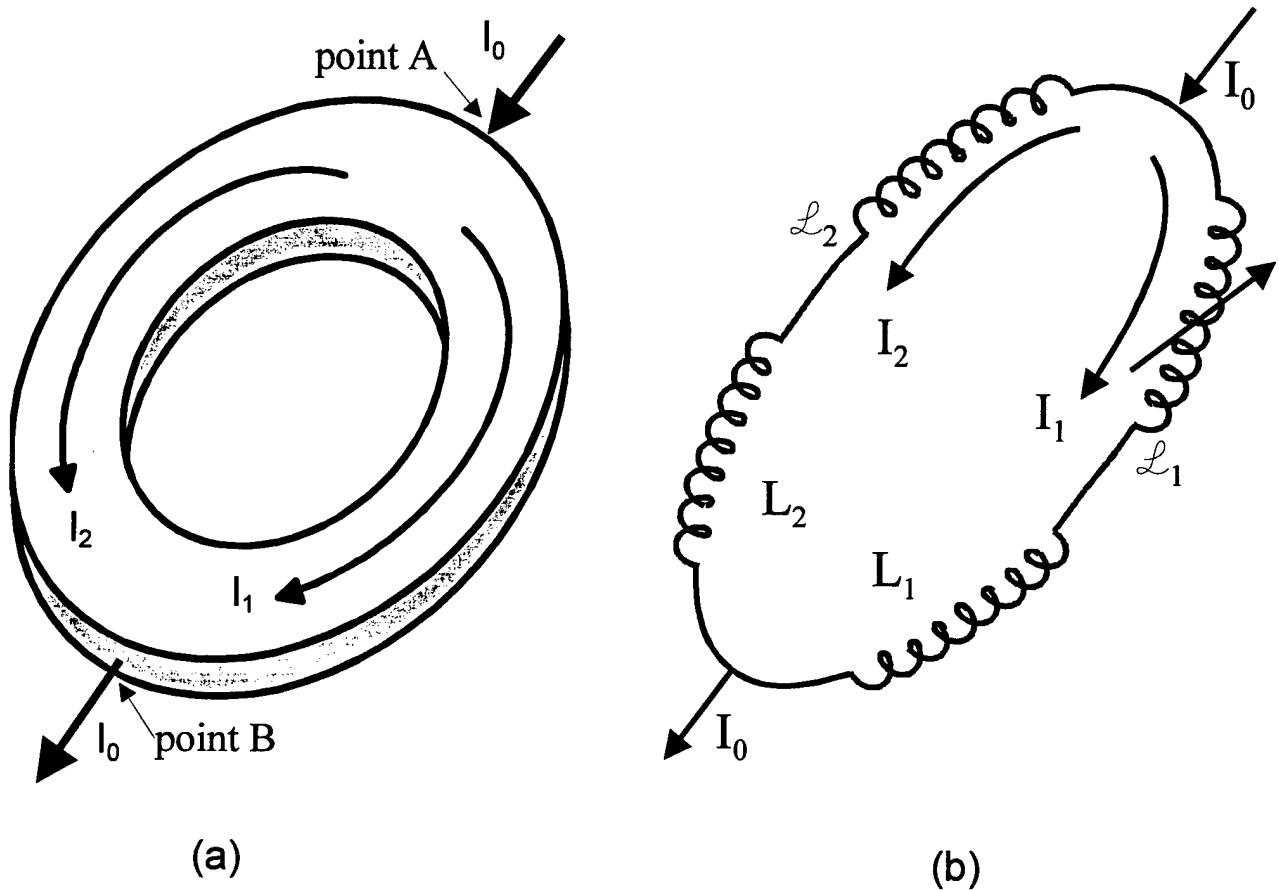


Figure 2.1. A superconducting loop (a), thinner than the London penetration depth, is subjected to a bias current I_0 injected at point "A" and removed at point "B". The bias current I_0 is divided into currents I_1 and I_2 flowing in branches 1 and 2, respectively. The equivalent circuit (b) contains the magnetic ($L_1 = L_{11} - M_{12}$, $L_2 = L_{22} - M_{12}$) and kinetic (l_1, l_2) inductance terms for branches 1 and 2, respectively. The self and mutual magnetic inductances are, respectively, represented by (L_{11} , L_{22}) and ($M_{12} = M_{21}$). l_1 is represented as a variable inductor to indicate changes caused by photoabsorption in branch 1.

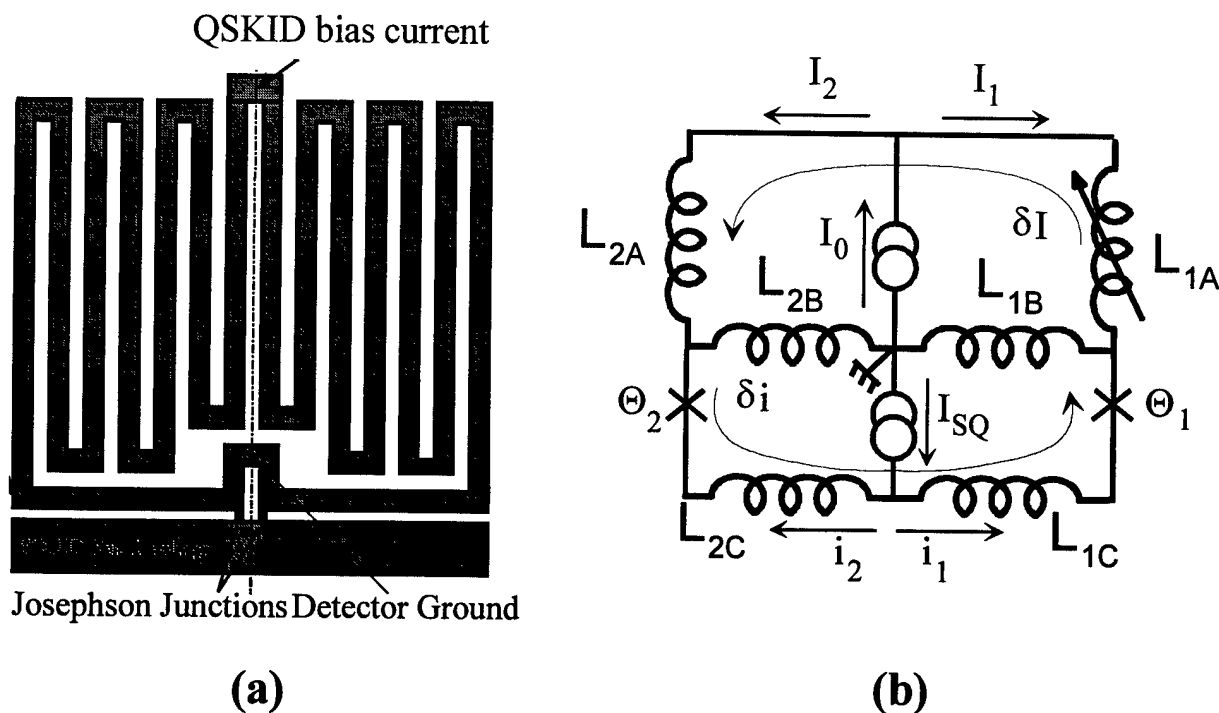


Figure 2.2. The YBCO QSKIP¹⁸ (a) is shaped into a serpentine pattern to increase its kinetic inductance and improve isolation against quasiparticle diffusion between the two branches. The readout SQUID is directly coupled to the QSKIP at the bottom. The photon flux only illuminates the right half of the QSKIP. The equivalent circuit (b) for the symmetrical QSKIP and readout SQUID represents the kinetic and magnetic inductances for branches 1 and 2. The QSKIP is biased with a dc current I_0 and the SQUID is biased with a dc current i_{SQ} .

2.2.1 THE QSKIP ENERGY MINIMUM

The QSKIP ring, illustrated in Fig. 2.1, receives a dc bias current I_0 , at point A, and divides it into currents I_1 and I_2 , in branches one and two, respectively, and I_0 exits at point B. The total energy of the condensate, E_{QSKIP} , is computed by integrating the energy of each pair over the pair density $\rho_{CP}(X)$ and the QSKIP volume $2V$. The value of currents I_1 and I_2 satisfy the energy extrema of the superconductor's Hamiltonian, \mathcal{H} , operating on the condensate, represented by a wave

function Ψ . The Hamiltonian written in terms of canonical momentum²¹ (the squared term in Eq. 1) and the Cooper pairs interacting potential (last term) is:

$$\mathcal{H} = \frac{1}{2m_{CP}} [\mathbf{p}(X) + q_{CP} \mathbf{A}(X)]^2 + q_{CP} \Phi(X) + q_{CP} V_{CP}(X) \quad (1)$$

where $\mathbf{p}(X) = m_{CP} \mathbf{v}$ is the kinetic momentum, $\mathbf{A}(X)$ is the vector potential generated by the current flow, $V_{CP}(X)$ is the attractive potential for a Cooper pair at X , $\Phi(X)$ is the electrostatic potential energy, q_{CP} is the electric charge for a pair and m_{CP} is the mass of a pair. We simplify equation 1 by making use of the Coulomb²² gauge $\nabla \cdot \mathbf{A}(X) = 0$, and the so called London gauge²³ $\Lambda \mathbf{J}(X) = -\mathbf{A}(X)$, where $\Lambda = m_{CP} / [\rho_{CP}(X) q_{CP}^2]$ and $\mathbf{J}(X)$ is the current density in the superconductor.

The Hamiltonian in Eq. 1 is simplified to a form similar to the BCS Hamiltonian²⁴ i.e.,

$$\mathcal{H} = \frac{1}{2m_{CP}} [\mathbf{p}(X)]^2 + \frac{1}{2\rho_{CP}(X)} \mathbf{A}(X) \cdot \mathbf{J}(X) + q_{CP} \Phi(X) + q_{CP} V_{CP}(X) \quad (2)$$

We have used the expression $\mathbf{J}(X) = q_{CP} \rho_{CP}(X) \mathbf{p}(X) / m_{CP}$ to simplify equation 1 and obtain an expression for the Hamiltonian with two terms in addition to the BCS terms: the second term accounts for the energy present in a flowing superconducting current, while the last term with $\Phi(X)$ was eliminated by BCS²⁴ by solving the problem relative to the Fermi Energy, E_F . Unlike the first two terms, the last two terms in Eq. 2 are not a function of currents I_1 or I_2 and they will drop out when the energy minimum of the QSKIP is calculated relative to I_1 and I_2 .

The QSKIP energy, E_{QSKIP} , is obtained by integrating \mathcal{H} over the Cooper pair density $\rho_{CP}(X) = \Psi^* \Psi$ where this density spans the domain of the Hermitian operator \mathcal{H} . Incorporating

$\rho_{CP}(X)=\Psi^*\Psi$ and substituting $\mathbf{J}(X)=q_{CP}\rho_{CP}(X)\mathbf{p}(X)/m_{CP}$, into the Hamiltonian given by Eq. 2, the expression for the QSKIP energy E_{QSKIP} becomes:

$$E_{QSKIP} = \int_{2V} \Psi^* \nabla^2 \Psi d^3x = \frac{1}{2} \int_{2V} \mathbf{A}(\mathbf{X}) \cdot \mathbf{J}(\mathbf{X}) d^3x + \frac{1}{2} \int_{2V} \mathbf{A}(\mathbf{X}) \cdot \mathbf{J}(\mathbf{X}) d^3x + \int_{2V} \rho_{CP}(X) [\Phi(X) + V_{CP}(X)] d^3x \quad (3)$$

The energy in Equation 3 has three terms: (1) the first term represents the condensate's kinetic energy, (2) the second term represents the energy stored in the field²⁵ produced by a flowing supercurrent, and (3) the third term represents the potential energy terms.

Since the E_{QSKIP} energy minimum is calculated in terms of currents I_1 and I_2 [or the corresponding current densities $\mathbf{J}_1(X)$ and $\mathbf{J}_2(X)$] we need to express Equation 3 in terms of these. This is facilitated by doing the volume integration over branches 1 and 2. The first and last terms in Equation 3 will each yield an additional term while the middle term will yield three additional terms. The vector potential term expressed in terms of volume integral over branches 1 and 2 is:

$$\mathbf{A}(\mathbf{X}) = \left(\frac{\mu_0}{4\pi} \right) \int_{V_1} \frac{\mathbf{J}_1(\mathbf{Y})}{|\mathbf{X} - \mathbf{Y}|} d^3y + \left(\frac{\mu_0}{4\pi} \right) \int_{V_2} \frac{\mathbf{J}_2(\mathbf{Y})}{|\mathbf{X} - \mathbf{Y}|} d^3y \quad (4)$$

Incorporating these substitutions into Eq. 3, we obtain an equation for the QSKIP energy in terms of I_1 and I_2 and: the kinetic inductances (ℓ_i), the self magnetic inductances (L_{ij}), and the mutual magnetic inductances (M_{ij} for $i \neq j$), where the subscripts "i" and "j" refer to branches one or two, i.e.,

$$E_{QSKIP} = \frac{1}{2} \ell_1 I_1^2 + \frac{1}{2} \ell_2 I_2^2 + \frac{1}{2} L_{11} I_1^2 + \frac{1}{2} L_{22} I_2^2 + M_{12} I_1 I_2 + \int_{2V} \rho_{CP}(X) [\Phi(X) + V_{CP}(X)] d^3x \quad (5)$$

Where $\mathcal{L}_1 = (m_{CP}/q_{CP}^2)(l_1/(S_1\rho_{CP1}))$ [$\mathcal{L}_2=(m_{CP}/q_{CP}^2)(l_2/S_2\rho_{CP2})$] is the kinetic inductance of branch number one (two) with a Cooper pair density ρ_{CP1} [ρ_{CP2}], a cross sectional area S_1 (S_2) and a length l_1 (l_2). The self inductance of branch one (two) is labeled by L_{11} (L_{22}) and the mutual inductance between the branches is labeled as $M_{12}=M_{21}$, by symmetry.

The minimum of E_{QSKIP} is calculated by taking the differential of equation 5 with respect to I_1 and I_2 to yield,

$$\frac{\partial E_{QSKIP}}{\partial I_i} = [\mathcal{L}_1 + L_{11}]I_1 - [\mathcal{L}_2 + L_{22}]I_2 = 0 \quad (6)$$

We make use of the fact that the currents flowing in the QSKIP branches divide $I_0=I_1+I_2$ hence $\partial/\partial I_1=(\partial I_2/\partial I_1)(1/\partial I_2)= -\partial/\partial I_2$ and the magnetic inductance terms are combined into effective inductance terms: $L_1=L_{11}-M_{12}$ and $L_2=L_{22}-M_{12}$. It should be noted that for a symmetrical QSKIP $L_{11}=L_{22}$ and $M_{21}=M_{12}$. Equation 6 holds for any arbitrary value of Cooper pair density occurring for each level of constant photodepairing.

2.2.2 QSKIP PHOTORESPONSE

In this section we calculate the QSKIP photocurrent from the constraints governing the photodetectors operation (given by Equation 6). The photocurrent I_s is calculated first in terms of the change in kinetic inductance $\Delta\mathcal{L}_1$ (section 2.2.2.1). Next, using the modified Rothwarf-Taylor Equations, we calculate the change of $\Delta\mathcal{L}_1$ in terms of changes in the quasiparticle density ΔN_Q produced by photoabsorption (section 2.2.2.2). Finally, we relate the change in $\Delta\mathcal{L}_1$ to the quasiparticle effective lifetime described in section 2.2.2.3.

2.2.2.1 Photocurrent Calculations

The photoresponse signal, $I_s = I_1 - I_2$, is produced as the division of I_0 changes from $I_1 = I_2$ to $I_1 \neq I_2$ as one of the QSKIP branches is exposed to a constant level of illumination, and the currents change to satisfy the required *minimum energy* conditions. Without loss of generality, and for the sake of simplicity, we assume a totally symmetric QSKIP geometry, where, under no illumination and under thermal equilibrium, the Cooper pair density $\rho_{CP}(X)$ is the same in branches 1 and 2 producing a symmetric current division i.e. $I_1 = I_2 = I_0/2$. Hence, the thermal equilibrium signal current I_s^0 , and the associated magnetic flux Φ_B^0 inside the ring are zero. Photoabsorption in branch number 1 only breaks the QSKIP's symmetry in $\rho_{CP}(X)$ and produces a photosignal $I_s = I_1 - I_2$ and a corresponding net magnetic flux Φ_B inside the QSKIP's ring, where $\Phi_B = I_s(L_1 + L_2)$. Read-out of the photoinduced signal current I_s (for directly coupled) or Φ_B (for magnetically coupled) is by a SQUID.

The signal current I_s is produced by kinetic inductance changes $\Delta\ell_1$ caused by photoabsorption, in branch 1 only, of N_Φ photons with an average value of N_Φ^0 . The signal current consists of a circulating current I_s , causing a corresponding magnetic flux Φ_B . The signal photocurrent directly depends on $\Delta\ell_1$ and is computed by taking the differential of Eq. 6 to obtain:

$$I_s = \frac{\partial I_1}{\partial \ell_1} \Delta\ell_1 = \frac{-I_1}{[\ell_1 + L_1 + \ell_2 + L_2]} \Delta\ell_1 \quad (7)$$

Equation 7 is valid under static nonequilibrium conditions and when the quasiparticle density N_Q is much less than $\rho_{CP}(X)$. Using partial derivatives, the change in the kinetic inductance $\Delta\ell_1$ is expressed as:

$$\Delta \mathcal{L}_1 = \frac{\partial \mathcal{L}_1}{\partial \rho_{CP}(X)} \frac{\partial \rho_{CP}(X)}{\partial N_Q} \Delta N_Q \quad (8)$$

Explicit expressions for the partial derivative factors in Eq. 8 are obtained using Eq. 6, the definition of kinetic inductance given below Eq. 5, and the fact that each Cooper pair forms two quasiparticles ($\partial \rho_{CP}(X)/\partial N_Q = -1/2$). To complete the calculation for I_S , an explicit expression for ΔN_Q is needed that represents the photoinduced increase in the quasiparticle population in branch 1.

The total static nonequilibrium quasiparticle density N_Q is expressed as a sum of the thermal equilibrium quasiparticle density N_Q^{EQ} and the photoinduced increase in the quasiparticle density, $N_Q = \Delta N_Q + N_Q^{EQ}$. The thermal equilibrium quasiparticle density in each branch, based on a BCS superconductor at $T < 0.5 T_C$, is given by:²⁶

$$N_Q^{EQ} = 2N(0) \sqrt{\frac{\pi}{2} \Delta(T) k_B T} \exp\left(-\frac{\Delta(T)}{k_B T}\right) \quad (9)$$

where $N(0)$ is the density of states in volume and energy at the Fermi surface, k_B is Boltzmann's constant, T is the operating temperature in degrees Kelvin, and $\Delta(T)$ is the temperature dependent superconducting energy gap. An expression for the change in the quasiparticle density ΔN_Q from the thermal equilibrium value N_Q^{EQ} is obtained with a *modified* form of the Rothwarf-Taylor²⁷ equations.

2.2.2.2 Photoinduced Quasiparticle Population ΔN_Q

The Rothwarf-Taylor equations, 10 and 11, describe a superconductor in nonequilibrium in terms of: the quasiparticle density, N_Q , the pair breaking phonon density, N_Ω , and the absorbed photon flux density,²⁸ N_Φ , as:

$$\frac{dN_Q}{dt} = 2m_1 \eta N_\phi + \frac{2N_\Omega}{\tau_B} - R N_Q^2 \quad (10)$$

$$\frac{dN_\Omega}{dt} = \frac{R N_Q^2}{2} - \frac{N_\Omega}{\tau_B} - \left[\frac{1}{\tau_{ES}} + \frac{1}{\tau_{AH}} \right] [N_\Omega - N_\Omega^{EQ}] + 2m_2 \eta N_\phi, \quad (11)$$

where $R=1/[\tau_R^{EQ} N_Q^{EQ}]$, $1/\tau_R^{EQ}$ is the thermal equilibrium quasiparticle recombination rate, $1/\tau_B$ is the quasiparticle generation rate by pair breaking phonons (since only pair breaking phonons have sufficient energy $2\Delta(T)$ to break Cooper pairs). The phonon depletion occurs by: (1) pair breaking phonon escape into the substrate with rate $1/\tau_{ES}$, or (2) anharmonic rate decay of pair breaking phonons into multiple phonons (each with energy less than $2\Delta(T)$) with rate $1/\tau_{AH}$.

We have incorporated into the Rothwarf-Taylor equation the effects of photoabsorption of a photon density N_ϕ , acting with an internal quantum efficiency η . Specifically, each photoabsorbed photon, with energy $h\nu$, is thermalized by electron-electron and electron-phonon interactions. Quasiparticles directly photogenerated by electron-electron interactions^{29,30} are represented by the term $2m_1\eta N_\phi$, in Eq. 10. Quasiparticles generated by electron-phonon interactions³¹ are represented by $m_2\eta N_\phi$, in Eq. 11. The constants m_1 and m_2 represent, respectively, the number of quasiparticles and pair breaking phonons produced by each photoabsorbed photon^{32,33}. In these calculations we assume photons with energy ($h\nu$) much larger than 2Δ and the pair breaking phonons with energies ($h\Omega \geq 2\Delta$) which are related by an approximation $h\nu \approx m_1(2\Delta) + m_2(h\Omega)$. Here the Fano³⁴ factor has been neglected. Also for YBCO $\tau_{ES} \gg \tau_{AH}$. These equations are simplified into *linear algebraic* equations by invoking two operating conditions for the QSKIP.

First, under *static nonequilibrium conditions* on average $dN_Q/dt=dN_\Omega/dt=dN_\Phi/dt=0$. There are time fluctuations in the densities of N_Φ , N_Q , and N_Ω and they manifest themselves as noise in the QSKIP, and these are considered in Section 2.2.3. Here, we are only interested in the *average* values of N_Φ , N_Q , and N_Ω , and this simplifies Equations 10 and 11 into two nonlinear algebraic equations.

Second, the nonlinearity in the Rothwarf-Taylor equations is removed by explicitly expressing the R term, in equations 10 and 11, in terms of the *nonequilibrium* quasiparticle lifetime. The nonlinear term represents the quasiparticle recombination rate and is expressed as a product of N_Q^2 and R. The N_Q^2 term represents the number of ways a pair can be formed from N_Q quasiparticles. Specifically, for N_Q quasiparticles there are $N_Q(N_Q-1)/2$ ways of pairing and since each pairing removes two quasiparticles we obtain the N_Q^2 factor, for $N_Q \gg 1$. The term R represents the recombination rate for any two quasiparticles and this is not equal to the reciprocal of the equilibrium quasiparticle lifetime $1/\tau_R^{EQ}$, calculated by Kaplan et al.³⁵. Kaplan calculated the recombination rate, at thermal equilibrium, of a single quasiparticle with any one of the N_Q^{EQ} available quasiparticles. Thus at thermal equilibrium, the factor $R=1/[\tau_R^{EQ} N_Q^{EQ}]$, because if N_Q^{EQ} were left out from the denominator we would be double counting. Rothwarf and Taylor²⁷ incorporated into their equation the thermal equilibrium values for τ_R^{EQ} and N_Q^{EQ} , where τ_R^{EQ} can be taken from Kaplan.³⁵ However, since the QSKIP operates under static nonequilibrium conditions, instead of representing $R=1/[\tau_R^{EQ} N_Q^{EQ}]$ we use the more appropriate static nonequilibrium values for $R=1/[\tau_R N_Q]$, where τ_R and N_Q are, respectively, the static nonequilibrium values for the quasiparticle lifetime and density. This approach has the benefit of *linearizing* the Rothwarf-Taylor equations.

The solution for ΔN_Q is obtained by incorporating the above conditions into equations 10 and 11 and solving for N_Q to obtain:

$$N_Q = N_Q^{EQ} + (m_1 + m_2) \frac{\tau_{AH} \tau_{ES}}{\tau_{AH} + \tau_{ES}} \eta N_\phi \quad (12)$$

This indicates that photoabsorption increases the pair breaking phonon population beyond the thermal equilibrium number N_Q^{EQ} and the increase is directly proportional to the effective internal quantum efficiency $(m_1 + m_2)\eta$, the factor $(\tau_{ES} \tau_{AH})/(\tau_{ES} + \tau_{AH})$, and the photon density N_ϕ . Substituting Eq. 12 into Eq. 10 and simplifying by recognizing that $\tau_B \ll (\tau_{ES} \tau_{AH})/(\tau_{ES} + \tau_{AH})$, we obtain:

$$N_Q^{EQ} + \Delta N_Q = 2 \eta (m_1 + m_2) \left(\frac{\tau_{AH} \tau_{ES}}{\tau_{AH} + \tau_{ES}} \right) \frac{\tau_R}{\tau_B} N_\phi + 2 \frac{\tau_R}{\tau_B} N_Q^{EQ} \quad (13)$$

In Eq. 13, N_Q is replaced by $N_Q^{EQ} + \Delta N_Q$ to provide an expression for the change in quasiparticle density in terms of N_ϕ and N_Q^{EQ} . Equation 13 is valid only for nonequilibrium conditions where $N_Q > N_Q^{EQ}$ or $\Delta N_Q > 0$. This requirement is satisfied by replacing $2(\tau_R/\tau_B)N_Q^{EQ}$ by N_Q^{EQ} in Eq. 13, since under thermal equilibrium conditions, when $N_\phi = 0$, the nonequilibrium excess quasiparticle density $\Delta N_Q = 0$. Solving Eq. 13 for ΔN_Q and substituting this into Eq. 8 and combining with Eq. 7, the explicit expression for I_s becomes:

$$I_s = \frac{I_0}{4\rho_{CF}(X)} \frac{\mathcal{L}_1}{(\mathcal{L}_1 + \mathcal{L}_1)} \left[\eta (m_1 + m_2) \left(\frac{\tau_{AH} \tau_{ES}}{\tau_{AH} + \tau_{ES}} \right) \frac{\tau_R}{\tau_B} N_\phi \right] \quad (14)$$

The expression in the square brackets in Eq. 14 is for ΔN_Q . The photocurrent I_s depends on the effective quantum efficiency $[(m_1 + m_2)\eta]$, the effective quasiparticle lifetime

$\tau_R \tau_{AH} \tau_{ES} / [(\tau_{AH} + \tau_{ES}) \tau_B]$, and the photon density N_ϕ . The effective internal quantum efficiency term is made up of: (1) the internal photon absorption efficiency η within the superconductor, (2) the number of quasiparticles generated by electron-electron interaction (m_1), and (3) the number of quasiparticles generated by electron-phonon interactions (m_2). Thus each absorbed photon, with energy several times larger than 2Δ generates up to $h\nu/\Delta$ quasiparticles. As expected, the effective quasiparticle lifetime has a direct influence on determining the signal I_s and it is considered next.

2.2.2.3 Effective Quasiparticle Lifetime

We estimate the quasiparticle lifetime assuming a BCS type superconductor, based on “s” wave pairing. This is appropriate for low temperature superconductors but is presently unresolved for high temperature materials where the nature of the superconducting gap is still in question. It should be noted that calculations taking account of “d” and “s” wave pairing have been made by Sergeev and Reizer³⁶ (see section 4.1) with results similar to these calculations. It should also be noted that the QSKIP is intended to operate near thermal equilibrium and the quasiparticle lifetimes used are consistent with this assumption. Operating significantly away from thermal equilibrium is expected to decrease the effective quasiparticle lifetime and the photoresponse, leading to a nonlinear and compressive photoresponse. With these two caveats, we proceed to estimate the quasiparticle lifetime using a BCS model.

The intrinsic quasiparticle lifetime at thermal equilibrium τ_R^{EQ} is very sensitive to temperature and for a BCS superconductor at $T < 0.5T_C$ the intrinsic quasiparticle lifetime is given by Kaplan as:³⁵

$$\tau_R^{EQ}(T) = \frac{\tau_0}{\sqrt{\pi}} \left[\frac{k_B T_C}{2\Delta_0} \right]^{5/2} \left[\frac{T_C}{T} \right]^{1/2} \exp \left[\frac{\Delta_0}{k_B T} \right] \quad (15)$$

$$\approx 0.1 \tau_0 \exp \left[\frac{\Delta_0}{k_B T} \right] ,$$

where, for low temperature superconductors, a representative value for τ_0 calculated by Kaplan³⁵ et. al is approximately 10^{-11} seconds. Near thermal equilibrium we *estimate* that $\tau_R^{EQ} \approx \tau_R$. At a low temperatures of $T \approx 0.1T_C$, for a BCS superconductor ($\Delta_0 \approx 1.72 k_B T_C$), the computed intrinsic recombination lifetime (with Eq. 15) is very large ($\tau_R \approx 30 \mu\text{sec}$) and is much larger than τ_0 . If high temperature superconductors have a larger “s” type energy gap, even longer quasiparticle lifetimes can be expected. For example, in YBCO the energy gap inferred from specific heat measurements³⁷ is $\Delta_0 \approx 2.5 k_B T_C$ (instead of $\Delta_0 \approx 1.72 k_B T_C$ for a BCS gap), at $T \approx 0.1T_C$ the calculated intrinsic quasiparticle lifetime is even longer, or $\tau_R \approx 70 \text{msec}$.

In low temperature BCS type superconductors, experimental measurements confirm the exponential dependence of the quasiparticle lifetime, expressed by equation 15, on the superconductor's energy gap and the operating temperature. Effective quasiparticle lifetime measurements in aluminum,^{38,39,40} lead,^{41,42} and tin⁴³ show an exponential dependence represented by Equation 15. At low temperatures very long effective quasiparticle lifetimes are measured for aluminum³⁹ ($\approx 100 \mu\text{sec}$ at $\Delta/kT > 6$) tin⁴⁴ ($\approx 0.1 \mu\text{sec}$ at $\Delta/kT > 5$), and lead²⁶ ($\approx 10 \mu\text{sec}$ at $\Delta/kT > 5$). Even longer effective quasiparticle lifetimes are expected in BCS superconductors at lower operating temperatures ($\Delta/kT > 10$ or $T/T_C < 0.172$) and because of phonon trapping, discussed next.

The effective quasiparticle lifetime depends on several components: the intrinsic quasiparticle lifetime, τ_R ; the phonon escape lifetime into the substrate, τ_{ES} ; the anharmonic phonon

decay lifetime, τ_{AH} ; and the pair breaking lifetime, τ_B . The increase in the effective quasiparticle lifetime is evident from the solution to the Rothwarf-Taylor equations 12 and 13 where the combination of lifetimes τ_R , τ_B , τ_{ES} , and τ_{AH} results in an effective quasiparticle lifetime τ_{EFF} given by:

$$\frac{1}{\tau_{EFF}} = \frac{1}{\frac{\tau_R}{\tau_B} \tau_{ES}} + \frac{1}{\frac{\tau_R}{\tau_B} \tau_{AH}} \quad (16)$$

The effective quasiparticle lifetime is limited by the depletion rate of nonequilibrium pair breaking phonons through: (1) escape into the substrate with *effective* rate, $\tau_{EES} = (\tau_R/\tau_B) \tau_{ES}$ and (2) anharmonic phonon decay with *effective* rate, $\tau_{EAH} = (\tau_R/\tau_B) \tau_{AH}$ (provided $\tau_{AH} > \tau_B$). At lower temperatures and near thermal equilibrium, these effective rates are much slower since $(\tau_R/\tau_B) \gg 1$.

The effective anharmonic decay τ_{EAH} and effective phonon escape τ_{EES} lifetimes are greater than the corresponding intrinsic values for τ_{AH} and τ_{ES} .^{45,46,47} At low temperatures, τ_B is very small,³⁵ $\leq 10^{-10}$ sec, and τ_R is much longer, $\approx 10^{-5}$ sec, (or $\tau_R/\tau_B \geq 10^5$) leading to a condition wherein the nonequilibrium photodeposited energy resides most of the time in the form of excited quasiparticles. However, the photodeposited energy can be removed by: (1) anharmonic decay or (2) escape into the substrate when it exists in the form of nonequilibrium phonons and not excited quasiparticles. Since the photodeposited energy exists for the largest fraction of time, $\tau_R/(\tau_R + \tau_B)$, in the form of excited quasiparticles, there is proportionally very little time during which the nonequilibrium pair breaking phonons can escape into the substrate or undergo anharmonic decay. Therefore at low temperatures, the effective lifetimes $\tau_{EAH} \gg \tau_{AH}$ and $\tau_{EES} \gg \tau_{ES}$ become much larger, leading to corresponding increases in τ_{EFF} . With a longer τ_{EFF} , the QSKIP expected

performance is significantly improved which is evident from the Noise Equivalent Power (NEP) calculations in section 2.2.4. The noise current δI is calculated next.

2.2.3 NOISE LEVEL IN QSKIP

A superconductor operating in the current state, in principle, has two major noise sources: (1) fluctuations in the Cooper pair density and (2) fluxoid noise. The QSKIP is intended to operate at low temperatures and at $I_0 < 0.5 I_C$. Under these conditions, the operation of the QSKIP can be readily limited to the Meissner state (below H_{C1}) thereby minimizing the effects of fluxoid noise. Accordingly we calculate the noise in the QSKIP as primarily due to fluctuations in the Cooper pair density.

The QSKIP's noise current δI is calculated from the Root Mean Square fluctuations in the signal current I_s , specifically, $(\delta I)^2 = \langle I_s^2 \rangle - \langle I_s \rangle^2$ where the brackets $\langle \rangle$ represent the expected value. Expressions for the noise current δI are derived in terms of the statistical fluctuations in the density of Cooper pairs $\rho_{CP}(X)$ (or quasiparticle density N_Q) in branches 1 and 2 (see Fig. 2.1). The QSKIP noise current, δI , is expressed in terms of the quasiparticle density variances, σ_{Q1}^2 , and, σ_{Q2}^2 , in branches 1 and 2, respectively. The expression for the total noise current δI , is calculated as is the signal current I_s by using Eq. 14 and adding contributions from branches 1 and 2. Making use of Eq. 7 and 8, the equation for the QSKIP's root mean square noise current is:

$$\sqrt{\delta I^2} = \frac{I_0}{4\rho_{CP}(X)} \frac{\ell_1}{(\ell_1 + L_1)} \sqrt{\frac{\sigma_{Q1}^2 + \sigma_{Q2}^2}{V}} \quad (17)$$

In the thermal equilibrium branch 2, the quasiparticle density variance, σ_{Q2}^2 , is calculated from the quasiparticle statistics. At low temperature, the quasiparticle density is much less than the Cooper pair density ($\rho_{CP2} \gg N_Q$). We estimate the average quasiparticle density by $P_{EQ} \rho_{CP2} \approx N_Q^{EQ}$ where the probability P_{EQ} for breaking a Cooper pair is very small $P_{EQ} \ll 1$. Under these conditions, we can approximate the quasiparticle statistics⁴⁸ by a Poisson Probability Density Function (PDF). For a Poisson PDF, the variance σ_{Q2}^2 is equal to the mean quasiparticle density in branch 2, $\sigma_{Q2}^2 = (1/V) N_Q^{EQ}$ and the mean quasiparticle density is given by Equation 9.

In the photoilluminated branch 1, the quasiparticle density variance, σ_{Q1}^2 , is calculated by examining the quasiparticle statistics. The quasiparticle density in branch 1, N_Q , is expressed in terms of the thermal equilibrium quasiparticle density N_Q^{EQ} and the additional density of static nonequilibrium quasiparticles, ΔN_Q , generated by the absorption of N_Φ . This corresponds to a nonequilibrium state that is *different from thermal models where the increases in the quasiparticle population are due to heating of the superconductor*. Here, the quasiparticles' nonequilibrium state is maintained by an excess static nonequilibrium of pair breaking phonons. The total pair breaking phonon density is made up of contributions due to thermal equilibrium pair breaking phonons N_Ω^{EQ} , represented by Bose-Einstein statistics, and contributions due to photogenerated nonequilibrium pair breaking phonons. The photogenerated nonequilibrium phonons span a narrow energy range because photoexcited hot quasiparticles thermalize most efficiently by the emission of energetic phonons, to which they are most strongly coupled. These energetic phonons are primarily the pair breaking phonons that maintain the nonequilibrium quasiparticle population by virtue of the fact that they participate in the quasiparticle generation and recombination process, since they have a minimum energy of $\approx 2\Delta$. This nonequilibrium phonon representation is similar to (but not

the same as) the T^* approach used by Parker.⁴⁹ Parker represented the phonon densities in a superconductor under static thermal nonequilibrium as a sum of: (1) thermal equilibrium phonon density represented by a thermal equilibrium temperature T_0 and (2) an excited phonon density represented by a higher thermal equilibrium temperature $T^* > T_0$. Here, we are representing the static nonequilibrium phonon distribution (which span a narrow energy range with an energy greater than 2Δ) as a sum of two phonon densities: (1) the N_Ω^{EQ} thermal equilibrium pair breaking phonon density, and (2) a nonequilibrium phonon population $\Delta N_\Omega = N_\Omega - N_\Omega^{\text{EQ}}$ (see Eq. 12). This static nonequilibrium distribution of quasiparticles and pair breaking phonons cannot be described by two thermal equilibrium distributions at different temperatures, the T^* model.

For the selected QSKIP operating constraints, as in the case of the unilluminated branch 2, the nonequilibrium quasiparticle density is much smaller than the Cooper pair density ($\rho_{\text{CPI}} \gg N_Q$). Thus the average nonequilibrium quasiparticle density can be estimated as $N_Q^{\text{EQ}} + \Delta N_Q \approx P_{\text{NE}} N_{\text{CP}}$, where the probability for breaking a Cooper pair is very small, $P_{\text{NE}} \ll 1$. Under these conditions the nonequilibrium quasiparticle statistics can be estimated by a Poisson PDF and the variance σ_{Q1}^2 represented by the mean quasiparticle density in branch 1, $\sigma_{Q1}^2 = (1/V)[N_Q^{\text{EQ}} + \Delta N_Q]$ (see Eq. 13).

Using the explicit expression for the quasiparticle density variances, the expression for the QSKIP noise in Eq. 17 becomes:

$$\sqrt{\delta I^2} = \frac{I_0}{4\rho_{\text{CP}}(X)} \frac{\mathcal{L}_1}{(\mathcal{L}_1 + L_1)} \sqrt{\frac{2\eta(m_1 + m_2)\tau_{\text{EFF}} N_\phi + 2 N_Q^{\text{EQ}}}{V}} \quad (18)$$

The square root term includes thermal equilibrium contributions from both branches $2N_Q^{\text{EQ}}$ and contributions from the ΔN_Q additional quasiparticles photogenerated in the illuminated branch 1.

In Equation 18, we have represented the QSKIP's noise current in terms of the total quasiparticle variance $\sigma_{Q1}^2 + \sigma_{Q2}^2$ instead of the noise power spectral density $S(\omega)$. The total quasiparticle variance, by Parseval's theorem, is equal to the integral, over radial frequency ω , of the power spectral density $S(\omega)$, $\sigma_{Q1}^2 + \sigma_{Q2}^2 = \int S(\omega) d\omega$. The power spectral density $S(\omega)$ is obtained from the quasiparticles autocovariance.⁵⁰ The power spectral density for quasiparticles with Poisson statistics and with an effective lifetime τ_{EFF} is $S(\omega) = [\sigma_{Q1}^2 + \sigma_{Q2}^2] [4\sin^2(0.5\omega\tau_{\text{EFF}}) / (\omega^2\tau_{\text{EFF}})]$. The spectral width $2\pi/\tau_{\text{EFF}}$ of $S(\omega)$ reflects the fact that the quasiparticle autocovariance is correlated in time over the quasiparticle lifetime τ_{EFF} . The QSKIP noise δI can be reduced by band limiting the QSKIP operation below $\approx 2\pi/\tau_{\text{EFF}}$. However, representing the noise δI , in Equation 18, by the quasiparticle variance $\sigma_{Q1}^2 + \sigma_{Q2}^2$ yield a more conservative and upper limit estimate for the photodetector noise.

It should be noted that the quasiparticle variance computation, based on Poisson statistics, agrees with the results obtain for the variance of the electron plus hole populations in *intrinsic* semiconductors.^{51,52} In both cases we are dealing with excitation across an energy (or band) gap that leads to correlated distribution of quasiparticle or electron-hole pairs. In the case of a superconductor, for no branch imbalance, generation and recombination of quasiparticles produces fluctuations in the quasiparticles population modulo two. Similarly, in an *intrinsic* semiconductor generation and recombination of electron-hole pairs produces fluctuations in the number of holes plus electrons population always modulo two.

2.2.4 QSKIP PERFORMANCE CHARACTERISTICS

The QSKIP operates in the zero resistance current state and accordingly the responsivity (\mathfrak{R}_I) and NEP (calculated at the end of this section) are calculated in terms of current and not

voltage. The calculated responsivity is readily expressed in terms of the photoinduced magnetic flux Φ_B simply by multiplication of \mathfrak{R}_I by the QSKIP total magnetic inductance L_1+L_2 . The expressions for the current responsivity \mathfrak{R}_I is:

$$\mathcal{R}_I \left(\frac{\text{Amps}}{\text{Watt}} \right) = \frac{1}{h\nu} \frac{I_s}{VN_\phi^0} \quad (19)$$

The explicit expression for $\mathfrak{R}_I(\text{A/Watt})$ is obtained by substituting I_s (Eq. 14) into Eq. 19 and dividing by the incident photon power, $Vh\nu N_\phi^0$, to yield:

$$\mathcal{R}_I = \frac{1}{Vh\nu} \frac{I_0}{4\rho_{CP}(X)} \frac{\ell_i}{(\ell_i + L_1)} 2\eta(m_1 + m_2)\tau_{EFF} \quad (20)$$

The responsivity is directly proportional to the effective quasiparticle lifetime τ_{EFF} , as is expected for a photoconductive nonequilibrium quantum detector.⁵³ At low temperatures, the responsivity is greatly increased because the ratio $\tau_R/\tau_B \gg 1$ (see calculations by S. B. Kaplan³⁵ et. al) resulting in an effective quasiparticle lifetime significantly larger than the phonon trapping lifetime τ_{ES} (produced by acoustical mismatch at the film substrate interface) or the anharmonic phonon decay lifetime τ_{AH} . Thus, the maximum responsivity occurs at low temperatures.

BLIP is achieved when τ_{EFF} is sufficiently large so that the photon radiation shot noise is equal to the detector noise and the readout circuit noise. From Equation 18, it is evident that one requirement for BLIP is that $\eta(m_1+m_2)\tau_{EFF}N_\phi^0 > 2N_Q^{EQ}$. The NEP for a photodetector with readout circuits operating over a bandwidth ΔF is represented by:

$$\text{NEP}(\text{Watts} / \sqrt{\text{Hz}}) = \frac{\left[\frac{\delta I^2}{\Delta F} + \delta I_{\text{SQUID}}^2 \right]^{1/2}}{\mathfrak{R}_I} \quad (21)$$

Under BLIP conditions, the photon radiation shot noise is equal to, or greater than, the detector's internal noise, $\delta I \geq \Delta F^{1/2} \delta I_{\text{SQUID}}$. In section 2.2.3 it was shown that the detector noise is bounded by the quasiparticle variances σ_{Q1}^2 and σ_{Q2}^2 . Hence, for BLIP, the noise from the photogenerated quasiparticles is at least equal to the noise from thermal equilibrium quasiparticles leading to $\eta(m_1+m_2)\tau_{\text{EFF}}N_{\Phi}^0 \approx 2N_Q^{\text{EQ}}$ (see Eq. 18). The expression for the QSKIP's BLIP NEP, obtained with Eq. 20, is:

$$\text{NEP}_{\text{BLIP}} = h\nu \sqrt{\frac{VN_{\Phi}^0}{\Delta F \eta(m_1 + m_2)\tau_{\text{EFF}}}} \quad (22)$$

The QSKIP NEP varies with: VN_{Φ}^0 , the effective internal quantum efficiency $[\eta(m_1+m_2)]$, and the effective quasiparticle lifetime, τ_{EFF} . The VN_{Φ}^0 term corresponds to variance of the nonequilibrium quasiparticle population assuming Poisson statistics and $\eta(m_1+m_2)\tau_{\text{EFF}}N_{\Phi}^0 \approx 2N_Q^{\text{EQ}}$.

2.2.5 YBCO QSKIP RESPONSIVITY AND FREQUENCY BANDWIDTH

The responsivity is computed for a 100 μm square and 100nm thick YBCO QSKIP. In computing the responsivity, we choose operating conditions compatible with maximum responsivity and sensitivity. Specifically, for high responsivity (see Equation 20) the main conditions required are: (1) long effective quasiparticle lifetime τ_{EFF} , and (2) the smallest Cooper pair density $\rho_{\text{CP}}(X)$

compatible with a large τ_{EFF} . Presently for YBCO, there are no universally accepted theoretical or experimental values available for τ_{EFF} and we estimate this first followed by an estimate for $\rho_{\text{CP}}(X)$.

(1) Estimating τ_{EFF} in a YBCO QSKIP requires knowledge of $\tau_{\text{R}}/\tau_{\text{B}}$, τ_{ES} , τ_{AH} , and $2\Delta(0)$. The value of $2\Delta(0)$ is needed to determine the pair breaking phonon's frequency for estimating τ_{ES} , and τ_{AH} , since an estimate already exists for $\tau_{\text{R}}/\tau_{\text{B}} \approx 10^5$ (see section 2.2.2.3). From specific heat measurements³⁷ in YBCO, the measured pair binding energy $2\Delta(0)$ is about $32\text{meV} \approx 5k_{\text{B}}T_{\text{C}}$. This energy gap value is consistent with the Raman measurements which from line broadening identified the B_{1g} (out-of-phase oxygen plane vibration) at 340cm^{-1} as being particularly strongly coupled with the electrons,^{54,55} and this is inferred as being related to superconductivity. This strongly suggests that the pair breaking phonons are energetic B_{1g} optical phonon whose energies are approximately equal to the YBCO Debye energy⁵⁶ phonons, which corresponds to the value of the energy gap, $2\Delta(0) \approx 32\text{meV}$.

The estimate for the phonon escape lifetime τ_{ES} is based on several experimental results. Experimental measurements with acoustic phonons indicate a temperature independent 99% scattering probability at the YBCO/substrate boundary ($\tau_{\text{ES}} \approx 10^{-8}\text{sec}$ for 100nm YBCO film)⁵⁷. For pair breaking phonons there are no similar measurements, however, the YBCO phonon dispersion curves in the "c" direction⁵⁸ indicate that *there are no phonon propagating modes with sufficient energy to break Cooper pairs*. Thus from a c-axis oriented HTS film, pair breaking phonons will not be depleted by escaping into the substrate because of the relatively poor coupling between the supercurrent carrying CuO planes. Thus, we expect that the depletion of pair breaking phonons is primarily by anharmonic phonon decay, i.e. $\tau_{\text{AH}} \ll \tau_{\text{ES}}$.

Experimental values for τ_{AH} are not available for pair breaking phonons. The value of τ_{AH} is estimated from measurements on YBCO subjected to large deviations from thermal equilibrium, induced by energetic laser pulses³². At large deviations from thermal equilibrium, $\tau_R/\tau_B \approx 1$ and from measured effective³² τ_R we estimate $\tau_{AH} \approx 10-100$ psec. At low temperatures and near thermal equilibrium $\tau_R/\tau_B \geq 10^5$, leading to a minimum estimate for $\tau_{EFF} \approx 10 \mu\text{sec}$.

(2) The Cooper pair density for YBCO, $\rho_{CP}(X)$, is estimated from specific heat measurements that identify the contribution of the electronic component, γ_p . The density of states at the Fermi surface⁵⁹ $N(0) \approx 3\gamma_p/(\pi^2 k_B^2)$ is estimated from measured values⁶⁰ of γ_p [between 1.4-2.9 mJ/(g-atom-K²)] to be about $2.8-5.8 \times 10^{27}$ states/(eV-m³). Furthermore, the specific heat jump⁶⁰ at T_C [$\Delta C/\gamma_p T_C$] varies between 0.4-1.11 instead of the BCS value of 1.43. Loram et. al³⁷ measured γ_p at 10K vanishes, hence the reduced jump in the specific heat at T_C is not attributed to a multiphase YBCO sample, with normal regions, but is simply an indication of a smaller fraction (10%-30%) of k-space pairing than in a BCS superconductor. Accordingly, our estimate of $\rho_{CP}(X)$ is 10%-30% of $\Delta(0)N(0)/2 \approx 0.2-1.4 \times 10^{25}$ pairs/m³, or on average $\approx 8 \times 10^{24}$ pairs/m³.

Responsivity of the YBCO QSKIP is estimated with Equation 20 and under several operating conditions. By utilizing the diamagnetic effect and by using a special detector geometry, we can make the ratio $\ell_1/(\ell_1+L_1) \approx 1$. For 12 μm incident photons and $2\Delta(0) \approx 32 \mu\text{m}$, we estimate $\eta(m_1+m_2) \approx 1$, which corresponds to η less than 40% since each 12 μm (0.1 eV) photon breaks several pairs, or $(m_1+m_2) > 2$. The assumed detectors quantum efficiency of For a YBCO QSKIP with $I_0 \approx 0.07$ Amps, and $V \approx 5 \times 10^{-16}$ m³, the current responsivity becomes $\mathcal{R}_I \approx 5.5 \times 10^8 \tau_{EFF}$ Amps/Watt, and for $\tau_{EFF} \approx 10 \mu\text{sec}$ $\mathcal{R}_I \approx 5.5 \times 10^3$ Amps/Watt. This represents a very good responsivity

that is linearly proportional to the quasiparticle lifetime. The responsivity will increase or decrease directly with the effective quasiparticle lifetime, and is plotted in Fig-2.3.

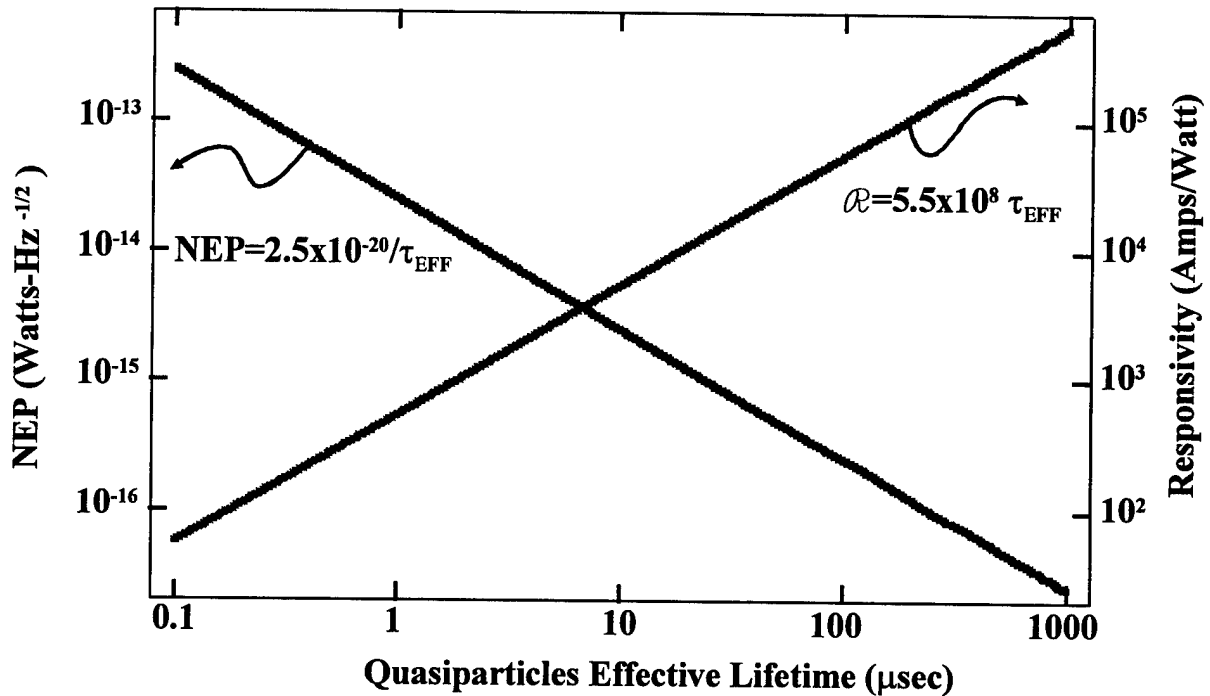


Figure 2.3. The QSKIP NEP and Responsivity are plotted as a function of effective quasiparticle lifetime at T=9K. A range for the effective quasiparticle lifetime is used to account for uncertainty in τ_B , τ_R , τ_{ES} and τ_{AH} .

The frequency bandwidth of the QSKIP is dependent on the effective quasiparticle lifetime and the detector's readout circuits. The maximum QSKIP frequency response, independent of the readout circuits, is estimated to be $1/\tau_{EFF}$ and for $\tau_{EFF} \approx 10 \mu\text{sec}$ the maximum QSKIP frequency response is $\approx 10^5 \text{Hz}$.

2.2.6 THE SENSITIVITY OF A YBCO QSKIP SENSOR

The sensitivity of any sensor includes, and is limited by, the noise from the detector and the detector's readout circuit. To achieve best sensitivity, smallest NEP, with a YBCO QSKIP requires:

(1) photon induced radiation shot noise to dominate over all other noise in the detector, and (2) a readout circuit with noise smaller than the detector's photon induced radiation shot noise $\delta I > \Delta F^{1/2} \delta I_{\text{SQUID}}$ (see Equation 21).

2.2.6.1 Noise in QSKIP

Noise in the YBCO QSKIP is minimized by reducing the thermal equilibrium quasiparticle density, and inhibiting the noise associated with fluxoid formation and transport. Noise from fluctuations in the quasiparticle population includes contributions (see Eq.18) from the thermal equilibrium quasiparticle density N_Q^{EQ} and the photon induced quasiparticle density $\eta(m_1+m_2)\tau_{\text{EFF}}N_\Phi^0$. By operating at sufficiently low temperatures, we can insure that within the detector the fluctuations in the quasiparticle density are dominated by photogenerated quasiparticles, i.e. $\eta(m_1+m_2)\tau_{\text{EFF}}N_\Phi^0 > 2N_Q^{\text{EQ}}$. Clearly, τ_{EFF} has a direct effect on the operating temperature at which noise from photogenerated quasiparticles dominates. The larger τ_{EFF} is the higher will be the detector temperature at which photon dominated noise performance is possible.

A second noise source in the QSKIP is associated with fluxoid trapping, generation and transport. This noise can be minimized by operating the photodetector at low current, $I_0 < 0.5I_C$, to insure operation in the Meissner state, or below H_{C1} . A reasonable value for the critical current density in YBCO at low temperatures is $\approx 2 \times 10^7 \text{ A/cm}^2$. For a 100nm thick YBCO film, 7 μm wide, $I_C \approx 0.14\text{A}$ and an operating current $I_0 \leq 0.07 \text{ Amp}$ is less than 50% of I_C . The self induced magnetic field produced by I_0 is less than 90 Gauss, which is below the value of H_{C1} in YBCO,^{61,62,63} thereby facilitating the maintenance of the QSKIP in the Meissner state, and severely inhibiting flux flow noise. Flux trapping and low frequency 1/f flux noise can be removed by

electronic means to create conditions wherein the dominant noise is from fluctuations in the photoinduced quasiparticle density (see Eq. 18).

2.2.6.2 Electronic removal of DC Offsets, SQUID Nonlinearities, and 1/f Noise.

The readout of the QSKIP is with a directly coupled SQUID readout circuit arranged in a feedback loop and operated like a DC magnetometer⁶⁴. Such a readout configuration, when combined with a “zero” photon reference source, lends itself to the removal of contribution from trapped flux, SQUID nonlinearities, and 1/f noise.

In operation, the photosignal is measured by first recording a “zero” calibration level and subtracting this level from the QSKIP’s output signal formed when the photodetector is exposed to a higher photon flux level. The “zero” calibration level is obtained by exposing the QSKIP to a very low photon flux level and recording the “zero” output signal with minimum noise⁶⁵. Any dc offsets or trapped flux in the SQUID or QSKIP are also included in the “zero” calibration level. Thus by subtracting the “zero” calibration level from each QSKIP signal in response to higher photon flux levels removes effects due to trapped flux and dc offsets

SQUID nonlinearities are removed by operating the QSKIP readout circuit as a DC magnetometer with a nulling feedback loop⁶⁶. The feedback loop will produce a null signal to maintain the readout SQUID at the same operating point. As the QSKIP output changes with different photon flux levels, the feedback circuit will maintain the SQUID at the same operating point, at an integer number of Φ_0 . Thus, the nonlinearities in the SQUID’s V - Φ characteristics will be removed.

Low frequency 1/f noise from the QSKIP and SQUID can be also removed by using the DC magnetometer with a feedback loop and the “zero” calibration level. The 1/f noise removal can be

mechanized provided the $1/f$ noise corner frequency in the SQUID and QSKIP are much smaller than the detector sampling frequency. SQUIDS may be obtained with a $1/f$ noise corner frequency between 0.1-1 Hz and this is much smaller than the detector's sampling frequency $\Delta F \geq 30\text{Hz}$. Thus, the $1/f$ noise contribution to the output signal will be correlated at a 30 Hz detector sampling rate. Recording and averaging the "zero" calibration level every several seconds provides a measure of the $1/f$ noise amplitude valid for about a second. Subtracting electronically the "zero" calibration level from the QSKIP output signal, in response to higher photon flux levels, will remove the $1/f$ noise component. In IR imaging systems, the "zero" calibration level corresponds to the "cold" reference source used to calibrate and remove DC offsets and $1/f$ noise contributions included in the detector's signal.

2.2.6.3 YBCO QSKIP Noise Equivalent Power

The ultimate performance of the QSKIP is limited by the readout circuit noise. The main contributor to the readout circuit noise is the SQUID. For BLIP sensitivity we require for the QSKIP noise to dominate over the readout circuit noise, i.e. $\delta I > \Delta F^{1/2} \delta I_{\text{SQUID}}$. Toward this end, we need: a SQUID with the lowest noise current, a QSKIP with the longest τ_{EFF} , and a sufficiently large photon density levels N_{Φ}^0 so that $\delta I > \Delta F^{1/2} \delta I_{\text{SQUID}}$ (see Equation 18). Since the QSKIP produces a photocurrent signal, the SQUID needed is one with a noise that has a very low spectral current power density.

SQUIDS with low noise current are facilitated by several operating conditions. For effective feedback operation, good modulation is required of the SQUID output voltage with bias current, and this is satisfied when $L_{\text{SQ}} I_{\text{SQ}} < \Phi_0$, where I_{SQ} and L_{SQ} are the SQUID critical current and loop inductance, respectively. Additionally, significant noise rounding in the SQUID I-V curves⁶⁷ is

prevented by selecting operating conditions which yield a $\gamma = hI_{SQ}/ek_B T > 100$. Selecting a SQUID with a small critical current $I_{SQ} \approx 10 \mu A$ allows a large SQUID inductance, $L_{SQ} \approx 200 pH$, and improves sensitivity by minimizing the SQUID's spectral noise current density. For $I_{SQ} \approx 10 \mu A$ and at $T = 9K$, $\gamma = hI_{SQ}/ek_B T \approx 300$ and this is consistent with operation that prevents significant noise rounding of the SQUID's I-V curves. In a low noise SQUID, the flux noise level^{68,69} is $\approx 10^{-6} \Phi_0 / Hz^{1/2} \approx 2 \times 10^{-21}$ Webers/ \sqrt{Hz} . With an inductance of $L_{SQ} \approx 200 pH$, the computed SQUID white noise current spectral density is $\delta I_{SQUID} \approx 10^{-11}$ Amps/ \sqrt{Hz} .

For a directly coupled SQUID readout circuit,¹⁸ and under BLIP performance we proceed to determine, in terms of N_Φ^0 and τ_{EFF} , the conditions required for $\delta I_{SQUID} \Delta F^{1/2} < \delta I$. We are assuming a serpentine QSKIP structure with $7 \mu m$ wide lines formed in a $0.1 \mu m$ thick YBCO film and within a $50 \times 100 \mu m$ area, with a value of $V \approx 5 \times 10^{-16} m^3$, which corresponds to a kinetic inductance of about $L_1 \approx 1.4 - 8 nH$. To satisfy the condition $\delta I_{SQUID} \Delta F^{1/2} < \delta I$, we need to select a sufficiently large N_Φ^0 (see Eq. 18) to satisfy the following expression:

$$\frac{I_0}{4\rho_{CP}(X)} \frac{L_1}{(L_1 + L_2)} \sqrt{\frac{2\eta(m_1 + m_2)\tau_{EFF} N_\Phi^0}{V}} > 10^{-11} \sqrt{\Delta F} \quad (23)$$

Evaluating Eq. 23 by substituting average values for: $L_1 \approx 4.7 nH$, $L_1/(L_1 + L_2) \approx 1$, $I_0 \approx 0.07$ Amps, $\rho_{CP}(X) \approx 0.8 \times 10^{25}$ pairs/ m^3 , $\eta(m_1 + m_2) \approx 1$, and a bandwidth ΔF of 30Hz, we obtain $\tau_{EFF} N_\Phi^0 > 1.5 \times 10^{17}$ photons/ m^3 . For a projected $\tau_{EFF} \approx 10 \mu sec$, we determine that $N_\Phi^0 > 1.5 \times 10^{22}$ photons/ m^3 -sec (corresponding to more than 1.5×10^{11} photons/sec- cm^2) is required for photon noise to dominate over the readout noise, i.e., $\delta I > \Delta F^{1/2} \delta I_{SQUID}$.

For BLIP performance, in addition to the requirement that $\delta I > \Delta F^{1/2} \delta I_{\text{SQUID}}$, N_{Φ}^0 needs to be sufficiently large so that the detector is dominated by the photoinduced quasiparticle noise, that is, $\eta(m_1+m_2)\tau_{\text{EFF}}N_{\Phi}^0 > 2N_Q^{\text{EQ}}$ (see Eq. 18). Below 9K, the value of N_Q^{EQ} is readily calculated with Eq. 9, where the product of all the pre-exponential factors is approximately equal to about 3.8×10^{25} quasiparticles/m³. Evaluating Eq. 9 at 9K, with $\Delta(0) \approx 16\text{meV}$, we obtain $N_Q^{\text{EQ}} \approx 1.6 \times 10^{16}$ quasiparticles/m³ and this leads to the requirement that $\tau_{\text{EFF}}N_{\Phi}^0 > 4 \times 10^{16}$ quasiparticles/m³ [assuming as before that $\eta(m_1+m_2) \approx 1$]. This is a less strict requirement than $\delta I > \Delta F^{1/2} \delta I_{\text{SQUID}}$ which requires that $\tau_{\text{EFF}}N_{\Phi}^0 > 1.5 \times 10^{17}$ photons/m³ (see previous paragraph).

For $\delta I > \Delta F^{1/2} \delta I_{\text{SQUID}}$, we calculate the NEP at BLIP. At 9K, for $\tau_{\text{EFF}} \approx 10\mu\text{sec}$, $N_{\Phi}^0 > 1.5 \times 10^{22}$ photons/m³-sec (corresponding to 1.5×10^{11} photons/sec-cm²). For 0.1eV photons, the equivalent NEP in a 30 Hz bandwidth is about 2.5×10^{-15} Watts/ $\sqrt{\text{Hz}}$. The photon flux level is selected to satisfy Eq. 23 and BLIP conditions. If the readout circuit is lower noise, a better NEP will be achieved. The QSKIP NEP limit due to noise from thermal equilibrium quasiparticles is 8×10^{-16} Watts/ $\sqrt{\text{Hz}}$ vs 2.5×10^{-15} Watts/ $\sqrt{\text{Hz}}$ for the readout circuit limited NEP. Better NEP should be achieved with larger values of τ_{EFF} [or $\Delta(T)$] or quieter readout circuits. A plot of the QSKIP NEP is given in Fig. 2.3 as a function of τ_{EFF} . The QSKIP performance is currently being experimentally investigated.

2.2.7 COMPETING LWIR SEMICONDUCTOR BASED QUANTUM DETECTORS

Development of competing semiconductor based quantum IR detectors has been under way for about 50 years.^{70,71,72} Included are Long Wave IR (LWIR) detectors with a spectral photoresponse (8-12 μm) that includes the black body radiation peak from room temperature (300K) objects, and Very Long Wave IR (VLWIR) detectors which are sensitive to colder objects ($\approx 150\text{K}$),

with black body radiation peaking in the 15-30 μ m spectral band. The main applications of the LWIR and VLWIR detectors are for the detection, or imaging, of black body radiation from men, man-made objects and very cold objects in space.

For LWIR applications intrinsic HgCdTe photoconductive⁷³ and photovoltaic⁷⁴ detectors have been used extensively. Photoconductive HgCdTe detectors have demonstrated very good performance⁷³ (NEP $\approx 10^{-14}$ Watts/Hz^{1/2} at 64K with a 12.5 μ m cut-off wavelength) but each detector needs a special preamplifier. For photoconductive arrays with many detectors, the power consumed by the readout amplifiers is significant, thereby limiting these detectors to scanning systems. The read out preamplifier power issue has motivated the development of photovoltaic HgCdTe detectors. Photovoltaic HgCdTe detectors⁷⁴ have been made with very good performance and at 77K have an NEP $\approx 10^{-14}$ Watts/Hz^{1/2} for a $\approx 10\mu$ m cut-off wavelength. The best photovoltaic detectors use p-on-n heterojunction diode structures. These photovoltaic HgCdTe arrays are compatible with low power readout electronics⁷⁵ but because of technological issues typically have shorter cut-off wavelength than photoconductive HgCdTe detectors (12.5 μ m vs $\approx 10\mu$ m). The shorter cut-off wavelength of photovoltaic HgCdTe detectors has opened the door for several competing extrinsic detector technologies which have longer cut-off wavelength and are compatible with low power focal plane readout circuits.

Typically, quantum VLWIR detectors are high resistance photoconductors whose photoresponse occurs by the photoionization of an impurity level^{76,77,78,79} in silicon or germanium. These extrinsic detectors^{80,81} include silicon doped with gallium (Si:Ga) or arsenic (Si:As), and these impurities provide VLWIR photoresponse with a 19 μ m cut-off wavelength (Si:Ga) and 25 μ m

cut-off wavelength (Si:As). The NEP performance⁸² of the Si:Ga and Si:As extrinsic photodetectors, below 20K, is about 5×10^{-13} Watts/Hz^{1/2}.

Another category of extrinsic detectors are Blocked Impurity Band⁸³ detectors (BIB) which also have a VLWIR response. These detectors have been formulated to circumvent the small optical absorption coefficient inherent in extrinsic high resistance photodetectors. Typically, the impurity's optical cross section is less than 10^{-15} cm² and there are about 10^{17} cm⁻³ impurities in the silicon, whose number is limited by the requirements of a long carrier lifetime and small leakage current. Intrinsic detectors have an optical absorption coefficient typically between 10-100 cm⁻¹ and for achieving good quantum efficiency it is not uncommon to find that extrinsic Si:As or Si:Ga detectors are 500µm thick. Use of thick detectors does achieve good quantum efficiency but at a cost of poorer spatial resolution. Typically a detector pixels size is less than 50µm square and since this is smaller than the detector thickness (optical absorption length) optical and electrical cross talk between detectors results. With the BIB detectors, within the solid solubility limit, the impurity concentration is increase and the leakage problem is handled by adding a blocking layer.^{84,85,86,87} With the increased impurity concentration the optical absorption increases and BIB detectors are typically ≤ 20 µm thin (vs 500 µm for extrinsic detectors). The BIB detectors offer very good spatial resolution and improved quantum efficiency. Operating at about 10K, a Si:Ga BIB detector, with a 25µm cut-off wavelength, is *projected*⁸⁴ to have an NEP of 10^{-17} Watts/Hz^{1/2}.

By comparison, the QSKIP is an intrinsic detector and thus we expect a higher absorption quantum efficiency. With higher optical absorption the QSKIP can be made smaller (better spatial resolution) than the BIB detector. Also, the anticipated cut-off wavelength for the QSKIP is about

32 μ m vs 25 μ m for the Si:As BIB detector. The QSKIP projected NEP is yet to experimentally verified, but it is projected to be better than that intrinsic HgCdTe detectors.

2.2.8 CONCLUSIONS ON OPERATION OF QSKIP

We have described a Quantum Superconducting Kinetic Inductance Photodetector suitable for operation in a low background environment and compatible with LTS and HTS material technologies. The QSKIP responsivity and NEP are analyzed using the Hamiltonian energy functional and *linearized* Rothwarf-Taylor equations. The QSKIP is intended to operate at low temperatures, in the current state, and below H_{C1} to maximize photoresponsivity and to suppress flux flow and Johnson noise, present in resistive current operation. The noise remaining is due to phonon induced fluctuations in the Cooper pair population, and this noise is significantly reduced because at $T \ll T_C$ the population of pair breaking phonons ($\hbar\Omega > 2\Delta(T)$) is very small. As in semiconductor based photoconductive quantum detectors, the QSKIP responsivity increases with the effective quasiparticle photoexcitation lifetime. Because the energy gap in superconductors (unlike the bandgap in conventional semiconductor detectors) is comparable to the energy of pair breaking phonons, trapping of these phonons increases the effective quasiparticle lifetime and thereby maximizes the QSKIP photoresponsivity. The trapping of pair breaking phonons in YBCO is very effective because, according to experiment, the pair breaking phonons cannot travel in the "c" direction (toward the substrate) since such large energy phonon modes do not exist for the "c" direction. Thus, the pair breaking phonons will be effectively prevented from escaping into the substrate and can only escape by lateral motion or anharmonic decay. The QSKIP is projected to have a spectral photoresponse up to $2\Delta(T)$, the superconductor's energy gap, $\approx 32\mu$ m for YBCO at $T \ll T_C$. Such a wide spectral response is currently achieved only with thermal detectors. Operating

the QSKIP at about 9K should provide very good performance to about $32\mu\text{m}$ with a calculated NEP of about 2.5×10^{-15} Watts/ $\sqrt{\text{Hz}}$.

2.3 DETECTOR FABRICATION

The original design for the kinetic inductance detector involved magnetic coupling between the detector and the readout SQUID. The multilayer HTS fabrication process required to produce such a device was not however available at the time. Thus the concept of the direct-coupled detector was invented to allow the use of a single YBCO layer to fabricate both detector and readout SQUID.

2.3.1 Step-edge Junction Version

The initial approach to the all-HTS direct-coupled detector is shown in Figure 2.4. The design uses step-edge grain boundary (SEGB) junctions which are formed where a YBCO film crosses a sufficiently sharp step in either the substrate or a deposited insulator. A second version, shown in Figure 2.5 and 2.6, incorporates a meander pattern in the YBCO, in order to increase kinetic inductance and to minimize quasiparticle diffusion between the two branches of the loop.

The fabrication steps for such devices are as follows:

1. Deposit ≈ 400 nm thick Nb milling mask on NdGaO_3 substrate
2. Pattern Nb milling mask by Reactive Ion Etching (RIE)
3. Ion mill ≈ 200 nm step into NdGaO_3 substrate
4. Remove remaining Nb by RIE
5. Deposit ≈ 150 nm YBCO and ≈ 50 nm in-situ Au
6. Ion mill YBCO and in-situ Au
7. Ion mill in-situ Au to open areas for light to impinge
8. Deposit SiO_2
9. RIE SiO_2
10. Deposit and lift off Au/Ti contacts and light shield

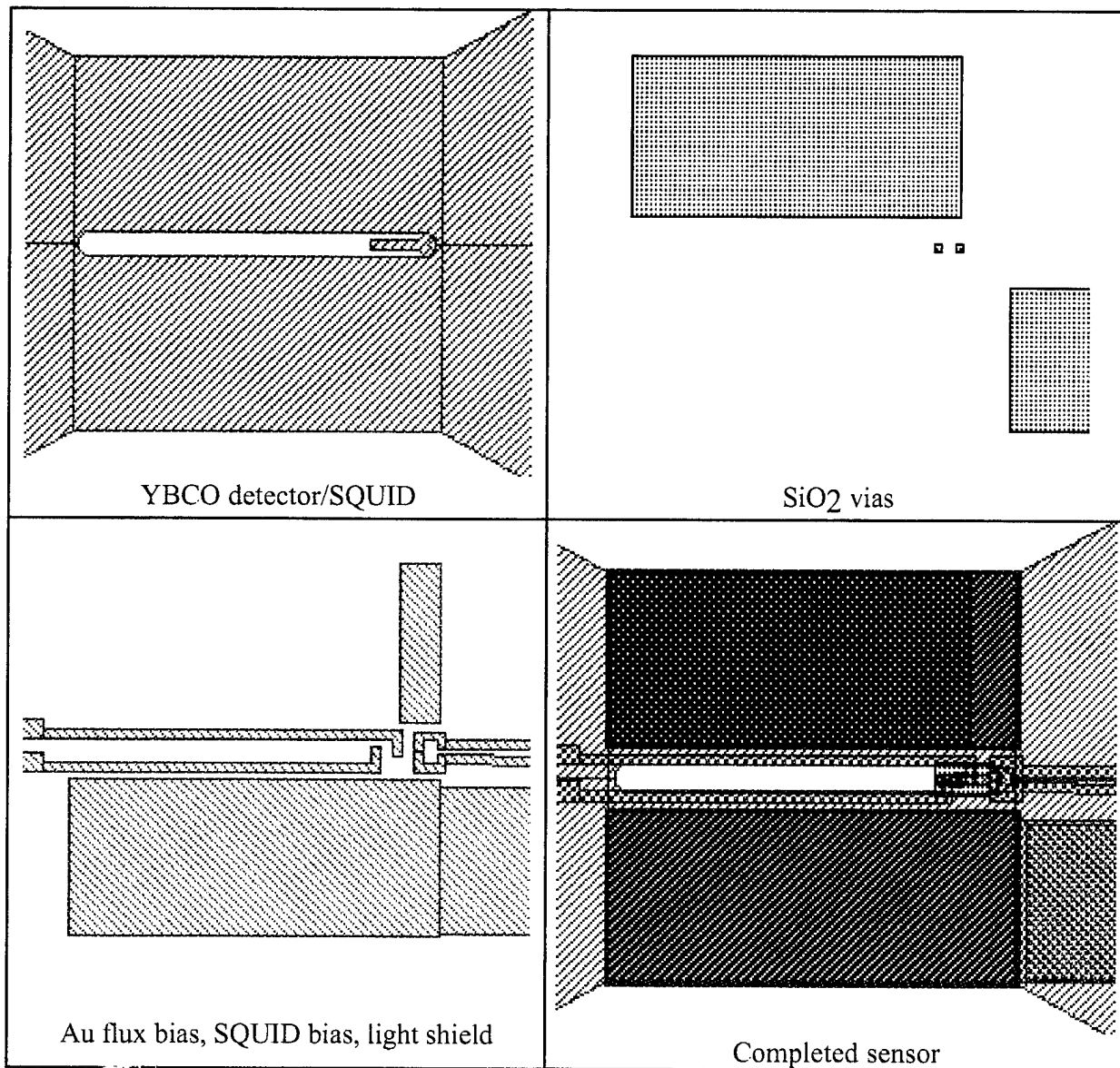


Figure 2.4 Direct-coupled HTS kinetic inductance detector with single slit. The SEGB SQUID is located at the right end of the slit.

The use of a metal milling mask, rather than photoresist, allows for definition of sharper steps in the NdGaO_3 , (see Figure 2.7) which leads to improved junction properties. The use of in-situ Au over the YBCO serves as passivation on the grain boundary, which we have found essential for good junction properties. The use of an insulating passivation layer would be preferable, since

the Au reduces the junction resistances, but the use of SrTiO_3 passivation has so far been found to severely decrease the critical current of the junctions.

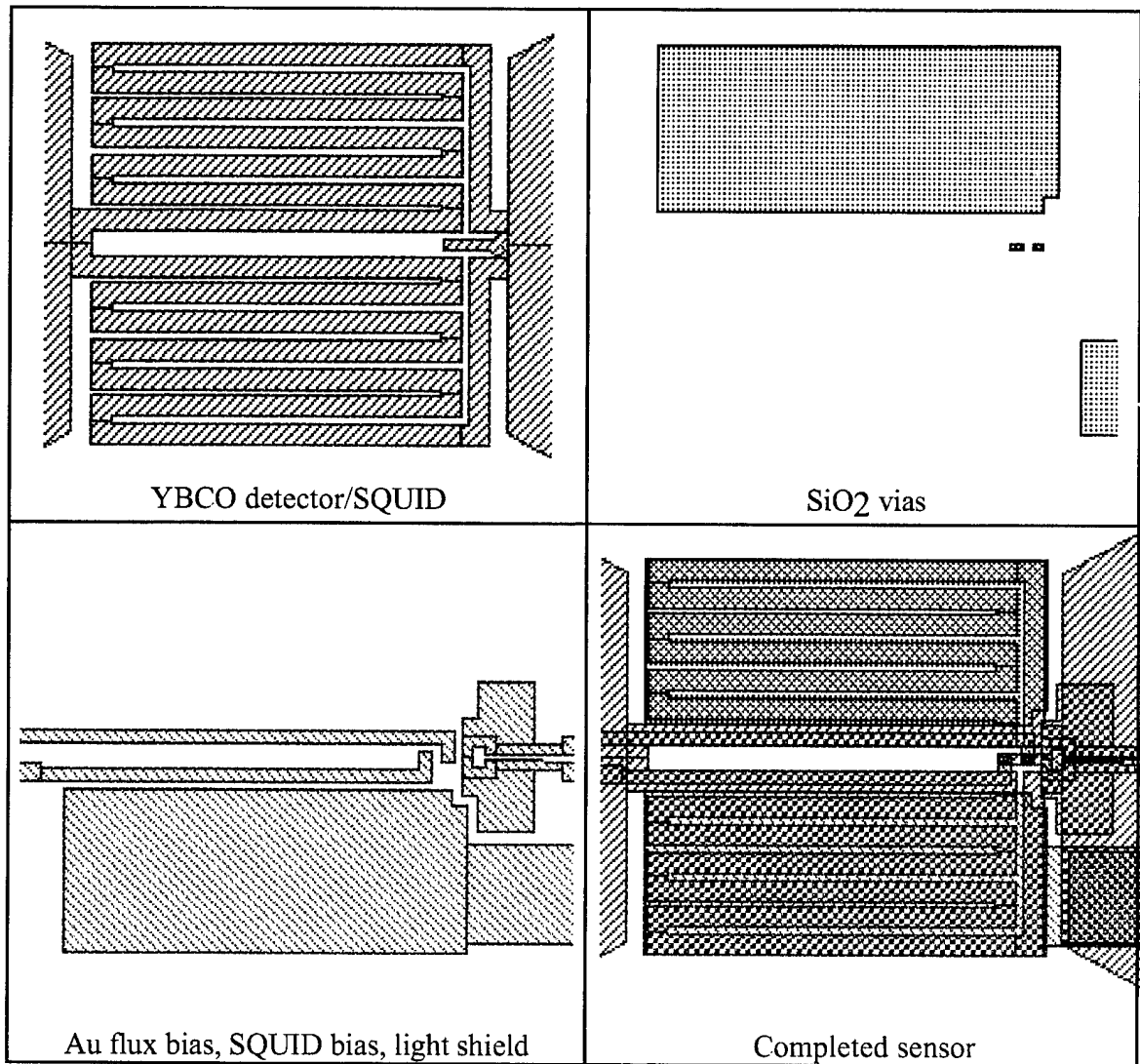


Figure 2.5. Direct-coupled HTS kinetic inductance detector with meander pattern. The meander increases the total kinetic inductance, reduces quasiparticle diffusion between the two branches, and fills area efficiently.

Initially most of the area of the in-situ Au on the YBCO was preserved, even away from the junctions, to protect the YBCO during processing. However it was found that this caused problems

for the adhesion of the SiO_2 so the process was changed to remove most of the in-situ Au from the YBCO.

In practice the most significant problem was deterioration of the YBCO T_c due to overlayers of SiO_x , which robbed oxygen from the YBCO. Removal of the SiO_x from the YBCO followed by an anneal resulted in recovery of the T_c to within a couple of degrees of the original value. This residual depression of T_c was presumably due to some diffusion of Si into the YBCO. This proved to be a severe problem and may have resulted in significant depression of the quasiparticle lifetime in the YBCO.

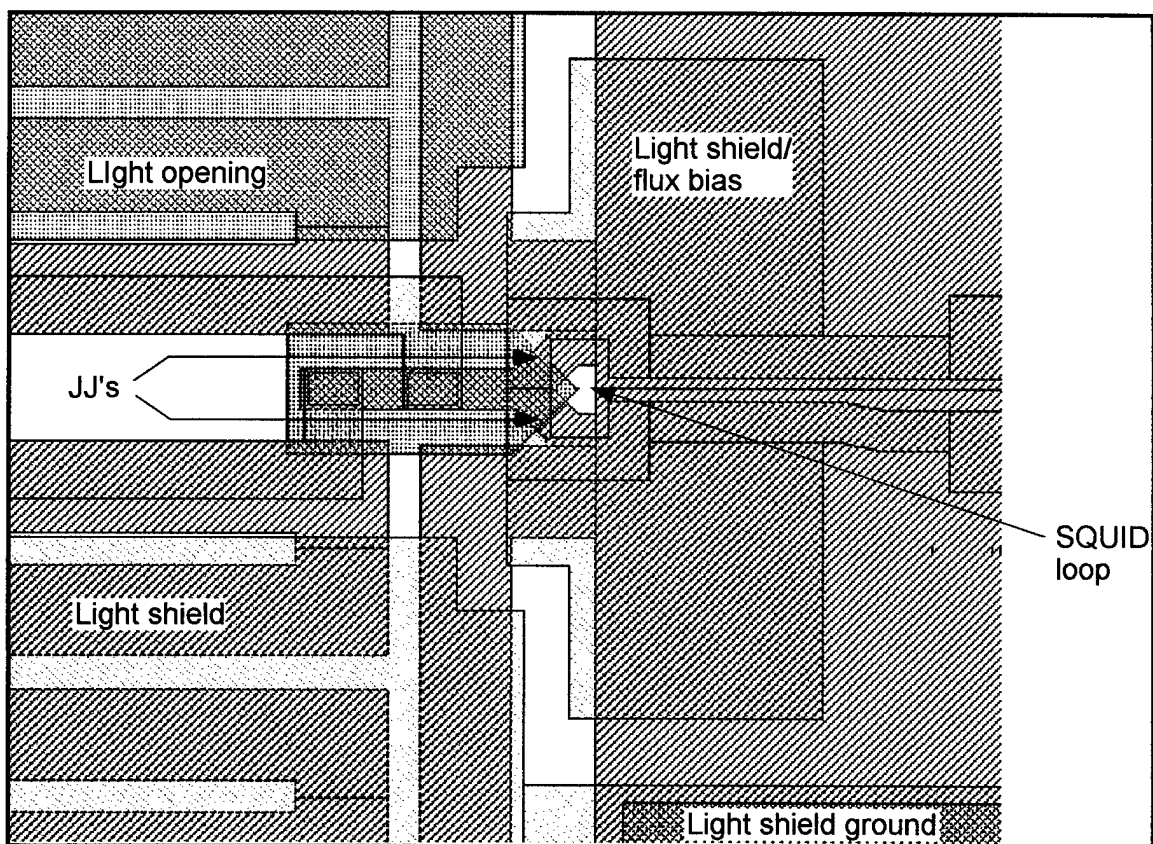


Figure 2.6. Detail of the readout SQUID for the detector of Figure 2.5. The gold layer coming from the right serves as both a light shield and a flux control line to set the operating point of the SQUID.

2.3.2 Bicrystal Junction Version

Since the detector is required to operate down to low temperatures (~ 10 K) the relatively high critical current density of SEGB junctions is a potential problem in that it is difficult to fabricate an optimized SQUID to operate at such low temperatures. We therefore fabricated a second detector version using bicrystal junctions, which have lower J_c values, making fabrication of an optimized SQUID easier.

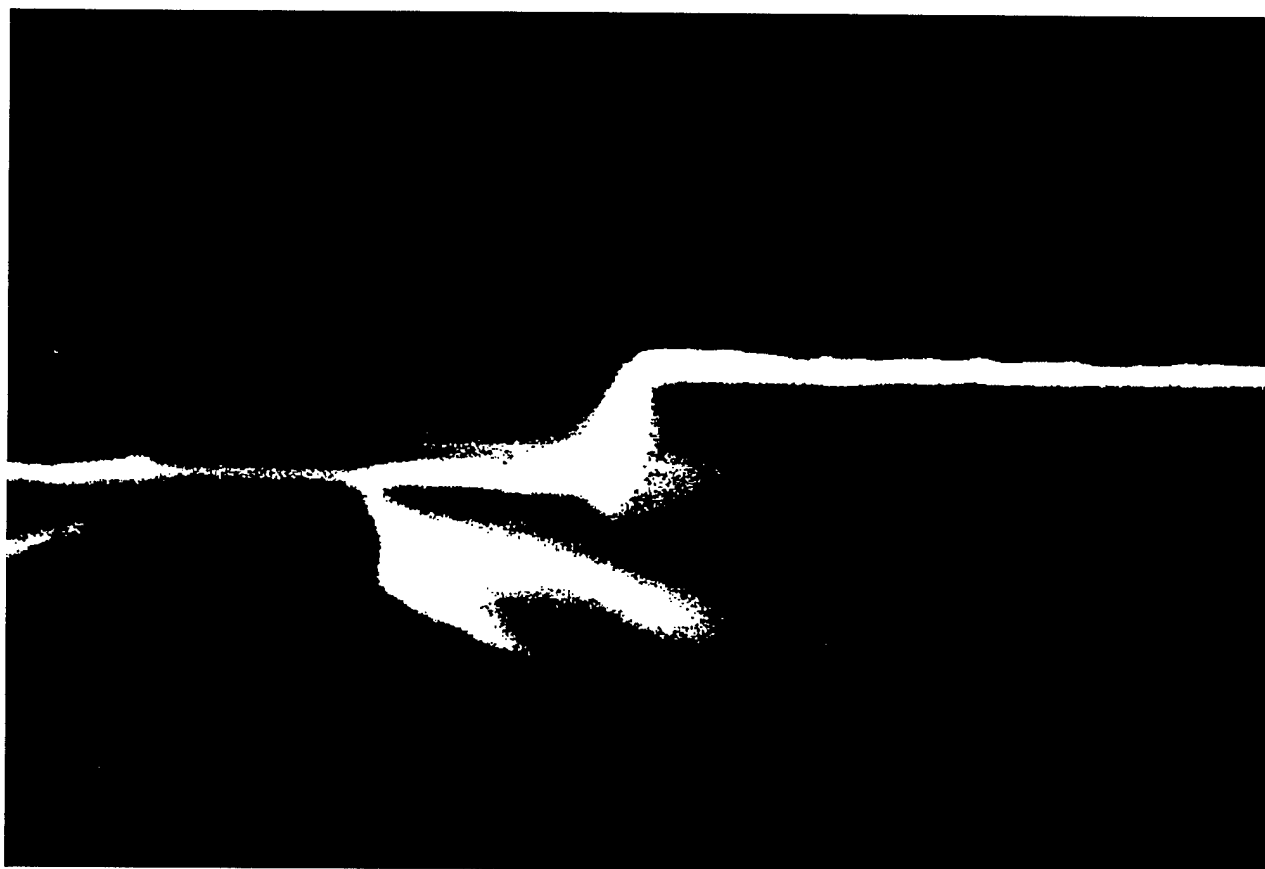


Figure 2.7 Cross-sectional SEM micrograph of a step in a NdGaO_3 substrate, fabricated using a Nb ion milling mask. The sharpness of the step and the minimal rounding of the top of the step are required to produce good step-edge grain boundary junctions.

The mask layout for this version of the detector is shown in Figure 2. The fabrication steps for such a device is as follows:

1. Deposit ≈ 150 nm YBCO and ≈ 50 nm in-situ Au on a SrTiO_3 bicrystal substrate

2. Define a ruler pattern at each end of the substrate grain boundary, ion milling through the YBCO/Au bilayer.
3. Note the position of the grain boundary on each ruler.
4. Define the YBCO pattern lithographically, using the known position of the grain boundary on the ruler to align.
5. Ion mill YBCO and in-situ Au
6. Ion mill in-situ Au to open areas for light to impinge
7. Deposit SiO_2
8. RIE SiO_2
9. Deposit and lift off Au/Ti contacts and light shield

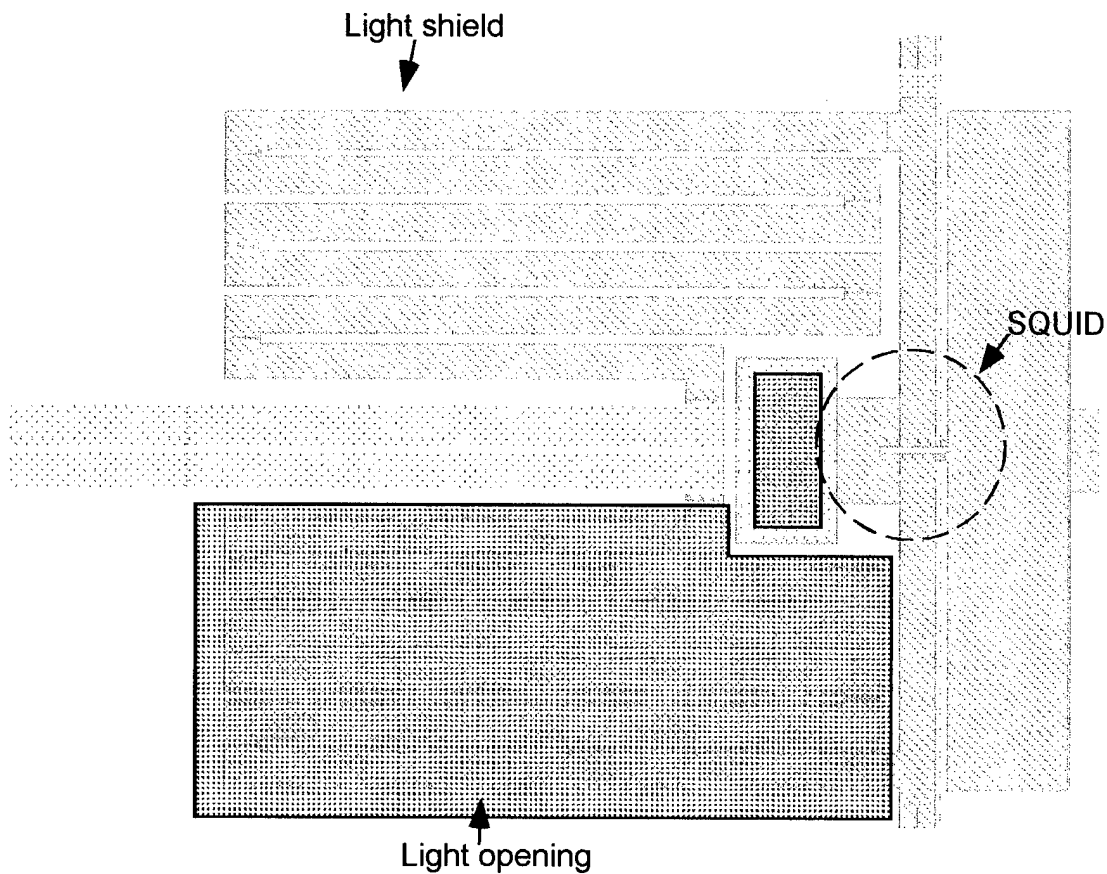


Figure 2.8. Mask layout for the bicrystal direct-coupled detector.

2.4 REFERENCES

- ¹ R.A. Smith, F.E. Jones and R.P. Chasmar, **THE DETECTION AND MEASUREMENTS OF INFRA-RED RADIATION** (Oxford at Clarendon Press, NY, 1958), p 206.
- ² P.W. Kruse, L.D. McGlauchlin and R.B. McQuistan, **ELEMENTS OF INFRARED TECHNOLOGY: GENERATION, TRANSMISSION, AND DETECTION** (John Wiley and Sons, NY, 1962), p 354.
- ³ Y. Enomoto and T. Murakami, J. Appl. Phys., **59**(11), 3807 (1986).

-
- ⁴ J.G. Bednorz and K.A. Muller, Z. Phys. B **64**, 189 (1986); Rev. Mod. Phys., **60**, 585 (1988).
- ⁵ H. S. Kwok, J.P. Zheng, and Q.Y. Ying, Appl. Phys. Lett., **54**, 2473 (1989).
- ⁶ M. Leung, P.R. Broussard, J.H. Claassen, M. Osofsky, S.A. Wolf and U. Strom, J. Appl. Phys. Lett., **51**, 2046, (1987).
- ⁷ W.S. Brookesby, D. Monroe, A.F.J. Levi, M. Hong, S.H. Liou, J. Kwo, C.E. Rice, P.M. Mankiewich and R.E. Howard, Appl. Phys. Lett., **54**, 1175 (1989).
- ⁸ E. M. Gershenzon, G. N. Gol'tsman, A. N. Semenov, A. V. Sergeev, IEEE trans. on Magn. **27**, 1321 (1991).
- ⁹ G. N. Gol'tsman, P. Kouminov, I. Goghidze, and E. M. Gershenzon, Physica C **235**, 1979 (1994).
- ¹⁰ M. A. Heusinger, A. D. Semenov, R. S. Nebosis, Y. P. Gusev, and K. F. Renk, IEEE trans. on Appl. Supercond. **5**, 2595 (1995).
- ¹¹ F. A. Hegman, R. A. Hughes, and J. S. Preston, Appl. Phys. Lett. **64**, 3174 (1994).
- ¹² M.G. Forrester, M. Gottlieb, J.R. Gavaler, and A.I. Braginski, IEEE Trans. on Magn., **MAG-25**, 1327, (1989).
- ¹³ A.M. Kadin, M. Leung, A.D. Smith, and J.M. Murduck, IEEE Trans. on Magn., **MAG-27**, 1540 (1991).
- ¹⁴ R. Kaplan, W.E. Carlos and E.J. Cukaukas, J. Appl. Phys., **67**, 4212 (1990).
- ¹⁵ E.K. Track, M. Radpavar, S.M. Faris, IEEE Trans. Magn. **MAG-25**, 1096 (1988).
- ¹⁶ In addition to the quasiparticle lifetime, the generation of the photosignal advocated in reference 13 depends on several complicated processes. First, each absorbed photon needs to locally suppress superconductivity by creating a vortex pair, however, the threshold, efficiency and conditions necessary for this creation process are difficult to model. Second, once the vortex pair is photogenerated, the photosignal level and noise depend on the vortex transport mechanism (e.g., flux creep or flow). In contrast, the QSKIP's signal only depends on the quasiparticle lifetime through the kinetic inductance of the condensate.
- ¹⁷ N. Bluzer, United States Patents 5,179,072 and 5,185,527.
- ¹⁸ N. Bluzer and M.G. Forrester, presented at the 1994 Applied Superconductivity Conference, October 16-21, 1994, Boston, Mass., and published in the IEEE Trans. on Applied Superconductivity, **5**(2), 2583(1995).
- ¹⁹ N. Bluzer and M.G. Forrester, Optical Engineering, **33** No. 3, 697 (1994); N. Bluzer and M.G. Forrester, Journal of Superconductivity, **7**, No. 2, 395 (1994).
- ²⁰ William L. Wolfe and George J. Zissis, Editors, **THE INFRARED HANDBOOK** (The Infrared Information and Analysis Center, Environmental Research Institute of Michigan, Revised Edition 1985) p19-45.

²¹ H. Goldstein, **CLASSICAL MECHANICS** (Addison-Wesley Publishing Co., Inc., Reading, Massachusetts 1950) Chapter 2

²² J.D. Jackson, **CLASSICAL ELECTRODYNAMICS** (John Wiley and Sons, Inc., New York, 1962) Chapter 6, p 181.

²³ With the so called London gauge we set $A_{\perp}(X) = -\Lambda J_{\perp}(X)$, where \perp denotes the normal component of the vector potential $A(X)$ and the current density $J(X)$ at all boundaries. Thus the canonical momentum $p = q_{CP}[\Lambda J_s(X) + A(X)]$ is equal to zero over the entire boundary and is given in terms of the condensate's phase angle θ as $p = i\hbar \nabla \theta = 0$. Hence θ is equal to a constant over the entire superconductor. Under these conditions $\Lambda J_s(X) = -A(X)$, where $\Lambda = m_{CP}/[\rho_{CP}(X)q_{CP}^2]$.

²⁴ J. Bardeen, L. N. Cooper, and J. R. Schrieffer, Phys. Rev. **108**, 1175 (1957); M. Tinkham, **INTRODUCTION TO SUPERCONDUCTIVITY** (Robert E. Krieger Publishing Co., Malabar, FL 1985), Chapter 2.

²⁵ Dale Corson and Paul Lorrain, **INTRODUCTION TO ELECTROMAGNETIC FIELDS AND WAVES** (W.H. Freeman and Co. San Francisco, 1962) Chapter 6, p254.

²⁶ W.H. Parker and W.D. Williams, Phys Rev. Lett. **29**, 924(1972).

²⁷ A. Rothwarf and B.N. Taylor, Phys. Rev. Lett. **19**, 27 (1967).

²⁸ Since all the terms in the Rathwarf-Taylor equations use volume density, we choose to use volume density instead of area density for the photon flux. The photon volume flux density is obtained by dividing the photoabsorbed fraction of the incident photon flux by the QSKIP's thickness $d \approx 100\text{nm}$.

²⁹ A. A. Abrikosov, L.P. Gorkov, and I.E. Dzyaloshinski, **METHODS OF QUANTUM FIELD THEORY IN STATISTICAL PHYSICS**, (Prentice-Hall, Engelwood Cliffs, NJ, 1993).

³⁰ M.Yu. Reizer, Phys. Rev. B **39**, 1602 (1989).

³¹ M.Yu. Reizer, Phys. Rev. B **40**, 5411 (1989).

³² N. Bluzer, Phys. Rev. B **46**, 1033 (1992); Phys. Rev. B **44**, 10222 (1991).

³³ N. Bluzer, IEEE Trans. Appl. Supercond. **3**, 2869 (1993).

³⁴ U. Fano, Phys. Rev. **70**, 44(1946)

³⁵ S.B. Kaplan, C.C. Chi, D.N. Langenberg, J.J. Chang, S. Jafarey, and D.J. Scalapino, Phys. Rev. B **14**, 4854 (1976).

³⁶ A.V. Sergeev and M.Yu.Reizer, "Nonequilibrium Superconducting Detectors of Electromagnetic Radiation," submitted to Phys. Rev. B.

-
- ³⁷ J.W. Loram, K.A. Mirza, J.R. Cooper and W.Y. Liang, MOS Satellite Conference to LT-20 July 27-31, 1993. Journal of Superconductivity, Plenum NY.
- ³⁸ J. A. Levine and S. Y. Hsieh, Phys. Rev. Lett. **20**, 994 (1968).
- ³⁹ K. E. Gray, A. R. Long and C. J. Adkins, Philos. Mag. **20**, 273 (1969).
- ⁴⁰ Michael Nahum, from Harvard, recently inferred the quasiparticle lifetime in aluminum from diffusion lengths measurements made in aluminum NIS tunnel junctions. At temperatures much less than 1K, the measured quasiparticle diffusion lengths are much larger than 300 μm . These very long quasiparticle diffusion length are consistent with quasiparticle lifetimes at least 1 μsec long and more likely several orders of magnitude larger (private communications).
- ⁴¹ I. Schuller and K. E. Gray, Phys. Rev. B **14**, 4213 (1976).
- ⁴² F. Jaworski, W. H. Parker and S. B. Kaplan, Phys. Rev. B **14**, 4209 (1976).
- ⁴³ P. Hu, R. C. Dynes and V. Narayanamurti, Phys. Rev. B **10**, 2786 (1974).
- ⁴⁴ A. Sai-Halasz, C. C. Chi, A. Denenstein, and D. N. Langenberger, Phys. Rev. Lett. **33**, 215 (1976).
- ⁴⁵ W.A. Little, Can. J. Phys. **37**,334(1959).
- ⁴⁶ A. C. Anderson, in **NON-EQUILIBRIUM SUPERCONDUCTIVITY, PHONONS, AND KAPITZA BOUNDARIES**, edited by Kenneth E. Gray (Plenum, New York, 1980)p. 263.
- ⁴⁷ S. B. Kaplan, J. low Temp. Phys. **37**, 343(1979).
- ⁴⁸ A. Papoulis, **PROBABILITY, RANDOM VARIABLES, AND STOCHASTIC PROCESSES** (McGraw Hill Systems in Science Series, NY 1965), chapter 16.
- ⁴⁹ W.H. Parker, Phys. Rev. B, **12**, 3667 (1975).
- ⁵⁰ The power spectral density of the quasiparticles noise is derived from the Poisson process examples given in Ref. 48 on pages 284-287.
- ⁵¹ R. E. Burgess, Phys. Soc. London, **B68**, 661 (1955).
- ⁵² R. E. Burgess, Phys. Soc. London, **B69**, 1020 (1956).
- ⁵³ R.K. Willardson and A.C. Beer, Editors, **SEMICONDUCTORS AND SEMIMETALS**, Infrared Detectors Vol. 5 (Academic Press, New York 1970). p219

-
- ⁵⁴ B. Friedl, C. Thomsen, and M. Cardona, Phys. Rev. Lett. **65**, 915(1990).
- ⁵⁵ R.E. Cohen, W.E. Pickett, and H. Krakauer, Phys. Rev. Lett. **64**, 2575(1990); R.E. Cohen, W.E. Pickett, and H. Krakauer, Phys. Rev. Lett. **62**, 831(1989).
- ⁵⁶ H.E. Fisher, S.K. Watson, and D.G. Cahill, Comments Mod. Phys. B **14**(2), 65(1988).
- ⁵⁷ G. L. Carr, M. Quijada, P. B. Tanner, et al., Appl. Phys. Lett., **57**, 2725 (1993); Nahum, S. Verghese, P.L. Richards, and K. Char, J. Appl. Phys. Lett. **59**, 2034(1991).
- ⁵⁸ See in particular Figure 5 in: W. Reichard, D. Ewert, E. Gering, F. Gompf, L. Pintschovius, B. Reneker, G. Collin, A.J. Dianoux, and H. Mutka, Physica B **156&157**, 897 (1989).
- ⁵⁹ Charles Kittel, **INTRODUCTION TO SOLID STATE PHYSICS**, (John Wiley, New York, 1971), p. 255.
- ⁶⁰ Y. Iye, T. Tamegai, H. Takeya and H. Takei, Physica **148 B**, 224(1987).
- ⁶⁰ A compilation of values for γ_p and $\Delta C/\gamma_p T_C$ obtained at different laboratories is given in table 1.6 of reference 56.
- ⁶¹ Y. Iye, T. Tamegai, H. Takeya and H. Takei, Physica **148 B**, 224(1987).
- ⁶² W. J. Gallagher, T. K. Worthington, T. R. Dinger, F. Holtzberg, D. L. Kaiser and R. L. Sandstorm, Physica **148 B**, 228, (1987).
- ⁶³ Y. Hidaka, M. Oda, M. Suzuki, A. Katsui, T. Murakami, N. Kobayashi, and Y. Muto, Physica **148 B**, 329 (1987).
- ⁶⁴ J. M. Clarke, W. M. Goubau, and M. B. Ketchen, Appl. Phys. Lett. **27**, 155 (1975); J. Low Temp. Phys. **25**, 99 (1976).
- ⁶⁵ N. Bluzer, SPIE Proceedings on Infrared Detectors and Arrays, Orlando Fl. 6-7 April 1988, Vol. 930, p. 64
- ⁶⁶ M. Huck, C. Heiden, and J. Clarke, Journal of Appl. Phys. **75**(9),4588 (1994).
- ⁶⁷ C.M. Falco, W.H. Parker, S.E. Trullinger, and P.L. Hansma, Phys. Rev., **B10**, 1865 (1974).
- ⁶⁸ H. Seppa, M. Kiviranta, A. Satrapinski, L. Gronberg, J. Salami, and I. Suni, IEEE Trans. on Appl. Superconductivity **3**(1), 1816 (1992).
- ⁶⁹ C.D. Tesche and J. Clarke, Journal of Low Temp. Phys. **29**, Nos.3/4, 301 (1977).
- ⁷⁰ E. Burstein, J. W. Davisson, E. E. Bell, W. J. Turner and H. G. Lipson, Phys. Rev. **93**, 65 (1954).
- ⁷¹ H. H. Woodbury and W. W. Tyler, Phys. Rev. **105**, 84 (1957).
- ⁷² H. Levinstein, Proc. Inst. Radio Engrs. **47**, 1478 (1959).

-
- ⁷³ M. A. Kinch, S. R. Borrello and A. Simmons, *Infrared Physics* **17**, 127 (1977).
- ⁷⁴ D. J. Gulbransen, J. K. Kojiro, C. G. Whitney, R. O. Mascitelli, T. L. Koch, M. S. Langell, A. J. Justice and D. F. Murphy, *Proc. of the IRIS specialty group on passive sensors*, Vol. 1, p13, 1991.
- ⁷⁵ N. Bluzer and A. S. Jensen, *Optical Engineering* **26**(3), 241 (1987), N. Bluzer and R. Stehlik, *IEEE trans. on Electr, Devices* **ED-25**(2), 213 (1978).
- ⁷⁶ E. Burstein, G. Pincus and N. Sclar, **PHOTOCONDUCTIVITY CONFERENCE** (John Wiley and Sons, New York ,1956)p 353.
- ⁷⁷ M. L. Schultz and G. A. Morton, *Proc. IRE* **43**, 1891 (1955).
- ⁷⁸ J. A. Burton, *Physica* **20**, 845 (1954).
- ⁷⁹ H. H. Woodbury, *Phys. Rev.* **105**, 613 (1957).
- ⁸⁰ N. Sclar, *Infrared Physics* **16**, 435 (1976).
- ⁸¹ D. K. Schroder in **TOPICS IN APPLIED PHYSICS Vol. 38, CHARGE COUPLE DEVICES**, edited by D. F. Barbe (Springer-Verlag, New York)p. 57.
- ⁸² W. L. Wolfe and G. J. Zissis, editors, **THE INFRARED HANDBOOK** , revised edition (Environmental Research Institute of Michigan, Ann Arbor, Michigan 1985)chapter 11.
- ⁸³ M. D. Petroff and M. G. Stapelbrock, United States Patent NO. 4 568 960, granted Feb. 4, 1986.
- ⁸⁴ F. Szmulowicz and F. L. Madarsz, *J. Appl. Phys.* **62**(6), 2533 (1987).
- ⁸⁵ F. Szmulowicz, F. L. Madarsz and J. Diller, *J. Appl. Phys.* **63**(11), 5583 (1988).
- ⁸⁶ B. G. Martin, *Solid-State Electronics* **33**(4), 427 (1990).
- ⁸⁷ D. M. Watson and J. E. Huffman, *Appl. Phys. Lett.* **52**(19), 1602 (1988).

3.0 EXPERIMENTAL APPROACH AND MEASUREMENTS

In this section, we describe the experimental approach used and the measurements made. All the equipment and engineering effort used to design the experimental test station were done on Westinghouse funds. The experimental test station, shown in Figure 3.1, has a generic capability for making photoresponse measurements and its use is intended for use on several different programs as a spectrophotometer for measuring photoresponse of superconducting and semiconducting photodetectors. The operation of the test station and data recording is computer controlled using the LabView for Windows software package. The optics, designed to operate over a very wide spectral band ($3\mu\text{m}$ - $100\mu\text{m}$), are described in section 3.1. The cryogenic test station is designed to operate between 5-300K and is described in section 3.3. Such operating characteristics are compatible with testing superconducting quantum photodetectors under development on this program. Part of the experimental test station's electrical subsystem was specifically designed for interface with a SQUID readout from QSKIP, and this is described in section 3.2. A special packaging approach for handling the QSKIP was developed and this is described in section 3.4. Finally, in section 3.5. we describe the experimental results on the QSKIP.

3.1 OPTICAL SETUP

The optical setup, assembled on an aluminum breadboard table, includes: (1) a monochrometer, (2) reflecting optics, (3) cooled long pass filters, (4) optical windows, (5) thermopile reference sources, (6) black body source, and (7) chopper. A diagram of the optical setup, including the black body source, focusing optics, and monochrometer is

shown in Figure 3.2. Also included in this diagram are the location of the optical elements in the dewar. The optical elements in the dewar include: (1) a window, (2) cooled (77K) filters and attenuators, (3) gold coated mirrors for sampling the incident and reflected optical beam onto thermopiles (not shown) cooled to 77K, and (5) the sample location. The sample is located on a cold stage whose temperature can be varied from 5-300K. A description of the components used and their operation follows.

The **black body source** is made up of a tungsten filament operated at 2400K. The filament selected is from an OSRAM Halogen projector lamp part number HLX 64655 EHJ. This lamp is rated to operate at 3400K and puts out 10^4 lumens for an average life of 50 Hours. The filament is enclosed in a quartz envelope and operates from a 24 DC power supply. To use this lamp as a black body source, we first removed the quartz envelope because it does not transmit much beyond $4\mu\text{m}$. The tungsten filament was enclosed in a specially made vacuum box that had provisions for replaceable optical windows and powering of the filament. The replaceable optical windows included KRS-5 ($0.6\mu\text{m}$ - $40\mu\text{m}$), clear ZnSe ($0.3\mu\text{m}$ - $18\mu\text{m}$), and single crystal silicon ($1.1\mu\text{m}$ - $300\mu\text{m}$, with a blocking band between $12\mu\text{m}$ - $40\mu\text{m}$). These windows allow transmission of black body radiation over a very broad spectral band and in particular the $3\mu\text{m}$ - $100\mu\text{m}$ spectral band we are interested in.

To maintain a longer life, the tungsten filament was operated at a lower voltage than its rated 24 volts. The tungsten filament was enclosed in the vacuum box and evacuated. The vacuum box was backed filled with an inert gas to a pressure of about 30 psi. This provided two advantages: (1) the window coating rate from the evaporation of

the hot tungsten filament was reduced, and (2) the filament could be operated hotter. Out of Argon, Krypton and Xenon we selected Krypton because Xenon was too expensive. With this design the filament and the optical windows provided us with a broad spectral source.

Only **Reflective optics** are used to focus the black body radiation onto the monochrometer entrance slit. Two gold coated 90^0 off-axis paraboloidal mirrors (part # 02 POA 013), from Melles Griot, collimate and refocus the black body radiation onto the monochrometer's entrance slit. A metal blade chopper, located less than 3mm in front of the monochrometer entrance slit, modulates the black body radiation. The radiation entering the monochrometer is filtered by a grating before it emerges at the monochrometer's exit slit.

Six-gold coated gratings spectrally filter and provide radiation within the $3\mu\text{m}$ - $100\mu\text{m}$ spectral band of interest. The six gratings are assembled on two turrets with each turret holding three gratings. The monochrometer, model SpectraPro-275 from Acton Research Corporation, holds one three-grating turret at a time. Each turret is easily installed in the monochrometer and no realignments are required. This six-grating set covers the $3\mu\text{m}$ - $100\mu\text{m}$ spectral band as listed in Table 3.1. Turret number 1 contains gratings (1) through (3) spanning $3\text{-}30\mu\text{m}$. Turret number 2 contains gratings (4) through (6) spanning $30\text{-}100\mu\text{m}$. The monochrometer is used to select a narrow wavelength band (with higher order harmonics) from the spectrally broad band of black body radiation, and this optical signal is collimated at the monochrometer exit slit with a Melles Griot gold

coated 90° off-axis paraboloidal mirror (part # 02 POA 013). The collimated optical signal reaches the photodetector through the dewar's optical window, shown in Fig.-3.3.

#	Grooves /mm	Blaze wavelength	Acton part #	Operating Band	$\Delta\lambda$ (for 3mm slit)
1	150 g/mm	4 μ m	1-015-4	3-6 μ m	72nm
2	75 g/mm	10 μ m	1-075-10	6-16 μ m	144nm
3	20 g/mm	22.5 μ m	1-02-22.5	16-30 μ m	540nm
4	20 g/mm	45 μ m	1-02-45	30-55 μ m	540nm
5	13.3 g/mm	67 μ m	1-013.3-67	55-85 μ m	810nm
6	7.9 g/mm	112 μ m	1-07.9-112	85-168 μ m	1365nm

Table 3.1. Operating characteristics of gratings used in this program. The first three gratings were mounted on turret number 1 and the last three are mounted on turret 2.

Filter #	Part Number	Cut-on λ	Transmission @ λ Cut-on
1	PN LP-3000-F	3 μ m	5%
2	PN LP-6000-F	6 μ m	5%
3	4-8 μ m P-12	12 μ m	20%
4	5-10 μ m P-16	16 μ m	35%
5	8-16 μ m P-22	25 μ m	20%
6	15-25 μ m P-40	40 μ m	20%
7	30-40 μ m P-62	62 μ m	20%

Table 3.2. Long pass filters use in set-up. Filters # 1 and # 2 are from the Infrared Optical Products, Inc. Filter # 3, #4, #5, and #6 are from Infrared Laboratories, Inc.

Inside the dewar (see Figure 3.3) the collimated optical beam is filtered to remove the higher order harmonics. Seven long pass filters are needed to operate over the 3 μ m-100 μ m spectral band, and these are listed in Table 3.2.

The filters, 1" in diameter, are mounted in an eight-position wheel and cooled to 77K. With a knob, mounted outside the dewar, we place one of the seven filters (or no filter) in the optical beam path. Cooling these filters to 77K greatly reduces self black body radiation. A second wheel, (cooled to 77K and located in front of the filter wheel and inside the dewar) contains neutral density attenuators that pass 10% and 1% of the

incident optical radiation. The second wheel is independently controlled with a second knob mounted outside the dewar. This two wheel arrangement allows us to filter out the higher order harmonics and attenuate the narrow-band optical signal. The filter and grating combinations used for spanning the 3 μ m- 100 μ m are listed in Table 3.3. The last column indicates the location of the filters in the wheel so the knob mounted outside the dewar can be used to set the dial at the appropriate number (or filter). In Table 3.4, the knob settings for the wheel with the attenuators are listed in the last column.

Operating Band	# Grating & Part	Filter	Knob Setting
Open	n/a	None	240
3-6 μ m	(1) 1-015-4	PN LP-3000-F	340
6-12 μ m	(2) 1-075-10	PN LP-6000-F	440
12-16 μ m	(2) 1-075-10	4-8 μ m P-12	540
16-26 μ m	(3) 1-02-22.5	5-10 μ m P-16	640
26-30 μ m	(3) 1-02-22.5	8-16 μ m P-22	740
30-45 μ m	(4) 1-02-45	8-16 μ m P-22	740
45-55 μ m	(4) 1-02-45	15-25 μ m P-40	840
55-70 μ m	(5) 1-013.3-67	15-25 μ m P-40	840
70-85 μ m	(5) 1-013.3-67	30-40 μ m P-62	940
85-100 μ m	(6) 1-07.9-112	30-40 μ m P-62	940

Table 3.3. Arrangement of Filters and Gratings for operating in 3-100 μ m spectral band. Once the operating band is selected, the corresponding grating is rotated into place in the monochrometer and the appropriate filter in the dewar is rotated into the beam path with the knob on the dewar.

After being spectrally filtered inside the dewar, the filtered optical signal is divided into three parts. One part is reflected by a gold mirror and is used as a reference. A second part is reflected from a thin film held at the same temperature as the photodetector. The thin film is from the same material as the photodetector. The third part of the filtered optical signal reaches the photodetector located on the cold stage.

Two thermopiles (operated at 77K and mounted on a cross member located inside the dewar's radiation shield, shown in Figure 3.3), are used to measure the intensity of the incident and reflected beams the detector's normalized photoresponse to be is computed. Both thermopiles are model 2M, manufactured by Dexter Research Center. Improved thermopile responsivity is realized because they are operated in a vacuum and at 77K. The responsivity of both thermopiles have been calibrated with a HeNe laser. The responsivities of the thermopile used to measure the incident filtered optical signal is 1425.5 Volts/Watt. The responsivity of the thermopile used to measure the reflected optical signal from the photodetector is 1104.19 Volts/Watt. The thermopile output signals are amplified and recorded on a PC. The electrical setup is described in the next section.

Operating Band	Function	Characteristics	Knob Setting
3-100μm	Open	Open	910
3-100μm	Attenuator	1% Pass	810
3-100μm	Attenuator	10% Pass	710
3-100μm	Open	Open	610
3-100μm	Open	Open	510
3-100μm	Open	Open	410
3-100μm	Open	Open	310
3-100μm	Open	Open	210

Table 3.4. Arrangement of attenuators in the second wheel. Out of the eight positions in this wheel only two are used, for the 1% and 10% neutral density attenuators. With the two wheel arrangement, these attenuators can be placed in series with the filters to vary the intensity of the filtered optical beam. For the present set-up we only placed two attenuators (1%, and 10%) inside the second filter wheel.

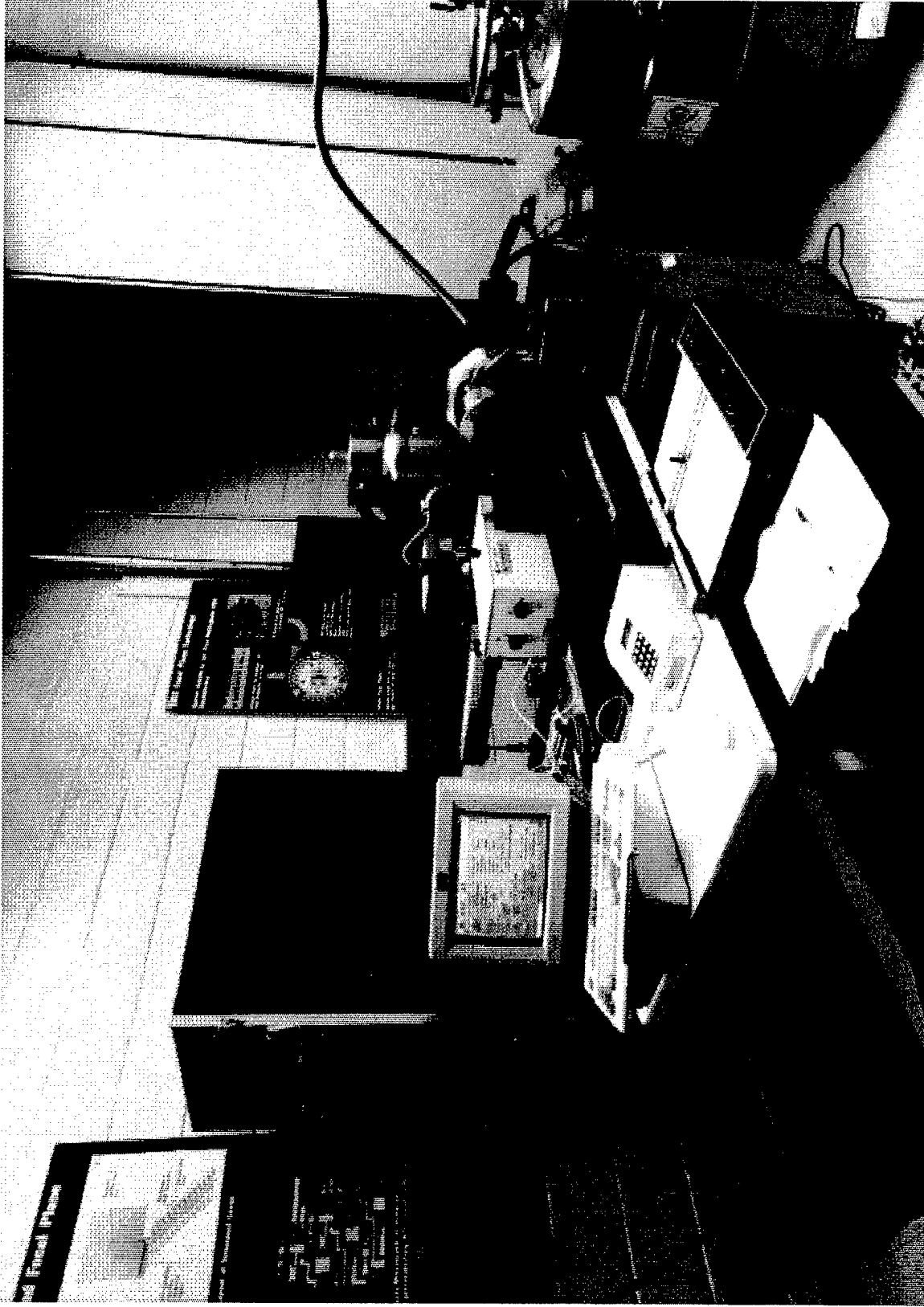


Figure 3.1. Shown is the experimental test station for measuring photodetector photoresponse. The dewars shown in the background are used to cool the radiation shield to 77K and the cold finger as low as 5K. Also visible are the electronics, dewar, optics and computer control.

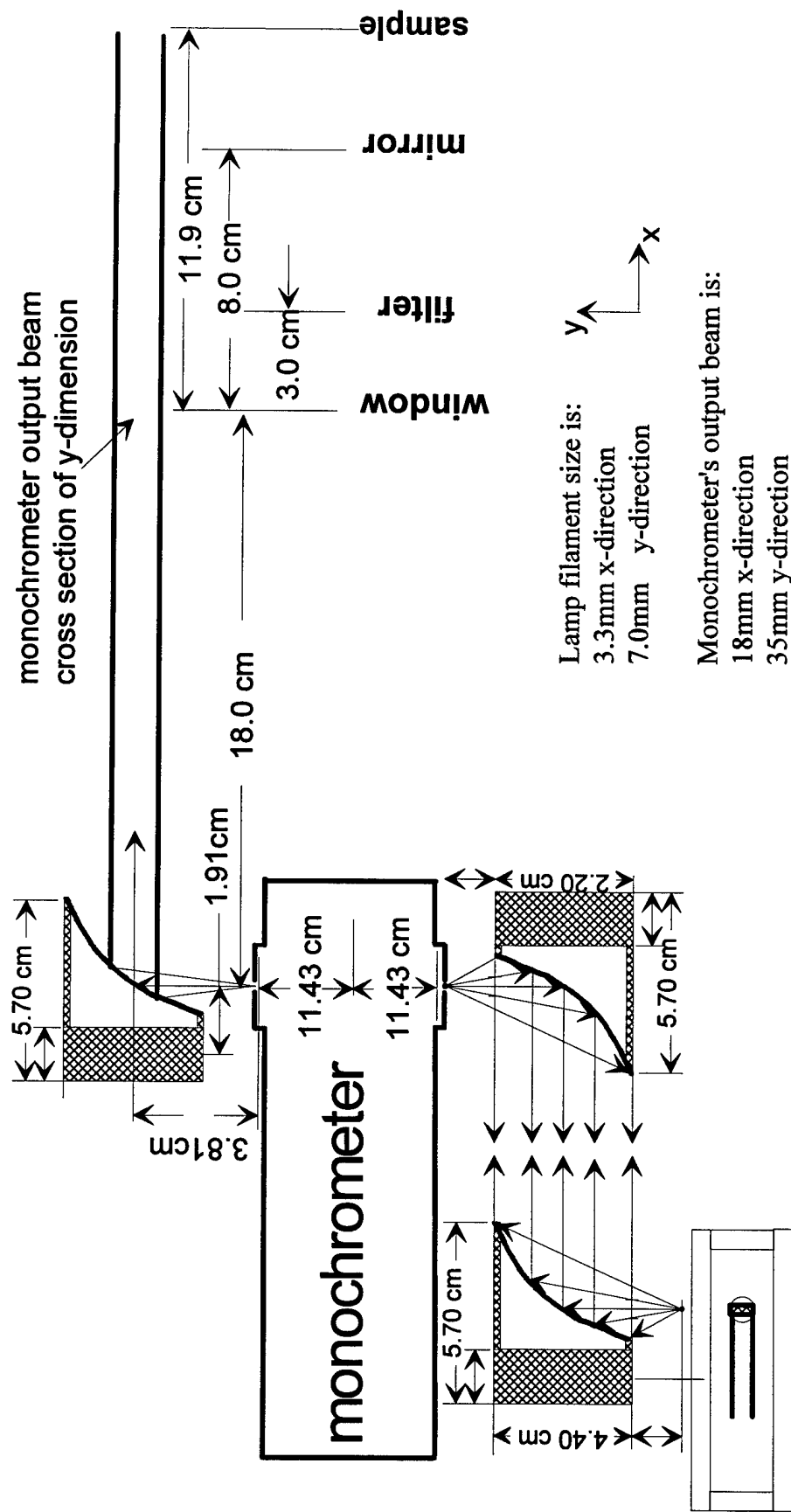


Figure 3.2. The layout of the optical system is shown, including: the monochromator, the paraboloidal mirrors, and the location of the dewar components.

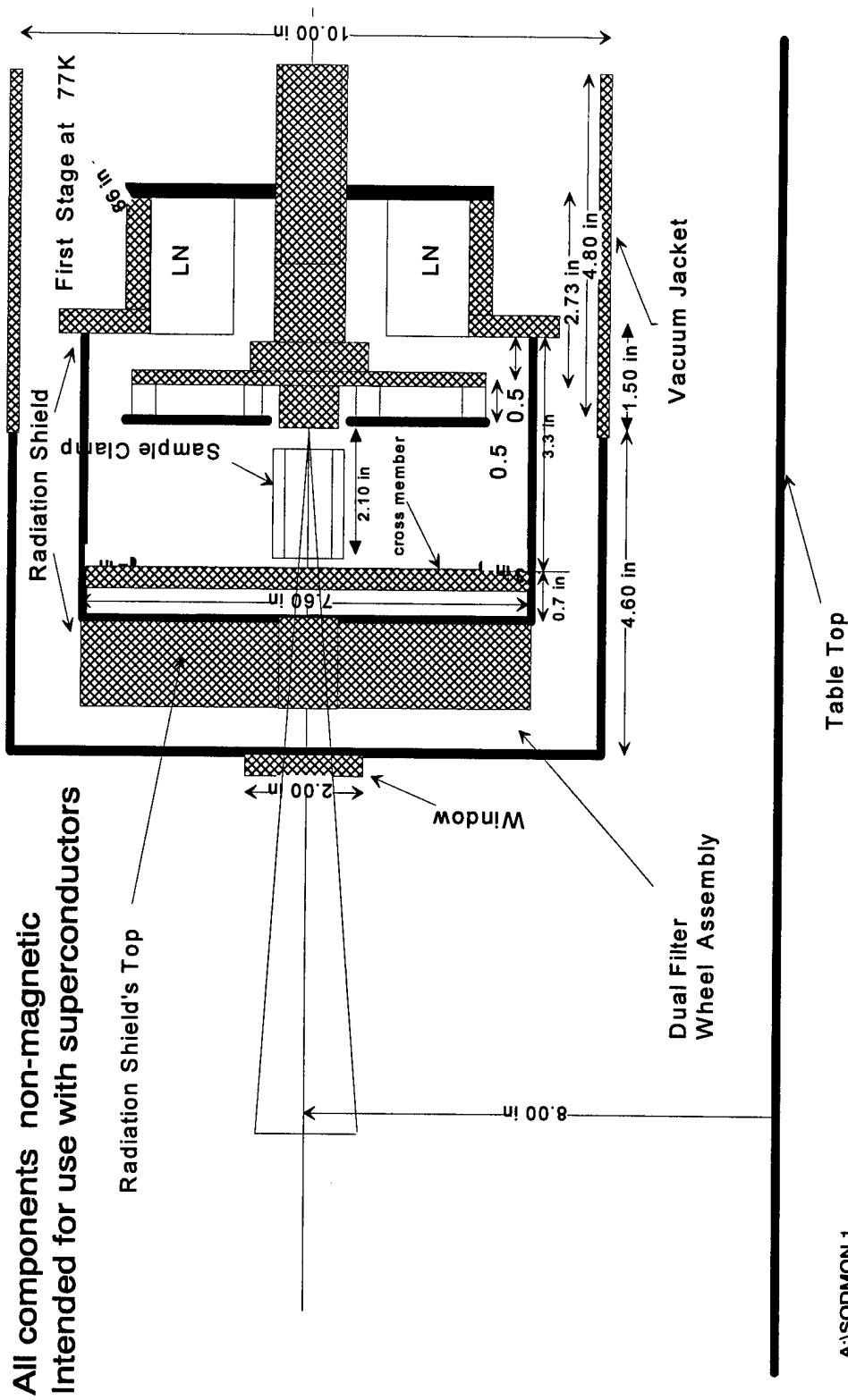


Figure 3.3. Details of the dewar design are shown, with the extra liquid nitrogen tank to cool the radiation shield to 77K. The cold finger is cooled by helium to as low as 5K. The dual filter wheel assembly is attached to the top of the radiation shield. A cross member below the dual filter wheel assembly contains the two thermopiles used to measure the incident and reflected optical beams.

3.2 ELECTRICAL SETUP

The electrical setup included provisions for: (1) PC data acquisition, (2) signal processing electronics, (3) photodetector bias circuits, (4) electrical interface to the optical elements, and (5) control and monitoring of dewar temperature. A significant effort was required for the electrical subsystem and this is described next.

PC data acquisition is used to control the entire experimental setup. A PC with a 486 microprocessor is used to operate the equipment through the GPIB. Incorporated into the PC are two cards made by National Instruments: (1) an AT-GPIB interface for IBM PC/AT EISA Bus PC including NI-488.2, and (2) a multifunction Analog and Digital I/O Bus for IBM PC, model AT-MIO-16L-25. The computerized data acquisition software is based on National Instruments LabView for Windows. All the electronics are initialized through the PC computer interface, with provisions for a manual override. The initial settings have been programmed into the Virtual Instruments (VI) formed with the LabView software. The VI represents all the electronic instruments on the PC CRT screen and provides control knobs for operating these through the GPIB. Once the photodetector sample has been cooled and properly biased, the data recording is made with the PC. The PC through the GPIB reads many different parameters from the instruments and these are listed in Table 3.5. The reason for all these reading follow.

The first three rows are used to establish the AC incident photon flux. The incident flux is measured with a 77K thermopile when the chopper blade is open and closed. The difference between these reading gives us the change in photon flux and this

is used to compute the AC photocurrent response. The AC measurement is used to remove the background photon flux which is very significant in the 3-100 μ m spectral band.

#	Label	Purpose
1	High Incident Photon Reading	Incident flux recording with chopper blade open
2	Low Incident Photon Reading	Incident flux recording with chopper blade closed
3	Delta 1-2 COMPUTATION	Incident flux AC amplitude computation
4	High Reflected Photon Reading	Reflected flux recording with chopper blade open
5	Low Reflected Photon Reading	Reflected flux recording with chopper blade closed
6	Delta 4-5 COMPUTATION	Reflected flux AC amplitude computation
7	Detector High Voltage Reading	Voltage across detector with chopper blade open
8	Detector Low Voltage Reading	Voltage across detector with chopper blade closed
9	Delta 7-8 COMPUTATION	Voltage change across SC should remain ZERO
10	Detector High Bias Current	Measures bias current with chopper blade open
11	Detector Low Bias Current	Measures bias current with chopper blade closed
12	Delta 10-11 COMPUTATION	Insures bias current remains the same
13	Detector Temperature	Reads the detector's temperature
14	SQUID Temperature	Reads the cold finger's temperature
15	Cold Shield Temperature	Reads the radiation shield's temperature
16	Thermopile Temperature	Reads the thermopile's temperature
17	SQUID Bias Current	I _c SQUID bias current
18	SQUID High Current Reading	Current used to balanced SQUID with blade open
19	SQUID LOW Current Reading	Current used to balanced SQUID with blade closed
20	Delta 18-19 COMPUTATION	AC photocurrent amplitude
21	Photon Wavelength	Provides spectral band of incident photon flux
22	DC Lock-in Null Signal	Error signal, zero if 18 & 19 are adjusted OK
23	SQUID Flux Bias	Net SQUID bias including Lock-in error signal
24	Lamp Voltage	DC Bias voltage on Black Body lamp source

Table 3.5. The readings and computations recorded with the PC data acquisition system, used to measure the photodetector's photoresponse, are listed in 24 rows.

Rows 4 through 6 are used to establish the AC reflected photon flux. The reflected photon flux is measured with a 77K thermopile with the chopper blade open and closed. The reflected photon flux is normalized by the corresponding incident photon flux. The difference between these readings yields the percentage of photon signal which is

reflected. With the calculated AC reflected photon signal we compute how much photon flux is absorbed by the photodetector to produce the observed photocurrent signal.

Rows 7 through 9 are used to monitor the voltage across the superconducting photodetector. Two readings are made, one with the chopper blade open and a second one with the chopper blade closed. If the superconducting photodetector remains in the zero resistance state (or current state) the difference between these two readings is zero. Taking a difference between two reading circumvents the issue of removing DC offsets present in the voltage reading. If the difference between the two readings is not zero it indicates that the photodetector is not operating in the zero resistance state.

Rows 10 through 12 are used to monitor the current bias of the superconducting photodetector. Two readings are made, one with the chopper blade open and a second one with the chopper blade closed, to account for any drift in the detector bias current . If the detector bias current remains constant, zero will be the difference between these two readings. The combination of the voltage and current readings is our check to ensure that during different levels of photoillumination the detector remains in the zero resistance superconducting state and the bias current is constant.

Rows 13 through 16 provide temperature information on the photodetector and dewar. Row 13 represents the temperature from a diode thermometer mounted inside a leadless chip carrier package containing the photodetector. Row 14 is the temperature of silicon diode sensor thermally attached to the cold stage. The temperature of the radiation shield is recorded on line 15 and we assume that it corresponds to the temperature of the

thermopiles which are attached to the radiation shield. Row 16 is for adding a second temperature sensor for specifically measuring the temperature of thermopiles, which are bolted to the cross member attached to the radiation shield.

The SQUID bias current is recorded in row 17. The bias current is manually adjusted for placing the SQUID in the voltage state and at maximum sensitivity.

Rows 18 through 20 monitor the needed offset current for balancing the photodetector signal and placing the SQUID in the symmetrical operating mode. The offset current is adjusted with the chopper blade open (Row 18) and the chopper blade closed (Row 19). The difference between these readings (Row 20) represents the photodetector AC photoresponse current. This photoresponse is normalized with the incident flux level obtained from Rows 1-6. The number of photons incident are calculated from the wavelength (Row 21) and the spectrophotometer spectral bandwidth $\Delta\lambda$ given in Table 3.1.

The total offset current flowing in the SQUID is automatically trimmed with a lock-in feedback circuit and the trim offset current level is given in Row 22. The total offset current is a sum of the manually adjusted offset current level and the lock-in contribution, and this is given in Row 23. The voltage used to power the black body tungsten lamp is listed in Row 24.

It should be evident that each data point recorded with the computer data acquisition system is extensive. Such a practice permits better data analysis and proper operation of the superconducting photodetectors.

The **Signal Processing Electronics** consist of IC preamplifiers and off-the-shelf electronics. The IC preamplifiers, housed inside a breakout aluminum box attached to the dewar, provide gain to improve noise immunity and reduce outside interference. The output from the preamplifiers is channeled to the computer data acquisition system through off-the-shelf electronics.

The signal processing electronics include: (1) a Keithley 182 nanovoltmeter with an IEEE 488 interface, (2) a Keithley 705 scanner with a 7160 nanovolt scanner card and IEEE 488 interface, and (3) an Ithaco 3970 electro optical lock-in measuring system. These instruments receive the outputs from the preamplifiers connected to the superconducting photodetector as shown in Figure 3.4. The photodetector is located inside the dashed lines drawn in Figure 3.4.

The **photodetector bias circuits** are illustrated in Figure 3.4 and the details are shown in Figure 3.5. A DC current $I(\text{QSKIP})$ biases the photodetector. The signal developed is sensed with a SQUID located at the photodetector base. The SQUID is biased with a DC current I_C (SQUID). The construction of the photodetector and the readout SQUID are symmetrical to provide a differential output between the illuminated and covered portions of the photodetector. With such a differential operation, the SQUID bias circuits provide bi-directional flux bias (see Figure 3.5) that apply positive and negative currents to different ends of the SQUID. The combination of offsetting positive and negative SQUID bias currents minimizes ground currents. The bi-directional DC and AC flux modulating currents are produced through two $10.2\text{K}\Omega$ resistors. The amplitude and phase of the SQUID flux nulling currents are adjusted to be equal in amplitude and

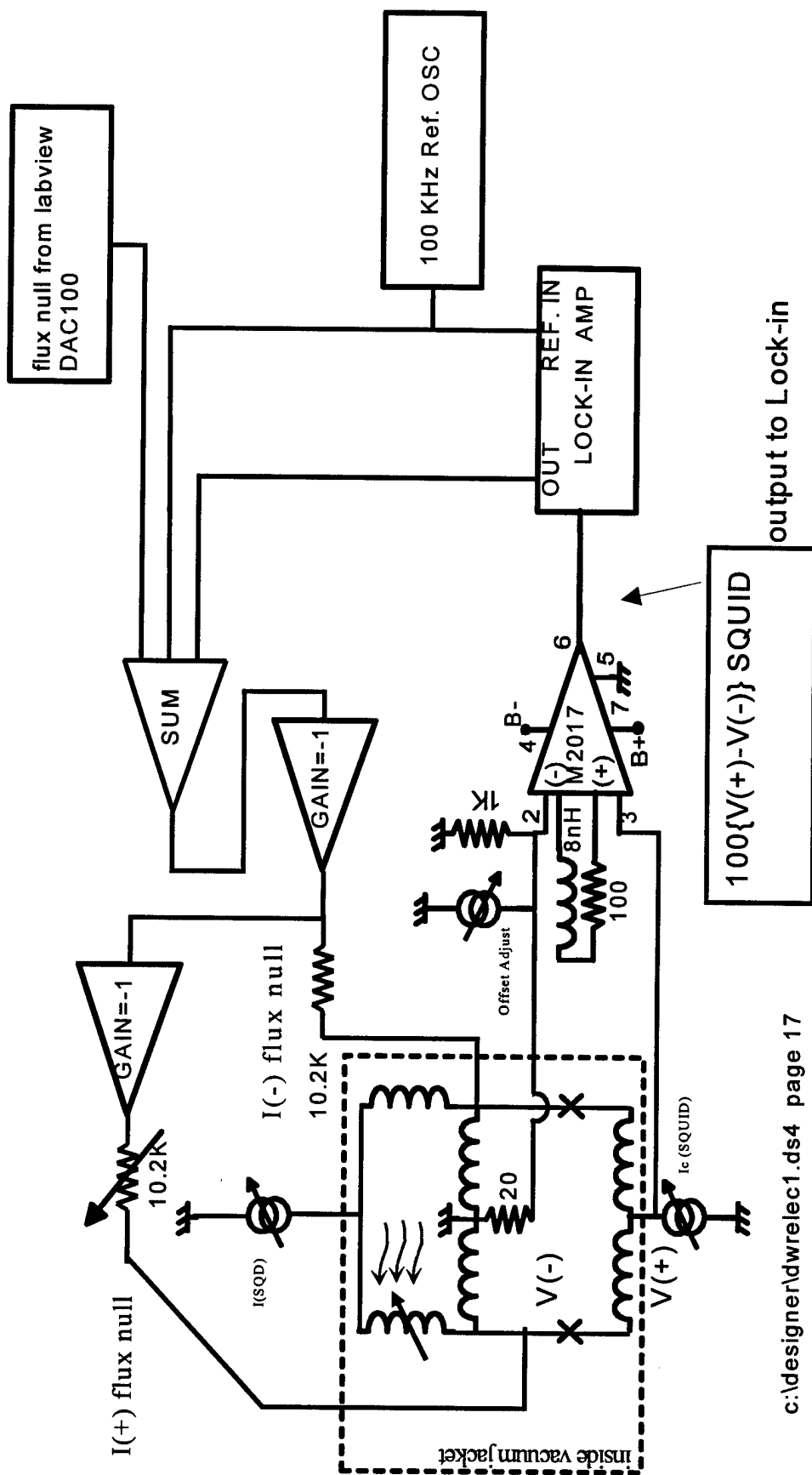


Figure 3.4. Diagram of preamplifier, Lock-in and photodetector bias circuits used for making photoresponse measurements.

180° out of phase with a variable resistor and capacitor (see Figure 3.5). The flux nulling circuits sum three inputs. These inputs are: the AC flux modulation signal, the V(+) null signal from the lock-in, and the manually controlled DC SQUID flux bias adjust from the Lab-view DAC. Since the photodetector is DC coupled to a high gain preamplifier, provisions have been included for manually removing any DC offsets that may saturate the preamplifier. At the preamplifier input, an "offset adjust" current through a 20Ω resistor provides a small voltage to null out DC offsets. The preamplifier is directly coupled to the SQUID to facilitate characterization of the SQUID's I-V curves. The SQUID preamplifier is an audio IC amplifier with a spectral voltage noise density of less than 1nV/√Hz.

The **electrical interface to optical elements** includes: the monochrometer, the chopper, the black body tungsten filament, and two thermopiles. The Acton Research monochrometer has an electronic control module that interfaces through an IEEE 488 bus with the PC computer to record the operating wavelength. The HMS light beam chopper 220 interfaces to the computer through the National Instruments AT-GPIB interface for IBM PC/AT EISA Bus PC including NI-488.2. The Black body tungsten filament is powered by a remote controlled Sorensen SRL 20-12 power supply (0-25VDC, 0-15 Amp). The Sorensen power supply has manual and automatic control options. The output of the supply is adjusted to maintain a fixed photon flux level as determined by the two thermopiles inside the dewar. Each thermopile is connected to special preamplifier circuit with a gain of 11 (see Figure 3.6) and are calibrated to read the incident photon flux

power. Capacitive loading from the coaxial shield is reduced by unity gain preamplifier circuits.

The **temperature control and monitoring** is centered around two Lake Shore 93CA temperature controllers connected via an IEEE 488 bus to a PC. Each controller accepts inputs from two temperature sensors and can power one heater. The heater output in combination with either temperature sensor provides for temperature control. The heater output is a proportional analog signal (not digital) to minimize heater induced electrical interference. The temperature sensors are calibrated silicon diodes with a temperature range between 2K and 300K. The sensor's calibration curves are entered inside the 93CA to provide, at low temperatures, a resolution better than 0.1K.

3.3 CRYOGENIC SETUP

The dewar used in this setup was a model MTD 150 made by Lake Shore Cryotronics (see Figure 3.3). The dewar includes 100 coaxial electrical inputs for electrical access to the packaged sample, and includes a socket designed to accept packaged devices in a leadless chip carrier (LCC) 84-pin package. A square hole is machined inside the socket to accommodate an aluminum pedestal which is attached to the cold finger. Several modification were made to this dewar and they are described.

The original dewar arrangement made use of a single clamp to make electrical and thermal contact between the LCC package and the dewar's socket and aluminum pedestal. We have incorporated two independent pressure clamps to electrically and thermally contact, respectively, the LCC package to the socket and the aluminum pedestal. The LCC socket is soldered to a small printed circuit board which is attached to

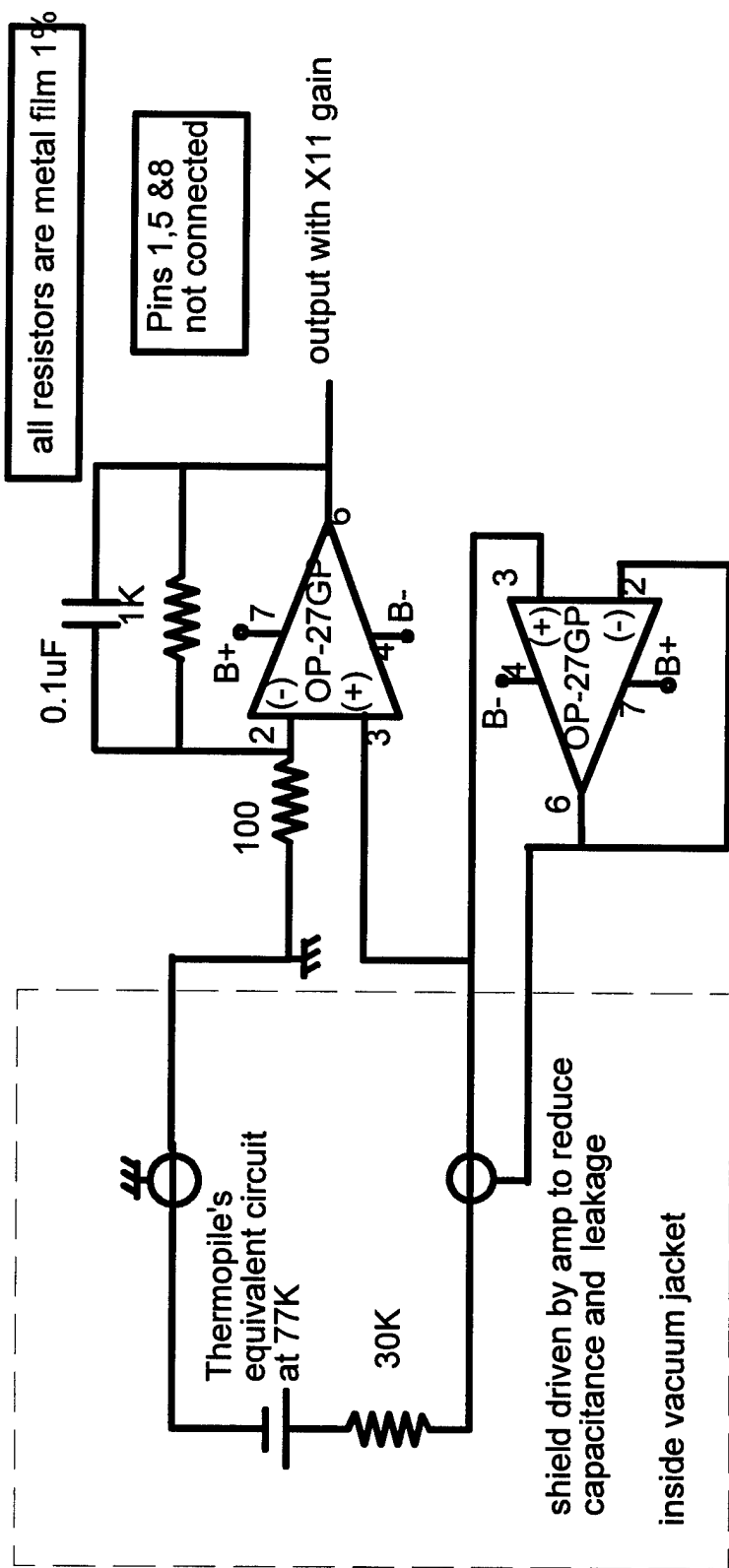


Figure 3.6. Circuit diagram of preamplifiers used to readout the thermopiles. One amplifier provides a voltage gain of 11 to the thermopile output signal. A second amplifier drives the coax shield to reduce the effective shunting capacitance across the thermopile and thus extend the frequency response.

a second fan-out board with flexible thin wires. The small printed circuit board has provisions for attaching a clamp that clamps down the LCC package inside the socket. This clamp is independent of a second clamp which is used to press the package/socket assembly onto the aluminum pedestal and make good thermal contact. With two spring loaded clamps good electrical and thermal contact are independently established. This is important given the fact that the packaged devices are loaded into the dewar at room temperature and cycled between 5-300K. Cycling devices over such a wide temperature range requires provisions for accommodating mechanical mismatches in the thermal expansion coefficients. The two clamps provide the additional degree of freedom to accomplish this feature.

The modified dewar included two separate cryogenic inputs. The radiation shield, the two filter wheels, and the thermopiles were cooled by liquid nitrogen through separate cryogenic lines. This permitted us to cool most of the dewar mass with liquid nitrogen and saved both cool down time and liquid helium consumption. The second cryogenic input was from liquid helium that allowed us to cool the sample to about 5K. In operation, liquid nitrogen and liquid helium were transferred at the same time to speed up cool down. After cool down, the liquid nitrogen valve was turned off and the radiation shield remained close to 77K. The cold finger temperature was varied between 5-77K.

To reduce electrical interference, a Mu-metal magnetic shield was incorporated in the dewar. The shield, purchased from Advance Magnetics, was custom designed and made from RMA 1084 material. The shield was assembled from several pieces so it could

be incorporated into the dewar. As designed the shield was easily added to the dewar after all the electrical, cryogenic, vacuum, and optical elements were incorporated.

As configured, the dewar was routinely used to cool down and measure photodetectors down to 5K. However, operation at 5K required reducing the thermal load from the 100 coaxial lines. For testing single photodetectors, 25 coaxial lines were sufficient and 75 coaxial lines were disconnected from the cold finger stage to significantly reduce the thermal load. The 75 lines can be readily reattached by removing three plastic inserts.

3.4. DETECTOR PACKAGING

Testing of the QSKIP requires provisions for dealing with large thermal expansion mismatch between the photodetector and package material. Additionally, operation at liquid helium temperatures requires excellent thermal contact between the package and the cold finger. We developed a method, on Westinghouse funds, for packaging superconducting IC's in modified ceramic packages, which resolves the thermal expansion mismatch and reduces thermal drops across the package.

The packaging approach is compatible with conventional bonding of integrated circuits into packages that fit in conventional sockets. The socket used is for an 84 pin LCC package, Kyocera part number PB-0289, and is integrated into the Lake Shore Cryotronics MTD-150 open cycle dewar.

The thermal mismatch is resolved by using a metallic base material (for good thermal conductivity) that has an thermal expansion coefficient close to the substrate the superconductor material is grown on, typically LaAlO_3 or NdGaO_3 . Table 3.6 lists

thermal expansion coefficient for several materials. For a LaAlO_3 substrate, beryllium, niobium and tantalum offer very good thermal matches (1300 vs 1300, 1290, and 1279). Niobium and tantalum are potentially good choices. However, as niobium becomes superconducting at 9.2K (vs 4.43K for tantalum) its thermal conductivity also begins to decrease drastically at 9.2K. Therefore, for operating down to about 4.5K we chose to use tantalum.

MATERIAL	$\Delta L/L \times 10^6$	MATERIAL	$\Delta L/L \times 10^6$
LaAlO_3	1300	SS Monel	2450
Niobium	1290	SS 301	2300
Tantalum	1270	SS 321	2600
Molybdenum	894	SS 316	2770
Iron Fe	1890	SS 304	2790
Beryllium	1300	Titanium	1700
Aluminum	3910	Poly-Alumina	791

Table 3.6. Total thermal contraction difference $\Delta L/L$ between 300K to 77K for different candidate substrate.

Incorporating a tantalum base into the 84 pin LCC alumina package requires package modification. A 1 cm diameter hole was drilled in the 84 pin LCC package to remove the alumina that the IC is normally mounted on (see 3.7). The hole was sufficiently small to be confined within the package well and thus not damage the electrical lines inside the package. The hole removes the bottom of the IC well which is replaced by the tantalum base (see Figure 3.7).

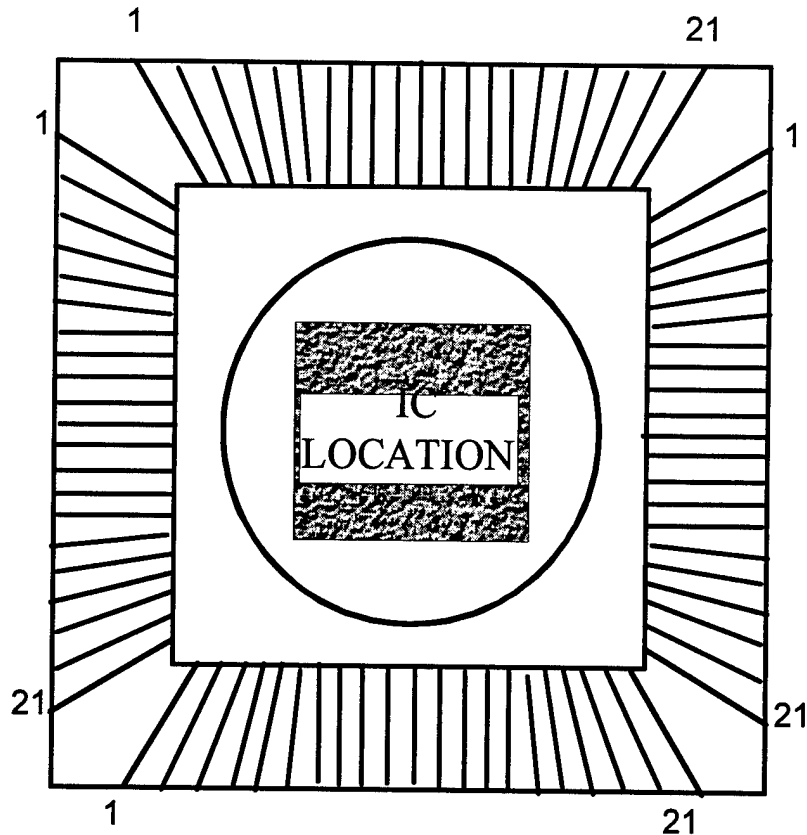


Figure 3.7. Schematic of 84 pin leadless chip carrier package with hole drilled in IC cavity. The hole, indicated by the circle, is 1 cm in diameter, which is sufficiently large for the IC to fit inside.

The base is made from approximately 0.05cm thick tantalum sheet cut into a 2.4 cm square. The 2.4 cm square size is sufficiently small to fit within the electrical contact frame located on the back of the ceramic package, about 2.86 cm square. The processing and assembly needed to incorporate this tantalum base are described next.

A tantalum sheet is first plated with about 10 μ m of copper on both sides and then cut into 2.4 cm squares. The plated tantalum squares receive about 120 μ m of Indium on the front side, for a total base thickness of about 620 μ m. The QSKIP devices are soldering to the indium-coated tantalum base. The soldering is performed by placing the device (with a gold coated back) on a SnInCd solder preform in the center of the indium-

coated tantalum base. This assembly is placed into an oven and heated to 130°C and cooled to room temperature. This thermal cycle solders the Multispectral QSKIP device to the indium-coated tantalum base with the SnInCd solder whose melting temperature is 95°C. The tantalum base with the Multispectral QSKIP device is glued to the back of the ceramic package as shown in Figure 3.8.

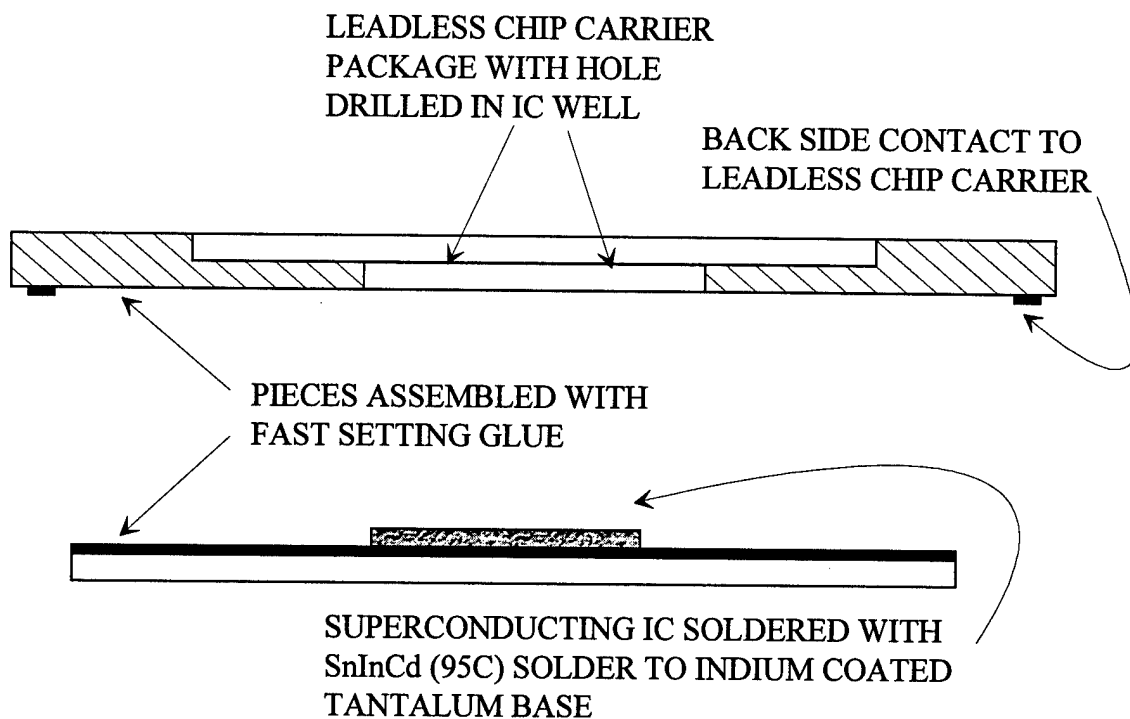


Figure 3.8. Illustration of assembly of indium-coated tantalum base, with IC attached, before being glued to back of ceramic package.

With this assembly, the soft indium, located between the tantalum base and the alumina LCC package, provides mechanical compliance to accommodate thermal expansion mismatch. The fast setting glue, (Super Bonder 495 made by Loctite) is used for ease of assembly. When the QSKIP device, the tantalum base, and package are assembled, ultrasonic bonding is used to bond the Multispectral QSKIP to the LCC

package frame. The completed assembly is shown in Figure 3.9, with the electrical contact pads exposed on the back. With this arrangement, the electrical contact between the socket and LCC package is through the original contact pads, located on the package's back side.

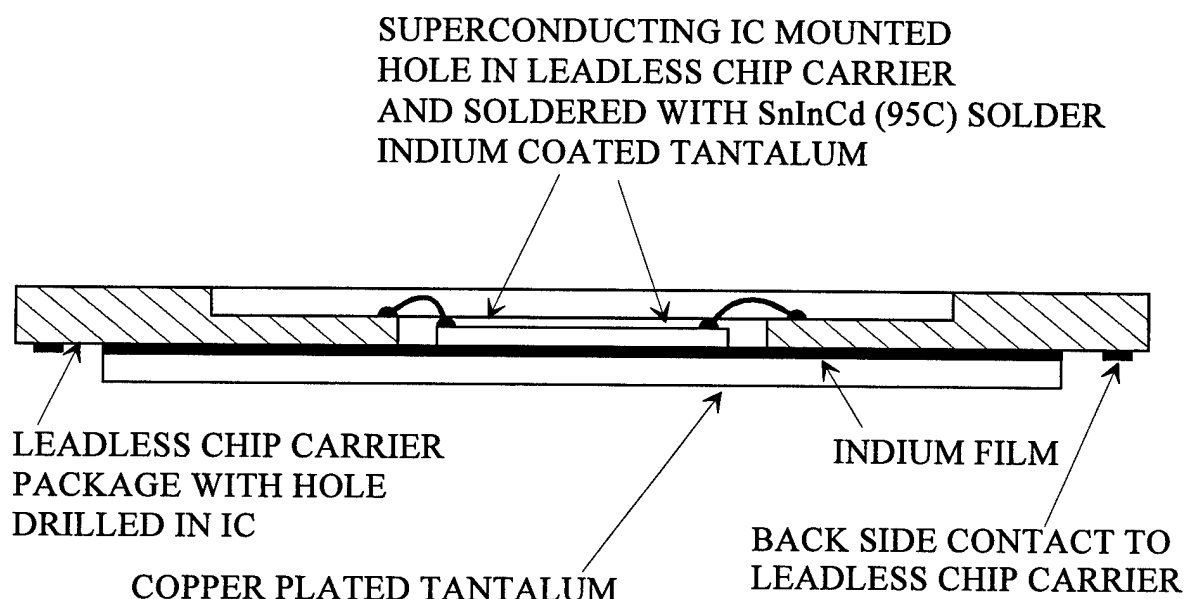


Figure 3.9. Assembly of tantalum base, with IC soldered to it, glued to the back of a ceramic package pre-drilled with a hole in the IC well.

The packaging scheme has been implemented and QSKIP devices have been placed in a dewar and cooled down to about 5K. Unlike previous approaches, the QSKIP device did not shear off the tantalum base after several cycles between 300K and 5K. This is a significant improvement over previous attempts where the QSKIP was placed directly inside a 84 pin ceramic package. This technique is appropriate for packaging different IC made with high and/or low temperature superconductors.

3.5 DETECTOR TESTING AND RESULTS

The Multispectral QSKIP fabricated and tested in this program is represented by the diagram shown in Figure 2.2 and the photograph shown Figure 3.10 and 3.11. In this section we start the QSKIP structure and follow with experimental measurements taken on photodetectors pictured in Figure 3.10. The Multispectral QSKIP did not exhibit photoresponse to light and we examine potential reasons for this.

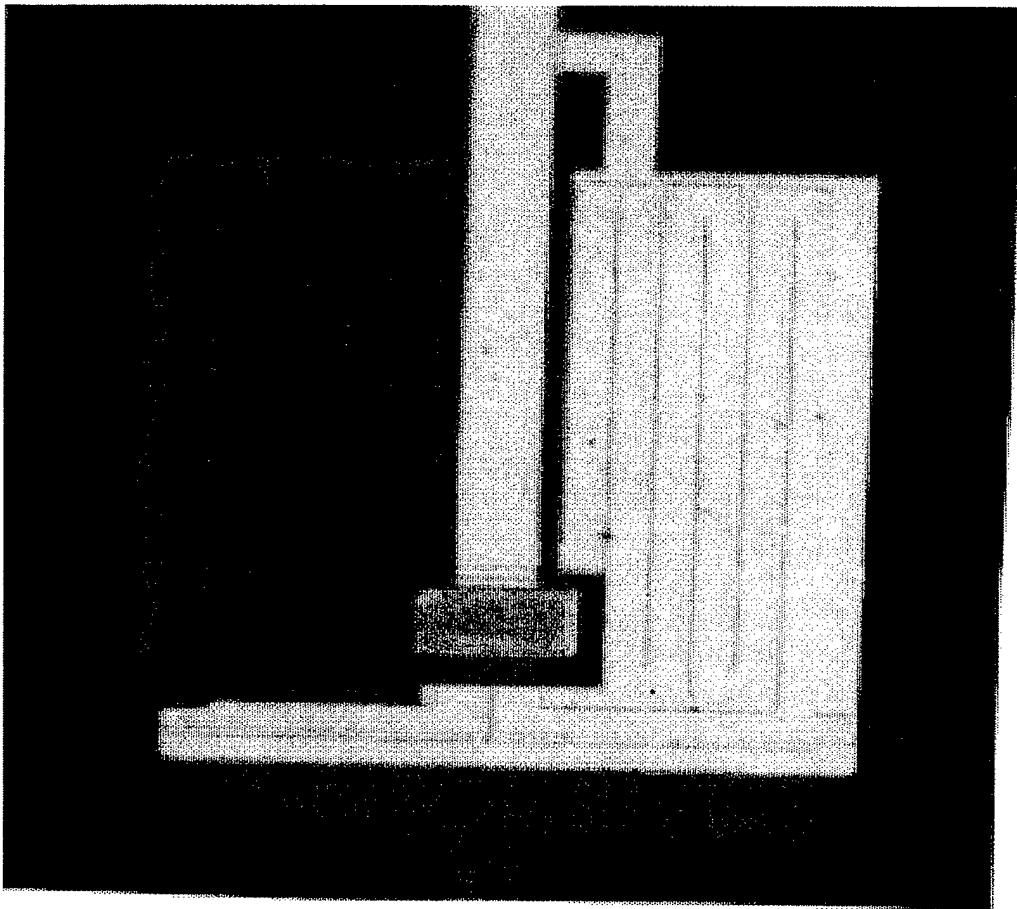


Figure 3.10. A photomicrograph of the Multispectral 100x100µm QSKIP designed and fabricated in this program. The photodetector is made of symmetric YBCO serpentine left and right portions with a YBCO SQUID readout located at the bottom.

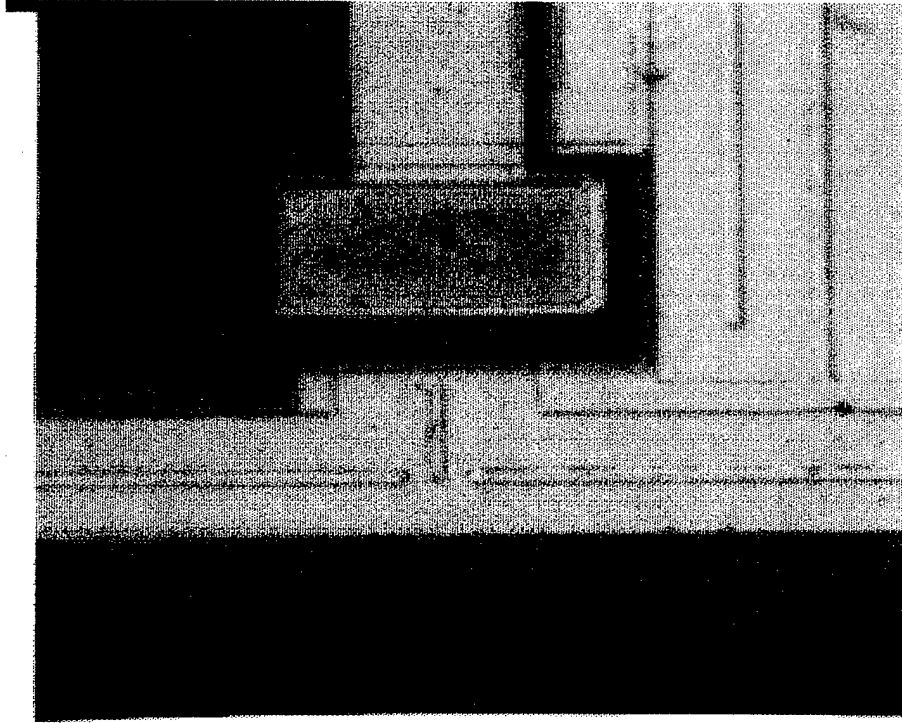


Figure 3.11. Photomicrograph details of the YBCO SQUID made on a bicrystal boundary and covered with gold. The YBCO SQUID reads the photoinduced changes in the currents flowing in the right and left sides of the QSKIP.

The device pictured in Figure 3.10 includes a YBCO photodetector with a YBCO readout SQUID (see detail in Fig. 3.11) located at the bottom. The photodetector is symmetric with each side configured into a serpentine pattern to increase the kinetic inductance. The YBCO SQUID and one side of the photodetector are shielded with a gold light shield. The YBCO SQUID readout consists of two Josephson junctions formed on a bicrystal boundary.

Packaged QSKIP were examined electrically and optically. In operation, the serpentine photodetector is biased by a DC current. The $0.1\mu\text{m}$ thick YBCO photodetector occupies a $100\mu\text{m} \times 100\mu\text{m}$ square. Each serpentine branch is about

700 μm long and 11 μm wide. For this geometry, the resistivity of undegraded YBCO lines should be about 300 $\mu\Omega\text{-cm}$ at 300K. The R vs T curve was taken at 10 μA bias current. At room temperature, the detector's resistance is about 8.125K Ω . This corresponds to a resistivity of about 2,553 $\mu\Omega\text{-cm}$ at 300K, compared to about 300 $\mu\Omega\text{-cm}$ at 300K for an as deposited and unprocessed YBCO film. The almost nine fold increase in the YBCO resistivity, at room temperature, represents process induced degradation which also effects the transition temperature.

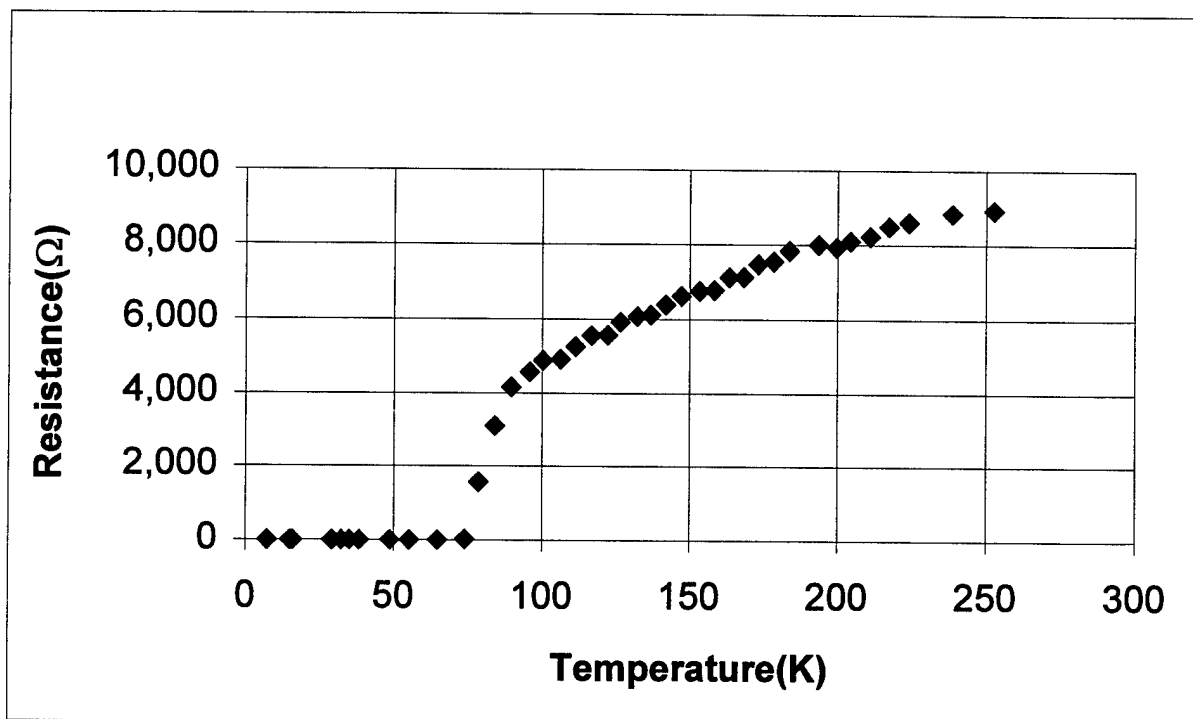


Figure 3.12. R vs T plot of YBCO in a multispectral QSKIP structure. The resistivity has increased almost nine fold over the resistivity of as deposited YBCO films.

The YBCO photodetector transition temperature is about 65K. Figure 3.12 shows a plot of the superconducting transition temperature of the YBCO detector. These process degradations also reduce the YBCO superconducting transition temperature from 89K to 65K. The processing damage to the YBCO films, we attribute primarily to the

silicon dioxide layer covering the YBCO. The sputtered silicon dioxide is used to provide electrical isolation between the gold interconnect lines and the YBCO film.

The first Multispectral QSKIP devices fabricated on this program had YBCO that was not superconducting down to 5K. It was determined that the sputtered silicon dioxide films were silicon rich. The excess silicon in silicon dioxide is expected to leach oxygen from the YBCO films. Experiments were run to add oxygen to the Argon sputtering gas used to deposit the silicon dioxide films. The addition of oxygen to argon is expected to make the sputtered silicon dioxide films more stoichiometric. With this process change, the deposited YBCO films remained superconducting after processing although they exhibited a reduced transition temperature.

To identify the cause of T_C reduction, we stripped the oxide from these YBCO films and attempted to reoxygenate these film. Thermal cycles in oxygen ambient at 400C did not increase the YBCO films transition temperature to 85K. The reduced transition temperature did not increase, leading us to conclude that some silicon has diffused into the YBCO sample to produce irreversible reductions in T_C . Careful tuning of the silicon dioxide deposition process improved the YBCO film quality. The latest YBCO films remained superconducting after all the processing.

However with a reduced transition temperature and an increased resistivity we expect a significant reduction in the quasiparticles lifetime. The absence of a photoresponse is attributed to a significant degradation in the quasiparticles lifetime. A solution to the YBCO degradation issue is to use epitaxial SrTiO_3 as the insulator and also as the YBCO passivation layer. Such a process is being developed in the laboratory.

The QSKIP YBCO readout SQUID is made on a 24° SrTiO_3 bicrystal substrate. The $I_{\text{C}}R_{\text{N}}$ SQUID product is $40\mu\text{V}$ at 4.5 K. The SQUID I-V curves were also measured at higher temperatures between 7.5K and 48.8K, see Figure 3.13. SQUID action is observed at the lower temperatures between 4.5K and 7.5K. The critical current of the SQUID at 7.5K was about $60\mu\text{A}$ and decreases to zero at 48.8K. These SQUID characteristics are not as good as for a niobium SQUID incorporated with a YBCO detector (see Figure 3.14).

The multispectral QSKIP was tested for photoresponse at 7.5K. No photoresponse was detected. The lack of a photoresponse is attributed to a reduced lifetime caused by processing the YBCO. The SQUID $I_{\text{C}}R_{\text{N}}$ product at 4.2K is also low, about $40\mu\text{V}$. Such a low value further increases the difficulty of seeing a small photoresponse signal since the photodetector output is directly proportional to the SQUID's $I_{\text{C}}R_{\text{N}}$ product. If one assumes an "s" wave superconductor, the SQUID's $I_{\text{C}}R_{\text{N}}$ product is limited to about $2\Delta \approx 3.5kT_{\text{C}} \approx 27\text{meV}$. This theoretical value is almost three orders of magnitude larger than the measured SQUID's $I_{\text{C}}R_{\text{N}}$ product of $40\mu\text{V}$. We attribute the lack of a photoresponse to a combination of a degraded YBCO superconducting transition temperature and a SQUID with a low $40\mu\text{V}$ $I_{\text{C}}R_{\text{N}}$ product.

In future programs, the processing will use SrTiO_3 insulators instead of SiO_2 to maintain good quality (or long lifetime) YBCO. Also, instead of using SQUIDs with grain boundary junctions, we will make use of shallow edge junctions made with PBCO. Such changes should go a long way to obtain multispectral QSKIP with a good photoresponse.

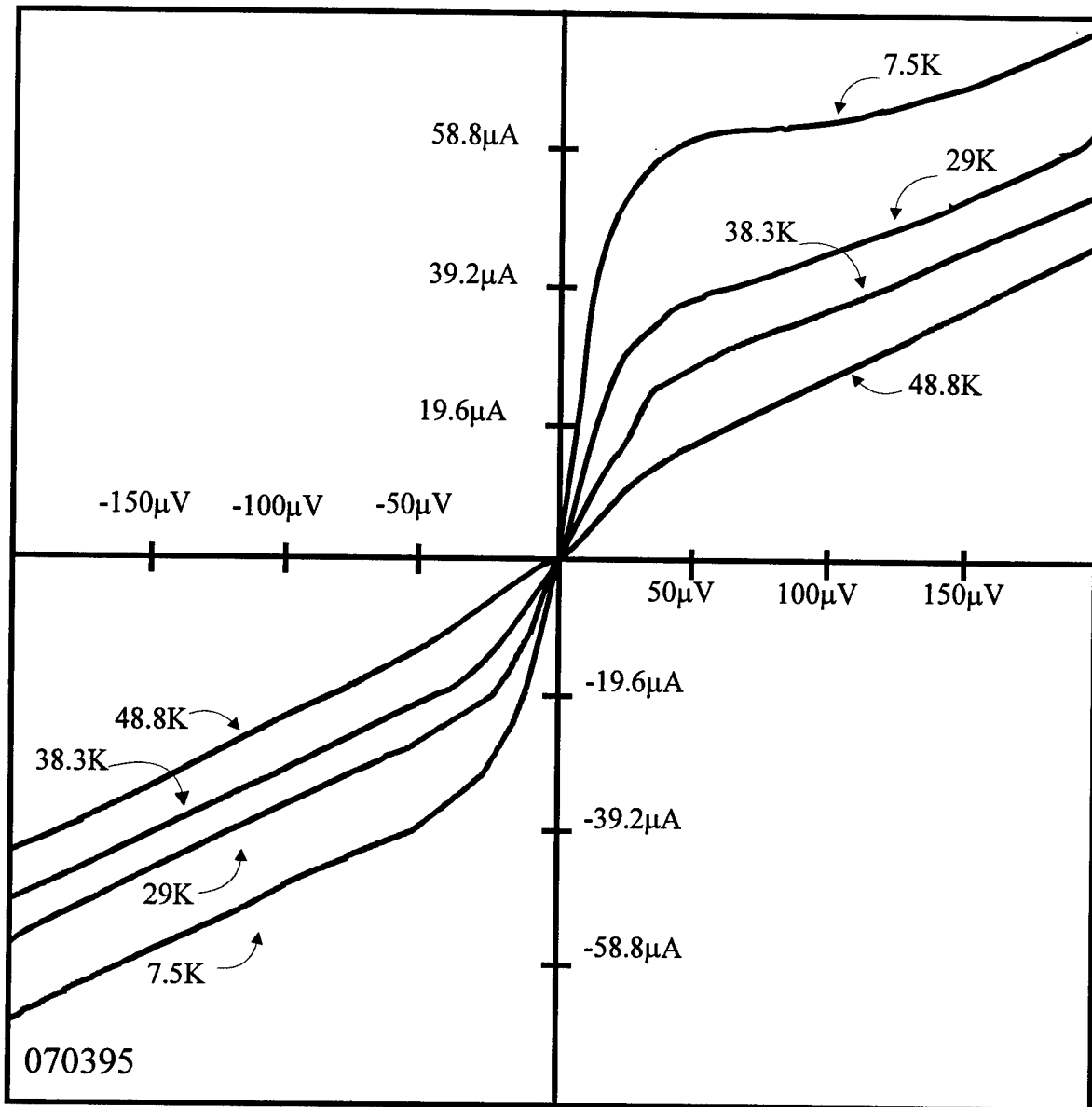


Figure 3.13 YBCO SQUID with grain boundary junctions made on a SrTiO₃ bicrystal. The SQUID I-V curves are shown as a function of operating temperature.

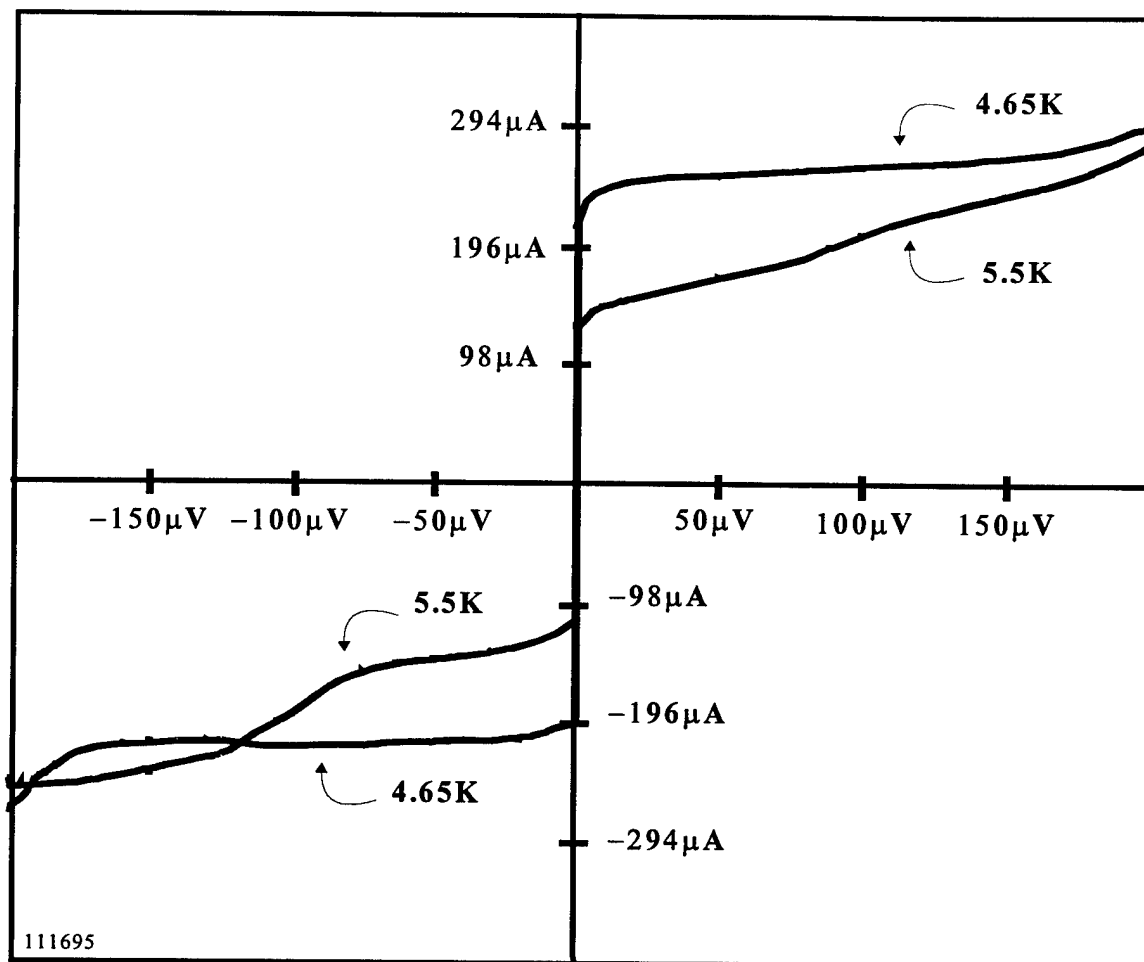


Figure 3.14 Characteristics of a niobium SQUID incorporated with a YBCO detector fabricated on a navy contract.

In conclusion, the calculation reveal that the Multispectral QSKIP device should provide excellent performance with an NEP of about 2.5×10^{-15} Watts/ $\sqrt{\text{Hz}}$ and between a 30-40 μm cut-off wavelength. On this program, we have developed performance models and photodetector structures which should provide the base for future demonstration of superconducting quantum photodetectors. With the development of improved fabrication, the QSKIP will be demonstrated. The main improvement for QSKIP design is a reduction of the magnetic field inductance relative to the kinetic inductance. Both process and design improvements are being pursued and we expect positive results in the near future.

4.0 PUBLISHED/SUBMITTED PAPERS.

4.1 Photoresponse Mechanism of Thin Superconducting Films and Superconducting Detectors.

Photoresponse mechanisms of thin superconducting films and superconducting detectors

A.V. Sergeev and M.Yu. Reizer

*Department of Physics, The Ohio State University,
Columbus, Ohio 43210*

ABSTRACT: The photoresponse of ordinary and high- T_c superconductors depends critically on the hierarchy of relaxation times, such as the electron-phonon and phonon-electron scattering times, the time of phonon escape from a superconducting film and also the phonon return time. For thin films of cuprates, close to the superconducting transition the following components of transient response are identified. The picosecond photoresponse is attributed to the dynamic of nonequilibrium quasiparticles and Cooper pairs. The nanosecond response is described by the thermal boundary resistance (the Kapitza resistance) between a superconducting film and a substrate. The microsecond response is associated with the phonon diffusion in the substrate. Using experimental results, we deduce characteristic time of electron-phonon relaxation and parameters of the film-substrate interface. The kinetic inductance photoresponse of superconductors with s- and d-wave pairing far below the superconducting transition is also calculated. We study parameters (responsivity, operating rate and noise equivalent power) of a nonequilibrium detector, in which only electron states are changed under the radiation, while the film phonons stay in thermodynamic equilibrium with the substrate. Our analysis demonstrates that the nonequilibrium superconducting detectors have essential advantages compared to superconducting bolometers and other detectors.

(PACS: 74.25.Nf, 74.76.Bz)

CONTENTS

1. Introduction
2. Electron and phonon relaxation times.
3. Photoresponse near the superconducting transition.
4. Kinetic inductance photoresponse of ordinary superconductors far below the superconducting transition.
5. Kinetic inductance response of d-wave superconductor at low temperature.
6. Noise characteristics.
7. Comparison.
8. Conclusions.

1. INTRODUCTION

The photoresponse of thin films of high- T_c superconductors has been attracting attention since the discovery of these materials. Much interest has sprung from numerous very promising applications such as fast detectors of the electromagnetic radiation, wide-band mixers and different switches. The electrical response to optical and microwave signals has been measured by many authors and interpreted either as the bolometric effect or the nonequilibrium response. In the bolometric effect the electromagnetic radiation results in simple heating of a superconducting films. In this case the electron and phonon subsystems of the film are described by the same temperature shift with respect to the substrate, which in turn is determined by the Kapitza resistance at the film-substrate interface or by the heat conductivity of the substrate. A crossover from one bolometric regime to another has been studied recently¹, and these investigations show a reasonable agreement between the parameters of the bolometric response and the phonon transparency of the interface, calculated on the base of the acoustic mismatch theory. Design and performance of modern superconducting bolometers have been discussed in a recent review².

This paper focuses mainly on the nonequilibrium response. There is a lot of experimental data, obtained near the superconducting transition, that demonstrate the nonbolometric response of high- T_c superconductors with a picosecond relaxation time^{3,4,5,6,7,8,9,10,11,12,13,14,15}. However, the nature of the nonequilibrium mode is still under debate. In Ref. 16 this mode is associated with the quantum photofluxonic process, in which a photon creates a vortex-antivortex pair. Another quantum effect was proposed in Ref. 17 (see also Ref. 18). A photon directly interacts with a magnetic vortex in a superconducting film, and if the photon energy is larger than the vortex activation energy, it produces additional flux creep and flux flow. However, the microscopic description of both mechanisms is still unclear. Following from the quantum photofluxonic effects, the the red boundary of the spectral characteristic

has not been observed.

We will assume that, in general, the nonequilibrium response, like the bolometric effect, results from suppression of superconductivity by excess quasiparticles, which are created by electromagnetic radiation^{19,20}. In the bolometric regime these excess quasiparticles have reached thermodynamic equilibrium with the film phonons, and both electron and phonon subsystems under the radiation are described by the same temperature shift. Unlike the bolometric effect, in the nonequilibrium response only electron states are changed by the radiation, while the phonon subsystem of the film remains in thermodynamic equilibrium with the substrate and plays the role of the heat sink for electrons. Therefore, in the nonequilibrium detectors the energy of the electromagnetic radiation changes only electron states without wasting power on heating the phonon subsystem. This characteristic feature of nonequilibrium response allows us to improve all parameters of the detector. Note that, in both bolometric and nonequilibrium effects, the correction to the electron (quasiparticle) distribution function due to the radiation gives rise to a change of a macroscopic parameter (such as the resistivity, the kinetic inductance or the magnetic flux), which in turn is measured by an external read-out circuit. In the bolometric effect the electron distribution function is completely controlled by the phonon subsystem, while in the nonequilibrium effect the distribution function is formed by the source of electromagnetic radiation and the electron relaxation mechanisms. In the latter case the nonequilibrium electron distribution function may depend on the radiation frequency, this is not always convenient for applications. However, we will show that in some cases of practical interest the nonequilibrium function may be described by the electron temperature, which differs from the phonon temperature and relaxes due to the electron-phonon interaction.

Basic parameters of the nonequilibrium detector are governed by the evolution of the electron distribution function under the effect of the radiation. The characteristic time of the detector is the inelastic electron relaxation time. The noise limit is determined by

fluctuations of the electron distribution function. The responsivity depends upon the net quantum efficiency (the number of low energy quasiparticles photogenerated by a photon), which in turn is determined by the electron-electron interaction and also by the interaction of electrons with high energy phonons. Parameters of the nonequilibrium detector may be regulated over a wide range by the choice of the material, the operating temperature, *etc.*

The purpose of present work is to study the necessary conditions for the realization of the nonequilibrium response and also to calculate the limiting characteristics of nonequilibrium detectors. In the next section we consider electron and phonon relaxation times. The hierarchy of characteristic relaxation times defines the steady-state nonequilibrium distribution functions of quasiparticles and phonons under the radiation as well as the quasiparticle and phonon transient response to a short laser pulse. The mechanism of steady state response is determined by the relation between the phonon relaxation times. At low temperatures the time of the phonon escape from a thin film to the substrate (τ_{es}) is shorter than the phonon-electron scattering time (τ_{ph-e}), and this condition provides the nonequilibrium steady-state response. The relation between τ_{es} and τ_{ph-e} is altered as the working temperature is raised from helium temperatures to the liquid-nitrogen range, and only the bolometric effect is observed in steady-state measurements at high temperatures. The form of electron transient response depends critically on the relation between the electron energy relaxation time due to the electron-phonon interaction (τ_{e-ph}) and the phonon-electron scattering time (τ_{ph-e}). At helium temperatures τ_{e-ph} is longer than τ_{ph-e} , and the photoresponse is characterized by a simple exponential decay. The characteristic time of the decay is τ_{e-ph} for the nonequilibrium response, which is realized, if $\tau_{es} \ll \tau_{ph-e}$. In the opposite case, $\tau_{es} \gg \tau_{ph-e}$, transient response is solely bolometric, and the corresponding decay time is τ_{es} . The relation between τ_{e-ph} and τ_{ph-e} is altered at $T=5-10K$. At high temperatures the transient response is very complex.

The qualitative picture of photoresponse in high- T_c cuprates is as follows. A short laser

pulse heats only electrons in the film. The electron-electron interaction and interaction of electrons with high-frequency phonons lead to the fast avalanche multiplication of nonequilibrium quasiparticles. Using optical pump and probe techniques, the characteristic time of this process was found to be approximately 0.1 ps. An increase of population of low-energy quasiparticle leads to the suppression of superconductivity. Voltage shift in the resistive state is proportional to the concentration of low-energy excess quasiparticles, the kinetic inductance signal in the superconducting state is proportional the time derivative of the quasiparticle population. The fast relaxation with the picosecond decay time corresponds to the cooling of the quasiparticle subsystem due to the electron-phonon interaction. Then electrons and film phonons reach equilibrium and are described by the same temperature. The next nanosecond decay corresponds to the cooling of the electrons and film phonons due to phonon escape from the film to the substrate. In other words, the second decay is determined by the Kapitza resistance at the film-substrate interface. At the time scale longer than the time of phonon return to the film, the temperature shift at the interface becomes unessential, and the film cooling is governed by the phonon diffusion in the substrate. Therefore, the third decay has power-law temporal dependence. Analyzing experimental data of the picosecond nonequilibrium response we conclude that the interaction of electrons and thermal phonons in high- T_c superconductors is stronger than the interaction in ordinary superconductors. On one hand, the strong electron-phonon interaction makes it possible to get very fast (as short as 1ps) radiation detectors. On the other hand, due to this interaction the electron and phonon subsystems of the film reach an equilibrium during a short time interval, and even in ultrathin films of high- T_c superconductors we cannot satisfy the condition: $\tau_{es} \ll \tau_{ph-e}$, and the steady-state under the radiation corresponds to the bolometric effect.

Many possible applications are limited by the presence of the bolometric component (bolometric tails) in the transient photoresponse of high- T_c materials. The bolometric com-

ponent significantly increases the conversion loss of mixers^{21,22}, it also impairs the performance of fast switches. The reduction of bolometric component is the main question for development of superconducting electronics on the basis of nonequilibrium effects. One solution may be decreasing the operating temperature to reach the conditions, at which the phonon escape from the film dominates over the phonon-electron relaxation. In addition, the small electron heat capacity in the superconducting state at low temperatures provides a way to improve noise characteristics of detectors. Possible realizations of the sensitive read-out circuit for the nonequilibrium kinetic inductance detector were suggested in Ref. 23 and Ref. 24. The kinetic inductor forms one branch of the DC SQUID loop, in which the inductance change under the radiation is converted to a voltage signal. Note that this signal as well as a signal of a resistive detector is proportional to a change of the quasiparticle population. Therefore we consider kinetic inductance detectors in the same way as resistive detectors.

The paper is organized as follows. In the second section we will give a review of the electron and phonon relaxation times and the corresponding mean free paths in the normal and superconducting states of a thin metallic film. The next section is devoted to the photoreponse of ordinary and high- T_c superconductors near the superconducting transition. In Sec. 4 and 5 we consider the nonequilibrium kinetic inductance response in the superconducting state far below the transition. In Sec. 4 we calculate the kinetic inductance response of ordinary superconductors in the context of the BCS model. In Sec. 5 we study the response of high- T_c superconductors using the d-wave pairing model, which has been supported for these materials by recent experiments. In Sec. 6 we consider fluctuations of the electron distribution function to calculate the limiting noise characteristics of the superconducting nonequilibrium detectors. Finally we compare the basic characteristics of the nonequilibrium detectors and superconducting bolometers.

2. ELECTRON AND PHONON RELAXATION TIMES

The nonequilibrium electron (quasiparticle) and phonon distribution functions under the radiation are found from kinetic equations. The electromagnetic field appears in the kinetic equation for quasiparticles as a source of excess quasiparticles. Processes of relaxation are described by corresponding collision integrals. The collision integrals have complicated forms, and we restrict ourselves to the relaxation times of electrons and phonons.

We begin our discussion with the electron-phonon interaction in the normal state above the superconducting transition. Strong electron-impurity or electron-boundary scattering in thin films modifies the electron-phonon interaction, which is dependent on the electron mean free path, l . Following Ref. 25 and Ref. 26, we present the energy relaxation rate of electrons interacting with longitudinal phonons as

$$\frac{1}{\tau_{e-l.ph}^n(\epsilon = 0)} = \frac{7\pi\zeta(3)}{2} \frac{\beta T^3}{(p_F u_l)^2} F_l(q_T l), \quad (2.1)$$

where u_l is the sound velocity, p_F and v_F are the Fermi momentum and velocity, and $q_T = T/u_l$ is the wavevector of the thermal phonon (we assume the Debye phonon spectrum). Note that, we measure the electron energy, ϵ , with respect to the electron chemical potential. In Eq. 2.1, β is the kinetic constant of the electron-phonon interaction,

$$\beta = \left(\frac{2}{3}\epsilon_F\right)^2 \frac{\nu(0)}{2\rho u_l^2}, \quad (2.2)$$

where $\nu(0) = mp_F/\pi^2$ is the electron two spin density of states and ρ is the density of the material. This constant describes coupling of electrons with thermal phonons. In the frame of the simplest "jelly" model the kinetic constant may be expressed in terms of the electron-phonon renormalization constant²⁷ λ , as $\beta = \lambda(2p_F/q_D)^2$, where q_D is the Debye wavevector.

In the general case, the function $F_l(z)$ is presented through the Pippard function $\Phi_l(x)$

as follows

$$F_l(z) = \frac{2}{7\zeta(3)} \int_0^\infty dx \Phi_l(xz) (N(x) + f(x)) x^2, \quad (2.3)$$

where $N(x)$ and $f(x)$ are the Bose and Fermi functions, and

$$\Phi_l(x) = \frac{2}{\pi} \left(\frac{x \operatorname{artan}(x)}{x - \operatorname{artan}(x)} - \frac{3}{x} \right). \quad (2.4)$$

In the limiting cases the function $F_l(q_T l)$ is

$$F_l(q_T l) = \begin{cases} 1, & \text{if } l > T/u_l, \\ \frac{2\pi^3}{35\zeta(3)}(q_T l), & \text{if } l < T/u_l. \end{cases} \quad (2.5)$$

In pure metals and superconductors the interaction of electrons with transverse phonons is absent. Electron scattering from vibrating impurities or from a film boundary gives rise to energy relaxation, and the corresponding rate is

$$\frac{1}{\tau_{e-t.ph}^n(0)} = \frac{3\pi^4 \beta_t T^2}{2(p_F u_t)(p_F l)} F_t(q l), \quad (2.6)$$

where

$$F_t(z) = \frac{4}{\pi^2} \int_0^\infty dx \Phi_t(xz) (N(x) + f(x)) x, \quad (2.7)$$

and

$$\Phi_t(x) = \frac{2x^3 + 3x - 3(x^2 + 1)\operatorname{artan}(x)}{2x^3}. \quad (2.8)$$

In the limiting cases the function $F_t(q_T l)$ is

$$F_t(q_T l) = \begin{cases} 1, & \text{if } l > T/u_t, \\ \frac{\pi^2}{5}(q_T l)^2 & \text{if } l < T/u_t. \end{cases} \quad (2.9)$$

In Eq. 2.6, β_t is the coupling constant of electrons with transverse phonons. In the jelly model, assuming the isotropic Fermi surface and the Boom-Staver relation for the sound velocity, the coupling constants satisfy the equation: $\beta_t/\beta_l = (u_l/u_t)^2$.

We denote the total electron relaxation rate due to the interaction with longitudinal and transverse phonons as

$$\frac{1}{\tau_{e-ph}^n(0)} = \frac{1}{\tau_{e-l.ph}^n(0)} + \frac{1}{\tau_{e-t.ph}^n(0)}. \quad (2.10)$$

According to Eqs. 2.1-2.9 in the impure case ($l < u_l, u_t$), the electron-phonon scattering rate is

$$\frac{1}{\tau_{e-ph}^n(0)} = \frac{\pi^4 \beta T^4}{5} (p_F l) \left(\frac{\beta}{(p_F u_l)^3} + \frac{3\beta_t}{2(p_F u_t)^3} \right), \quad (2.11)$$

Bearing in mind that the parameter u_l/u_t changes in the interval 1.8-2.5 for the most materials, we come to the conclusion that the interaction of electrons with transverse phonons dominates over the interaction with longitudinal phonons in the impure limit and in the wide transition region, which spreads up to 50K in samples with a short electron mean free path ($l < 10 - 20\text{\AA}$) or in thin films.

Now we consider the electron-electron interaction. In a pure normal metal the energy relaxation rate of electrons at the Fermi surface due to the electron-electron interactions is²⁸

$$\frac{1}{\tau_{e-e}^n(0)} = \frac{\pi^4}{64} \frac{k}{p_F} \frac{T^2}{\epsilon_F}, \quad (2.12)$$

where $k^2 = 4\pi e^2 \nu(0)$.

In a thin film of an impure metal the electron-electron interaction is enhanced considerably²⁹, and the energy relaxation rate is

$$\frac{1}{\tau_{e-e}^n(0)} = \frac{e^2 R_0 T}{2\pi} \ln \frac{\pi}{e^2 R_0}, \quad (2.13)$$

where $R_0 = 1/\sigma_n d$ is the resistance of a film square.

In the superconducting state near the transition temperature T_c the quasiparticle recombination and relaxation rates are of the same order as the relaxation rate in the normal state (Eqs. 2.1 - 2.11). According to Ref. 30, at low temperatures ($T \ll \Delta$) the quasiparticle scattering rate due to the electron-phonon interaction in a pure superconductor is

$$\frac{1}{\tau_{e-ph}^s(\epsilon = \Delta)} = \Gamma\left(\frac{7}{2}\right) \zeta\left(\frac{7}{2}\right) \frac{\pi \beta_l T^3}{4(p_F u)^2} \left(\frac{2T}{\Delta}\right)^{1/2}. \quad (2.14)$$

The quasiparticle recombination rate is

$$\frac{1}{\tau_{e-ph}^r(\epsilon = \Delta)} = 2\pi \beta_l \left(\frac{\Delta}{p_F u}\right)^2 (2\pi \Delta T)^{1/2} \exp\left(-\frac{\Delta}{T}\right). \quad (2.15)$$

The quasiparticle scattering rate decreases in an superconductor with a small electron mean free path ($lT < u_l, u_t$), and according to Ref. 26 the scattering rate may be found as

$$\frac{1}{\tau_{e-ph}^s(\epsilon = \Delta)} = \frac{2}{5} \Gamma\left(\frac{9}{2}\right) \zeta\left(\frac{9}{2}\right) \left(\frac{\beta}{(p_F u_l)^3} + \frac{3\beta_t}{2(p_F u_t)^3} \right) (p_F l) T^4 \left(\frac{2T}{\Delta} \right)^{1/2}. \quad (2.16)$$

Under the condition $l\Delta < u_l, u_t$, the recombination of quasiparticles with emitting a phonon is also modified by the electron-impurity scattering. In this case, the recombination rate is

$$\frac{1}{\tau_{e-ph}^r(\epsilon = \Delta)} = \frac{2}{5} \left(\frac{\beta}{(p_F u_l)^3} + \frac{3\beta_t}{2(p_F u_t)^3} \right) (p_F l) \Delta^3 (2\pi \Delta T)^{1/2} \exp\left(-\frac{\Delta}{T}\right). \quad (2.17)$$

The exponential temperature dependence in Eqs. 2.15 and 2.17 corresponds to the exponentially small equilibrium quasiparticle concentration n_{eqv} at low temperatures,

$$n_{eqv} = \left(\frac{\pi T \Delta}{2} \right)^{1/2} \nu(0) \exp\left(-\frac{\Delta}{T}\right). \quad (2.18)$$

For further discussion it is convenient to introduce the dimensionless quasiparticle concentration $x = n_{eqv}/(2\nu(0)\Delta)$. Thus, Eqs. 2.15 and 2.17 show that the contribution of recombination processes due to the electron-phonon interaction is of the order of x/τ_{e-ph}^n .

Now we discuss the electron-electron interaction in a superconductor. The rate of scattering processes, which conserve total number of quasiparticles, and the rate of recombination processes are given by³¹

$$\frac{1}{\tau_{e-e}^s(\Delta)} = \frac{1}{\tau_{e-e}^n(0)} \left(\frac{\Delta}{2\pi T} \right)^{1/2} \exp\left(-\frac{\Delta}{T}\right), \quad (2.19)$$

$$\frac{1}{\tau_{e-e}^r(\Delta)} = \frac{1}{\tau_{e-e}^n(0)} \frac{\Delta}{\pi T} \exp\left(-\frac{2\Delta}{T}\right). \quad (2.20)$$

Thus, at low temperatures the relative effectiveness of the electron-electron interactions is small compared with the electron-phonon interaction, because it requires an additional power of x .

There are no reliable calculations of the electron-electron relaxation rates in an impure superconductor.

There is one more relaxation processes specific for the superconducting state - relaxation of the order parameter. For all temperatures, except for a very narrow region near T_c , the superconducting order parameter monitors Φ s simultaneously the change of the electron distribution function. As found in Ref. 32, very close to T_c , $0.97T_c < T < T_c$, the relaxation of the order parameter to the value corresponding to the instant electron distribution function is slower than the energy relaxation. In this temperature interval the relaxation time of the order parameter is

$$\tau_\Delta = \frac{\pi^3}{7\zeta(3)} \frac{T}{\Delta} \min\{\tau_{e-ph}, \tau_{e-e}\}. \quad (2.21)$$

Now let us discuss the phonon relaxation. The phonon-electron and electron-phonon scattering times in a normal metal are connected to each other by the energy balance equation

$$\frac{1}{\tau_{ph-e}^n} \approx \frac{C_e}{C_{ph}} \frac{1}{\tau_{e-ph}^n}, \quad (2.22)$$

where C_e and C_{ph} are the electron and phonon specific heat capacities in the normal state. Note that $C_e \gg C_{ph}$ at low temperatures, and for most of metals the heat capacities of electrons and phonons become equal at $T = 5 - 10K$.

In the superconducting state at low temperatures ($T \ll \Delta$) the energy dependence of the phonon relaxation rate is very important. The main relaxation mechanism of high frequency phonons with energies $\omega_q > 2\Delta$ is creation of quasiparticles from the condensate and the corresponding relaxation rate, $(\tau_{ph-e}^{s,>})^{-1}$, is practically the same as in the normal state. The main relaxation mechanism of low energy phonons is absorption of phonons by quasiparticles; therefore, the corresponding rate is proportional to the quasiparticle concentration,

$$\frac{1}{\tau_{ph-e}^{s,<}} \approx \frac{x}{\tau_{ph-e}^n}, \quad (2.23)$$

The relaxation of acoustic phonons due to the phonon-phonon interaction (the lattice anharmonicity) is determined by the equation

$$\frac{1}{\tau_{ph-ph}} \approx \frac{(\max\{\omega, T\})^5}{(Mu^2)(p_F u)^3}. \quad (2.24)$$

The characteristic time of phonon escape from a film to a substrate is

$$\tau_{es} = \frac{4d}{K_{f-s}u}, \quad (2.25)$$

where K_{f-s} is the average phonon transparency of the film-substrate interface for phonons incident on the interface from the film.

If a width of a superconducting strip is larger than l_{ph}^s/K_{s-f} (l_{ph}^s is the phonon mean free path in a substrate and K_{s-f} is the average transparency for phonons incident on the interface from the substrate), the phonon return from the substrate to the film is important. According to Refs. 1 and 33, the characteristic rate of this process is

$$\tau_R = \frac{1}{\tau_{ph,s}(K_{s-f})^2}, \quad (2.26)$$

where $\tau_{ph,s}$ is the phonon scattering time in the substrate.

The balance of heat flows through the interface results in the following relation for average transparency coefficients¹:

$$K_{f-s}uC_{ph}^f = K_{s-f}u_sC_{ph}^s, \quad (2.27)$$

where u and u_s are the sound velocities in the film and in the substrate, C_{ph}^f and C_{ph}^s are the phonon specific heats of the film and the substrate.

As we discuss in the next section the relation between phonon relaxation times and the phonon escape time plays a decisive role in the mechanism of the photoresponse of a superconductor.

3. PHOTORESPONSE NEAR THE SUPERCONDUCTING TRANSITION

In this section we discuss the bolometric and nonequilibrium photoresponses near the

superconducting transition. Then we will show that these two mechanisms may explain practically all available experimental data obtained in ordinary and high- T_c superconductors.

3.1 Bolometric response.

The bolometric response at the superconducting transition is the most studied phenomenon. It is assumed that relaxation times of the electron and phonon subsystems are much smaller than the time of the bolometric response, which will be discussed latter. Therefore, the absorbed energy is effectively redistributed over the electron and phonon subsystems during a short time scale. After that the electron and phonon distribution functions are described by the same temperature. The phonon escape from a film to a substrate provides the film temperature relaxation, which is hindered by the backflow of hot phonons from a substrate to a film. In steady state measurements the backflow of nonequilibrium phonons may be limited by the film geometry. In the case of a structure of several strips, which is commonly used, the phonon return is negligible, provided the total width of the structure, W , is less than the critical value, W_c , *e.g.*

$$W \ll W_c = \frac{l_{ph,s}}{K_{s-f}}. \quad (3.1)$$

In Eq. 3.1, $l_{ph,s}$ is the phonon mean free path in the substrate. In transient-response measurements, the phonon backflow is unessential for the time scale shorter than the phonon return time τ_R (Eq. 2.14). Without the phonon backflow the cooling rate of the strips is determined by the phonon transparency of the interface, *i.e.* the Kapitza thermal resistance. In this case the time evolution of the film temperature, T , is described by the following equation

$$(C_e + C_{ph}) \frac{dT}{dt} = \frac{C_{ph}}{\tau_{es}} (T - T_0) + I_0. \quad (3.2)$$

Here T_0 is the temperature of the substrate and I_0 is the electromagnetic power absorbed per unit volume of the superconducting film.

As it follows from Eq. 3.2, the decay time of the bolometric response is

$$\tau_b = \frac{C_e + C_{ph}}{C_{ph}} \tau_{es}, \quad (3.3)$$

where the phonon escape time τ_{es} is determined by Eq. 2.13.

Without specifying the read-out circuits, it is convenient to define the responsivities of the resistive and kinetic inductance detectors as

$$r_R = \frac{\delta R}{RI_0 V}, \quad r_L = \frac{\delta L_k}{L_k I_0 V}, \quad (3.4)$$

where δR and δL_k are changes of the resistivity and the kinetic inductance due to the absorbed electromagnetic power $I_0 V$, where V is the volume of the sensitive element. The responsivities are expressed through the temperature derivatives of the resistance and the kinetic inductance

$$r_R = \frac{dR}{dT} \frac{\tau_{es}}{RC_{ph}}, \quad r_L = \frac{dL_k}{dT} \frac{\tau_{es}}{LC_{ph}}. \quad (3.5)$$

Note that the condition (3.1) is usually fulfilled at helium temperatures, *i.e.* for bolometers made from traditional superconductors. Such detectors have therefore the characteristic time τ_b (Eq. 3.3), defined by the phonon transparency of the interface. As for high- T_c superconductors, it is more difficult to satisfy Eq. 3.1 at nitrogen temperatures. Phonon transparencies of the interface between the YBaCuO-film and various substrates at nitrogen temperatures were determined in Ref. 1. These data and also the magnitudes of the critical width are presented in Tab. 1. As seen, the critical width W_c is of the order of $10\mu m$, while the total width of the strip structure was generally larger, or at least comparable with this scale. Therefore, in photoresponse measurements with low chopping frequencies of the electromagnetic radiation, the cooling of a film is controlled by the heat conductivity (phonon diffusion) of the substrate. We guess that this is the main reason why numerous experiments demonstrated current and temperature dependencies which are inconsistent with Eqs. 3.2-3.5. We will not consider such a regime, because it is not promising for detectors.

The bolometric regime controlled by the thermal resistance at the interface (the fast bolometric response) was observed in experiments with short laser pulses^{34,35,36,37,38,39}. It dominates during the time interval $t < \tau_R$ (Eq. 2.26) after a pulse. Fast bolometric response is characterized by exponential decay with the decay time defined by the phonon escape time (Eq. 2.13). For the time scale $t > \tau_R$ the slow nonexponential decay is determined by phonon diffusion in the substrate. In Sec. 3.3 we will discuss experimental data concerned with the fast bolometric response together with picosecond measurements of the nonequilibrium response.

3.2 Nonequilibrium photoresponse.

As well as in the proceeding subsection, we consider here the resistive response at the superconducting transition and the kinetic inductance response slightly below the transition. We begin discussion of the nonequilibrium photoresponse with the assumption that the electron and phonon distributions functions due to the radiation may be described by the Fermi and Planck functions with nonequilibrium temperatures, θ and T_{ph} . Later we will justify this assumption for many situations. Time evolution of the nonequilibrium temperatures θ and T_{ph} under the modulated radiation is given by equations

$$C_e \frac{d\theta}{dt} = -\frac{C_e}{\tau_{e-ph}}(\theta - T_{ph}) + \frac{I_0}{d}, \quad (3.6)$$

$$C_{ph} \frac{dT_{ph}}{dt} = \frac{C_{ph}}{\tau_{ph-e}}(\theta - T_{ph}) - \frac{C_{ph}}{\tau_{es}}(T_{ph} - T_0), \quad (3.7)$$

where T_0 is the temperature of the substrate. The electron relaxation time τ_{e-ph} in Eq. 3.6 may be presented as $\tau_{e-ph} = ab \tau_{e-ph}^n(0)$, where a is a function of T/T_c ($a(T_c) = 1$), b takes into account averaging over the electron energy, and $\tau_{e-ph}^n(0)$ is the electron-phonon relaxation time in the normal state (Eqs. 2.1-2.11) at the Fermi surface. Near the transition, superconducting corrections to the relaxation time from the coherent factors and the electron density of states are small, and even at $T = 0.8T_c$ a change of the parameter a is smaller than 15% (see Fig.2 of Ref. 30). The parameter b is determined by the frequency dependence of

the Eliashberg function (the phonon density of states weighted by the square of the matrix element of the electron-phonon interaction): $F(\omega) \propto \omega^n$. Our calculations show that b is 0.62 for $n=1$, 0.22 for $n=2$ and 0.11 for $n=3$. The average phonon relaxation time τ_{ph-e} in Eq. 3.7 may be exactly calculated from the energy-balance equation: $\tau_{ph-e} = \tau_{e-ph} C_{ph}/C_e$.

Whatever the origin of the nonhomogenous resistive state in a superconducting film is, the resistivity change under radiation may be presented as $\delta R = (\partial R(T)/\partial T)\delta\theta$, where $(\partial R(T)/\partial T)$ is measured independently. For BCS superconductors the kinetic inductance change in the superconducting state near the transition is

$$\frac{\delta L_k}{L_k} = \frac{1}{\Delta} \frac{\partial \Delta(T)}{\partial T} \delta\theta. \quad (3.8)$$

As it follows from Eqs. 3.6 and 3.7, the form of the photoresponse depends strongly on the relation between the electron and phonon specific heat. In the limit $C_e > C_{ph}$, which usually corresponds to the temperature interval $T < 5 - 10K$, the transient response of the electron temperature to the short laser pulse with duration τ_d is given by

$$\theta(t) = \frac{I_0 \tau_d}{C_e} \exp\left(-\frac{t}{\tau_{e-ph} + (C_e/C_{ph})\tau_{es}}\right) \quad (3.9)$$

Therefore, in thin films, where the phonon escape to a substrate is faster than the phonon-electron relaxation,

$$\tau_{es} \ll \frac{C_{ph}}{C_e} \tau_{e-ph} \sim \tau_{ph-e}, \quad (3.10)$$

the nonequilibrium electron temperature relaxes exponentially to the substrate temperature, T_0 , with the characteristic time τ_{e-ph} . The condition (3.10) may be interpreted as follows. Nonequilibrium phonons, emitted by electrons, escape from the film without scattering on electrons. Therefore, the phonons that interact with the electron subsystem have an equilibrium substrate temperature. The condition opposite to 3.10 corresponds to the bolometric response.

At higher temperatures $T > 5 - 10K$, where the electron heat capacity is smaller than phonon one, $C_e < C_{ph}$, the photoresponse is more complicated. Only under condition of 3.10 we get a simple exponential decay with characteristic time τ_{e-ph} . In the opposite limit, namely $\tau_{es} \gg \tau_{ph-e}$, Eqs. 3.6 and 3.7 predict a biexponential decay

$$\theta(t) = \frac{I_0 \tau_d}{C_e} \exp\left(-\frac{t}{\tau_{e-ph}}\right), \quad t < \tau_{ph-e}; \quad (3.11)$$

$$\theta(t) = \frac{I_0 \tau_d}{C_{ph}} \exp\left(-\frac{t}{\tau_{esc}}\right) \quad t > \tau_{ph-e}. \quad (3.12)$$

In accordance with Eq. 3.11, the film phonons, due to their large heat capacity, play the role of the heat sink for electrons at the first step of energy relaxation, until the electrons cool down to the phonon temperature. The next step (Eq. 3.12) corresponds to the bolometric effect, when both electrons and phonons cool down to the equilibrium substrate temperature

In Eqs. 3.6 and 3.7 we described the nonequilibrium electron distribution function by nonequilibrium temperature. This assumption is valid, if the absorbed energy effectively redistributes over the all electron subsystem faster than it transfers from electrons to phonons, in other words, if the electron-electron relaxation time is shorter than the electron-phonon one, $\tau_{e-e} \ll \tau_{e-ph}$. Note that for ordinary pure superconductors at helium temperatures, the electron-phonon scattering is the fastest energy relaxation process, and a description in terms of the nonequilibrium temperature is not adequate for real kinetic processes. In particular, at low radiation frequencies, $\Omega < 2\Delta$, the radiation cannot create new quasiparticles from condensate; it only shifts available quasiparticles to higher energies. This redistribution of quasiparticles results in the enhancement of superconductivity. In the opposite case, $\Omega > 2\Delta$, the superconductivity is effectively suppressed by new quasiparticles created from the condensate. The situation changes in a thin film of a superconductor with a small electron mean free path, where the electron-electron interaction dominates over the electron phonon scattering (see Eqs. 2.3 and 2.4). In this case the effect of radiation is reduced to frequency independent electron heating (increase of the electron temperature). Transition

from microwave enhancement of superconductivity to its suppression with the decrease of the electron mean free path was studied experimentally and theoretically in Ref. 40.

A problem of the inelastic electron scattering in high- T_c superconductors has been discussed in a recent review⁴¹. Most of the data shows the evidence of a strong interelectron interaction, which mechanism is still unclear. The corresponding scattering time is of the order of $0.01 - 0.1ps$, while, as we will see later, the electron-phonon relaxation time is of the order of $\sim 1ps$. Therefore, the concept of the nonequilibrium electron temperature is also justified for high- T_c materials.

3.3 Analysis of experimental data

We will now discuss experimental results for ordinary impure superconductors at helium temperatures. There are a lot of papers devoted to the electron heating in thin metallic films^{42,43,44}. The data obtained, together with results of other experiments in thin metallic films and semiconductor heterolayers, demonstrate the T^2 temperature dependence of the relaxation rate,^{45,46,47} which origin is still unclear⁴⁸. The measured photoresponse in the resistive state of thin impure superconducting films is well described by the electron heating model. The electron-phonon relaxation time extracted from the photoresponse data is in good agreement with results of experiments above T_c and demonstrates the same T^2 -dependence⁴⁹. Experimental results for Nb films from Refs. 49, 50 and 51 are summarized in Tab. 2. In Ref. 49 the superconducting transition was shifted to low temperatures by a magnetic field, and at 1.6 and 4.2K only the simple exponential decay is measured. The dependence of the decay time on the film thickness was found to be in agreement with Eq. 3.9: the decay time is independent on a thickness in ultrathin films, and it becomes proportional to a thickness with further increase of the film thickness. The critical thickness, shown in Tab. 2, was determined from Eq. 3.10, $\tau_{es}(d_c) = \tau_{ph-e}(T)$, which describe a transition from the nonequilibrium to the bolometric effect. If $d < d_c$, the decay time is the electron-phonon energy relaxation time, and, as we discussed above, it shows T^2 -

dependence. In the very narrow temperature range $0.97T_c < T < T_c$ the measured decay time varies as $(1 - (T/T_c))^{-1/2}$ in accordance with slow relaxation of the order parameter (Eq. 2.21). If $d > d_c$, the decay time is the time of the phonon escape (Eq. 2.25), which is independent on temperature. The critical thickness decreases with temperature, and at $T=8K$ it obviously becomes shorter than the film thickness of 20nm. If at these temperatures the electron heat capacity was still larger than the phonon one, $C_e(T) > C_{ph}(T)$, only the bolometric decay would have been observed in 20nm-films. Therefore, we deduce that the measured biexponential (nonequilibrium and bolometric) decay is inconsistent with the condition: $C_e(T) > C_{ph}(T)$. To explain these results we must invoke the high-temperature condition $C_e(T) < C_{ph}(T)$. Then, according to Eq. 3.11, the characteristic time of the first decay τ_1 is the electron-phonon relaxation time. The observed second decay is bolometric. In Refs. 50 and 51 the film width was $\sim 1mm$, which is larger than the critical width (Eq. 3.1), and therefore the film cooling was determined by the phonon diffusion in a substrate. The accuracy of measurements was not enough to distinguish between the exponential and power law temporal dependencies of the bolometric decay. Note also, that the electron-electron scattering time^{52,53}, obtained from the magnetoconductivity data, was found to be in a good agreement with Eq. 2.13. As it is seen from Tab. 2, in all temperature range the electron-electron scattering rate is shorter than the electron-phonon one. Therefore the use of the nonequilibrium electron temperature is justified for the analysis of photoresponse in Nb.

A summary of experimental response times in YBaCuO films is presented in Tab. 3. First measurements have already demonstrated a fast bolometric response³⁴ as well as picosecond nonequilibrium response⁵⁴. Note that films with a wide temperature transition were used in Ref.54, and a strong magnetic field was applied to reach the resistive state at helium temperatures. The value of the electron-phonon scattering time 100ps at 1.6K shows very strong interaction between electrons and thermal phonons. It was found latter that the

nanosecond response time is proportional to the film thickness³⁵ and is therefore caused by the thermal boundary resistance. The biexponential photoresponse decay was observed for the first time in Ref. 5. As seen from Tab. 3, up to now many works have shown the coexistence of the bolometric and nonequilibrium components in the photoresponse of high- T_c superconductors at liquid nitrogen temperatures. The kinetic inductance response in the superconducting state has been found in Ref. 4.

Finally, we discuss the relaxation times in $YBaCuO$ at nitrogen temperatures. In Ref. 3 the relaxation time at 77K was calculated from the experimental value of the temperature shift under influence of the radiation (Eq. 3.11), and it was found that $\tau_{e-ph} \simeq 2ps$. In recent papers^{13,15} $\tau_{ph-e} = 40ps$ was determined as the transition from the nonequilibrium to the bolometric component in the transient response (see Eqs. 3.11 and 3.12). According to Eq. 2.22, the corresponding electron-phonon relaxation time is $\tau_{e-ph} = 1.8ps$ in agreement with Ref. 3. In Ref. 55 the measuring photoresponse was simulated by the two nonequilibrium temperature model (Eqs. 3.6 and 3.7), and at the superconducting transition the electron-phonon relaxation time was obtained to be 3.5ps and 1.8ps for $YBaCuO$ and $TlBaCuO$ films respectively.

Unfortunately, a measurement of the picosecond decay is limited by the resolution of experimental equipment, and up to now there are no direct measurements of τ_{e-ph} near the superconducting transition. Therefore, values of τ_1 in Tab. 3 give us the upper limit of the electron-phonon relaxation time.

As seen from our analysis, most of experimental results may be understood by the two nonequilibrium temperature model. Taking into account data of Ref.9, we think that this model has some limitations for ultrathin films (or temporal scale $\sim 10 - 100$ ps). Films with a thickness 15-40nm were used in Ref. 9 for photoresponse measurements, and 40-100ps decay time was found. The most surprising peculiarity of these data is that the decay time is proportional to the film thickness, while phonon escape (the bolometric effect) relaxation

times are at least six time longer than it was observed. To explain these results we suggested a new mechanism of energy transfer from film electrons to substrate phonons by means of inelastic electron-boundary scattering⁵⁶ (the electron Kapitza conductivity), which will be described in detail elsewhere. We guess that suggested mechanism may be also important for understanding a response with 15 ps decay time, which was observed recently in Ref. 57.

4. KINETIC INDUCTANCE PHOTORESPONSE OF S-WAVE SUPERCONDUCTORS FAR BELOW THE SUPERCONDUCTING TRANSITION

At low temperatures ($T \ll \Delta$) the nonequilibrium response dominates if the mean free path of a thermal phonon, $l_{ph}^<$ is much larger than the effective film thickness,

$$l_{ph}^< \approx l_{ph}(T)/\bar{x} \gg d/K. \quad (4.1)$$

In this case the distribution function of low energy phonons ($\omega \sim T \ll \Delta$) in the film is described by the equilibrium function with the substrate temperature T_0 , and the substrate plays a role of the heat sink. The condition (4.1) may be easily satisfied for films with thickness $d \sim 100nm$, because the dimensionless quasiparticle concentration x is exponentially small at low temperatures $T < 0.4T_c$ (Eq. 2.18).

The kinetic inductance is expressed in terms of the imaginary part of the a.c. electrical conductivity

$$L(\omega) = \frac{1}{\omega \sigma_2(\omega)}. \quad (4.2)$$

Following Mattis and Bardeen⁵⁸ the dynamic electric conductivity may be presented as follows

$$\frac{\sigma_2}{\sigma_n} = \frac{1}{\omega} \int_{\Delta-\omega}^{\Delta} d\epsilon [1 - 2f(\epsilon - \omega)] \frac{\epsilon(\epsilon + \omega) + \Delta^2}{(\Delta^2 - \epsilon^2)^{1/2} [(\epsilon + \omega)^2 - \Delta^2]^{1/2}}, \quad (4.3)$$

where σ_n is the conductivity in the normal state and $f(\epsilon)$ is the quasiparticle distribution function. In the low frequency limit ($\omega < \Delta, T$), Eq. 4.3 reduces to

$$\frac{\sigma_2}{\sigma_n} = \frac{\pi\Delta}{\omega} [1 - 2f(\Delta)], \quad (4.4)$$

and in thermodynamic equilibrium Eq. 4.4 has a well known form

$$\frac{\sigma_2(T)}{\sigma_n} = \frac{\pi\Delta(T)}{\omega} \tanh\left(\frac{\Delta(T)}{2T}\right). \quad (4.5)$$

Under the electromagnetic radiation the value of σ_2 is determined by changes in the superconducting gap and the nonequilibrium quasiparticle distribution function.

Nonequilibrium processes in a superconductor due to the electromagnetic radiation are described by kinetic equations for quasiparticles and phonons and also the equation for the order parameter (the gap). In the spatially homogeneous case, the equation for the gap is

$$\Delta = -g \int_{\Delta}^{\omega_D} \frac{d\epsilon}{(\epsilon^2 - \Delta^2)^{1/2}} [1 - 2f(\epsilon)], \quad (4.6)$$

where g is the BCS coupling constant and ω_D is the Debye temperature.

The kinetic equation for the quasiparticle distribution function has the form

$$Q_{\Omega} = I_{e-ph} + I_{e-e}, \quad (4.7)$$

where Q_{Ω} is the quasiparticle source due to the electromagnetic radiation of frequency Ω and I_{e-ph}, I_{e-e} are the quasiparticle-phonon and quasiparticle-quasiparticle collisions integrals. According to Eliashberg¹⁹ Q_{Ω} is given by

$$Q_{\Omega} = Q_{\Omega}^{(1)} + Q_{\Omega}^{(2)} + Q_{\Omega}^{(3)}, \quad (4.8)$$

where

$$Q_{\Omega}^{(1)} = \alpha_{\Omega} \rho(\Omega - \epsilon) [1 - f(\epsilon) - f(\Omega - \epsilon)], \quad (4.9)$$

$$Q_{\Omega}^{(2)} = Q_{-\Omega}^{(3)} = \alpha_{\Omega} \rho(\epsilon - \Omega) [f(\epsilon - \Omega) - f(\epsilon)]. \quad (4.10)$$

In Eqs. 4.9 and 4.10 $\rho(\Omega - \epsilon)$ is the combination of the quasiparticle density of states and the superconducting coherence factor,

$$\rho(\Omega - \epsilon) = \frac{\epsilon(\omega - \epsilon) - \Delta^2}{\epsilon[(\Omega - \epsilon)^2 - \Delta^2]^{1/2}} \theta(\Omega - \epsilon - \Delta). \quad (4.11)$$

The coupling of electrons with the electromagnetic radiation is given by a parameter

$$\alpha_\Omega = 2 \frac{e^2}{c^2} A_\Omega A_{-\Omega} D, \quad (4.12)$$

where A_Ω is the Fourier component of the vector potential and D is the diffusion coefficient.

Note that Eqs. 4.8-4.10 describe absorption of electromagnetic radiation by free electrons and neglect the electron band structure. The term $Q_\Omega^{(1)}$ corresponds to creation of new quasiparticles from the condensate, while the terms $Q_\Omega^{(2)}$ and $Q_\Omega^{(3)}$ correspond to the redistribution of quasiparticles to higher energy levels.

Let us consider the nonequilibrium quasiparticle distribution function and the gap suppression. The kinetic equation for the quasiparticle distribution function (Eq. 4.7) is solved by iteration

$$f(\epsilon) = f_0(\epsilon) + f_1(\epsilon) + f_2(\epsilon), \quad (4.13)$$

where $f_0(\epsilon)$ is the equilibrium Boltzmann distribution function and $f_1(\epsilon)$ is the main correction, which describes quasiparticles just above the gap ($\epsilon \sim \Delta$). The next correction $f_2(\epsilon)$ represents the distribution of high-energy nonequilibrium quasiparticles. According to Owen and Scalapino (Ref. 20), $f_1(\epsilon)$ has the form of the Boltzmann quasiequilibrium function with a nonvanishing chemical potential,

$$f_1(\epsilon) = \exp\left(\frac{\mu - \epsilon}{T}\right). \quad (4.14)$$

The chemical potential of quasiparticles is found from the quasiparticle number conservation law,

$$\int d\epsilon Q_\Omega^{(1)}(\epsilon) = \int d\epsilon I_{e-ph}(\epsilon). \quad (4.15)$$

For further discussion it is convenient to introduce two coefficients. The net quantum efficiency r describes of quasiparticle multiplication at high energies due to the electron-electron and electron-phonon interactions. The second coefficient η describes effects of phonon trapping on the quasiparticle lifetime, $\eta = \tau_L/\tau_R$. Using these coefficients, we can present a chemical potential of the nonequilibrium quasiparticles in the form

$$\mu = \frac{T}{2} \ln \left(1 + \frac{\alpha \Omega \Omega r \eta (p_F u)^2}{\pi^2 \beta \Delta^3 T} \exp \left(\frac{2\Delta}{T} \right) \right), \quad (4.16)$$

Now we consider coefficients r and η in different situations, which are summarized in Tab.

4. The mean free path of high-energy phonons is usually much smaller than the effective film thickness,

$$l_{ph}^> \approx l_{ph-e}^n(\Delta) \ll d/K, \quad (4.17)$$

and the high-energy phonons are in "chemical" equilibrium with quasiparticles, so their distribution function has the form

$$N_\omega = \exp \frac{2\mu - \omega}{T}. \quad (4.18)$$

The escape of a high energy phonon from the sample corresponds effectively to the loss of two quasiparticles. However, only phonons within a distance $l_{ph}^>$ of near the film-substrate interface can reach the boundary. As a result, the effective lifetime of quasiparticles in the film is given by

$$\tau_l = \tau_R \left[1 + \frac{\tau_{es}}{\tau_{ph-e}^{s,>}} \right]. \quad (4.19)$$

Therefore the coefficient η in Eq. 4.16 is $(1 + \tau_{es}/\tau_{ph-e})$. It is seen from Eq. 4.19 that if the phonon trapping is strong ($\eta \gg 1$), the quasiparticle lifetime is independent on the electron-phonon coupling.

Under condition of strong phonon trapping, the multiplications of nonequilibrium quasiparticles continues as long as quasiparticle energy ϵ diminishes to the value of the superconducting gap. It means that the multiplication coefficient r is

$$r = \frac{\Omega}{\Delta}. \quad (4.20)$$

In the opposite case ($\tau_{es}/\tau_{ph-e}^{s,>} \ll 1$), the avalanche-like multiplication of quasiparticles stops if the energy of radiated phonons reaches the critical value ω^* , at which the phonon-electron scattering time $\tau_{ph-e}^{s,>}(\omega^*)$ becomes of the order of the phonon escape time τ_{es} (Eq. 2.25) or the time of phonon decay into two low energy phonons with energy $\omega < 2\Delta$ (Eq. 2.24). The corresponding multiplication coefficient is

$$r = \frac{\Omega}{\omega^*} = \frac{\Omega}{\Delta} \frac{\tau_{es}}{\tau_{ph-e}^{s,>}(\Delta)}. \quad (4.21)$$

For high- T_c superconductors the phonons emitted in recombination processes have the energy which is of the order 400K. At such energies the relaxation of both acoustic and optical phonon modes is due to the phonon-phonon interaction, while the phonon-electron interaction is much weaker,

$$\tau_{ph-ph}^{>} \ll \tau_{ph-e}^{>}. \quad (4.22)$$

As a result, the high-energy phonons emitted by nonequilibrium quasiparticles decay into the low-energy phonons before they can be scattered by quasiparticles. Therefore, even in the frame of s-wave pairing the response of high- T_c superconductors drastically differs from the behavior of ordinary superconductors. Due to Eq. 4.22 the effect of the phonon trapping in high- T_c materials is absent and the quasiparticle lifetime is given by the quasiparticle recombination time (Eqs. 2.6 and 2.8). The avalanche-type processes of quasiparticle multiplication are realized only because of the electron-electron interaction. In this case the high energy correction $f_2(\epsilon)$ has the asymptotic form⁵⁹

$$f_2(\epsilon) \sim \left(\frac{\Delta}{\epsilon}\right)^4. \quad (4.23)$$

The corresponding coefficient r of the quasiparticle multiplication is given by

$$r = 1 + \frac{a\Omega^3}{\epsilon_F\omega_D}, \quad (4.24)$$

where the constant $a = \tau_{e-ph}(T_c)/\tau_{e-e}(T_c)$.

The suppression of the superconducting gap by the radiation, $\delta\Delta$ is then calculated by substituting Eqs. 4.14 and 4.15 into Eq. 4.6. The results for all considered cases have the form

$$\frac{\delta\Delta}{\Delta} = \frac{\alpha_{\Omega}\Omega r\eta(p_F u)^2}{8\beta\Delta^4} \left(\frac{2\Delta}{\pi T}\right)^{1/2} \exp\left(\frac{\Delta}{T}\right), \quad \frac{\alpha_{\Omega}\Omega r\eta(p_F u)^2}{\beta\Delta^3 T} \ll \exp\left(-\frac{2\Delta}{T}\right); \quad (4.25)$$

$$\frac{\delta\Delta}{\Delta} = \left(\frac{\alpha_{\Omega}\Omega r\eta(p_F u)^2}{2\beta\Delta^4}\right)^{1/2}, \quad \frac{\alpha_{\Omega}\Omega r\eta(p_F u)^2}{\beta\Delta^3 T} \gg \exp\left(-\frac{2\Delta}{T}\right). \quad (4.26)$$

In Eqs. 4.25-4.26 the crossover from one limiting case to another corresponds to the power of radiation at which the number of nonequilibrium quasiparticles, created by the electromagnetic radiation, is approximately equal to the number of thermal quasiparticles.

The shift of the kinetic inductance is determined by the correction to the distribution function $f_1(\epsilon)$ (Eqs. 4.14 and 4.15) and the gap suppression (Eqs. 4.25 and 4.26),

$$\frac{\delta L_k}{L_k} = \left[\left(1 + \frac{\alpha_{\Omega}\Omega r\eta(p_F u)^2}{\pi^2\beta\Delta^3 T} \exp\left(\frac{2\Delta}{T}\right) \right)^{1/2} - 1 \right] \exp\left(-\frac{\Delta}{T}\right). \quad (4.27)$$

Eq. 4.27 expresses the responsivity of the kinetic inductance detector in all considered cases.

5. KINETIC INDUCTANCE RESPONSE OF A D-WAVE SUPERCONDUCTOR AT LOW TEMPERATURES

A problem of a nonequilibrium detector on the base of a high- T_c superconductor is more complicated. We are still far from understanding the pairing mechanism in these materials. Results of recent microwave experiments, NMR, and photoemission data have unambiguously demonstrated the existence of low energy excitations consistent with superconducting gap nodes on the Fermi surface (see Ref. 60). Therefore, the low temperature properties of high- T_c oxides are drastically different from those of conventional superconductors. Instead of exponential temperature dependencies of the quasiparticle concentration and the response functions, power laws are observed.

Recent SQUID phase coherence data support the idea of d-wave pairing, resulting in the order parameter with lines of nodes⁶¹. The d-wave symmetry also stems from the model, in which pairing arises from the exchange of antiferromagnetic spin fluctuations⁶². Due to the presence of node lines, the low temperature behavior of a superconductor is quite sensitive to the presence of impurities. Without electron-impurity scattering the quasiparticle density of states is a linear function of the energy near the Fermi surface. Even low impurity concentrations modifies the quasiparticle density of states to a constant value, which depends on the electron-impurity potential. The effect of impurities was considered in several recent theoretical papers to explain the strong sample dependence of the experimental results⁶³.

Here we consider the nonequilibrium response of a d-wave pure superconductor. We restrict ourselves to the pure case for the following reasons. First, measurements of the electromagnetic penetration depth in perfect samples⁶⁴ have shown the linear temperature dependence consistent with the pure case. Second, real electron-impurity potentials in high- T_c superconductors are still unknown. And finally, as we will show, in the clean limit the parameters of a nonequilibrium detector are better. In the following we will calculate the electron specific heat, the temperature dependence of the kinetic inductance, and the electron and phonon relaxation rates, which are necessary to estimate the responsivity and the noise characteristics of the nonequilibrium kinetic inductance detector.

The superconducting order parameter with $d_{x^2-y^2}$ symmetry is

$$\Delta(\mathbf{p}) = \Delta \cos(2\phi), \quad (5.1)$$

where ϕ is the angle between the quasiparticle momentum and the a -axis of $Cu - O$ plane.

The quasiparticle density of states is given by⁶⁵

$$\nu_s(\epsilon) = \begin{cases} \nu(0) \frac{2}{\pi} \frac{\epsilon}{\Delta} K\left(\frac{\epsilon}{\Delta}\right), & \text{if } \epsilon < \Delta; \\ \nu(0) \frac{2}{\pi} K\left(\frac{\Delta}{\epsilon}\right), & \text{if } \epsilon > \Delta, \end{cases} \quad (5.2)$$

where $K(x)$ is the complete elliptic integral. As seen, the BCS singularity in the density of states is smeared. The heat capacity of the quasiparticles is easily calculated

$$\frac{C_q(T)}{C_e(T_c)} = \frac{6}{\pi^2 T_c} \int_0^\infty d\epsilon \epsilon \frac{\nu_s(\epsilon)}{\nu(0)} \frac{\partial f(\epsilon/T)}{\partial T}. \quad (5.3)$$

At low temperatures, the usual BCS exponential dependence of the heat capacity is replaced by power law behavior:

$$\frac{C_q(T)}{C_e(T_c)} = \frac{27}{\pi^2} \zeta(3) \frac{T^2}{T_c \Delta} \approx 1.54 \left(\frac{T}{T_c} \right)^2, \quad T \ll \Delta. \quad (5.4)$$

Due to smearing of the BCS singularity in the density of states, the quasiparticle scattering rate is no longer exponentially large with respect to the recombination rate. Therefore the Owen-Scalapino description of the photoresponse doesn't hold anymore. As we discussed above, the experiments near the superconducting transition show a very strong interelectron interaction. Assuming that the electron-electron interaction prevails over the electron-phonon scattering in the superconducting state, we will use the simplest kinetic scheme with the nonequilibrium electron temperature.

The kinetic inductance of a d-wave superconductor is strongly anisotropic. However, its temperature dependence is isotropic and is defined by the equation

$$\frac{L_k(T)}{L_k(0)} = 1 + \int \frac{\partial f}{\partial \epsilon} \frac{\nu_s(\epsilon)}{\nu(0)} d\epsilon. \quad (5.5)$$

At low temperatures ($T \ll \Delta$) we obtain

$$\frac{\partial L_k(T)}{\partial T} = 2 \ln 2 \frac{L_k(0)}{\Delta}. \quad (5.6)$$

Let us now consider relaxation of a quasiparticle with the energy ϵ and momentum \mathbf{p} , directed at the angle ϕ with respect to the a -axis. Following Ref. 30, the scattering rate due to the electron-phonon interaction may be presented as

$$\frac{(\tau_{e-ph}(\epsilon, p \cos(2\phi), T))^{-1}}{(\tau_{e-ph}^n(0, T))^{-1}}$$

$$\begin{aligned}
&= \frac{1}{7\zeta(3)} \left\{ \int_{\epsilon}^{\infty} d\omega \, \omega^2 \frac{\omega - \epsilon}{\sqrt{(\omega - \epsilon)^2 - (\Delta \cos(2\phi))^2}} \left(1 + \frac{(\Delta \cos(2\phi))^2}{\epsilon(\omega - \epsilon)} \right) \left[f\left(\frac{\omega - \epsilon}{T}\right) + N\left(\frac{\omega}{T}\right) \right] \right. \\
&\quad + \int_0^{\epsilon} d\omega \, \omega^2 \frac{\epsilon - \omega}{\sqrt{(\epsilon - \omega)^2 - (\Delta \cos(2\phi))^2}} \left(1 - \frac{(\Delta \cos(2\phi))^2}{\epsilon(\epsilon - \omega)} \right) \left[f\left(\frac{\omega - \epsilon}{T}\right) + N\left(\frac{\omega}{T}\right) \right] \\
&\quad \left. + \int_0^{\infty} d\omega \, \omega^2 \frac{\epsilon + \omega}{\sqrt{(\epsilon + \omega)^2 - (\Delta \cos(2\phi))^2}} \left(1 - \frac{(\Delta \cos(2\phi))^2}{\epsilon(\epsilon + \omega)} \right) \left[f\left(\frac{\omega + \epsilon}{T}\right) + N\left(\frac{\omega}{T}\right) \right] \right\}, \quad (5.7)
\end{aligned}$$

where $\tau_{e-ph}^n(0, T)$ is the relaxation time of electrons at the Fermi level in the normal state (Eq 2.1), $f(x)$ and $N(x)$ are the equilibrium Fermi and Planck distribution functions. In Eq. 5.7 the first term corresponds to a process in which a quasiparticle recombines with another quasiparticle to form a Cooper pair. The second and the third terms correspond to quasiparticle scattering processes with emission and absorption of a phonon, respectively. It is important that in all processes the change of the electron momentum direction is negligible. Therefore the available phase space for the small angle scattering is approximately the same as in the normal state. As a result, the electron-phonon relaxation rate only slightly changes due to the coherence factors. Note that for the electron-electron relaxation the large angle scattering is important, and to the electron-electron scattering rate is strongly modified in d-wave superconductor⁶⁶,

$$\frac{1}{\tau_{e-e}} \simeq \frac{T}{\Delta} \frac{1}{\tau_{e-e}^n}, \quad (5.8)$$

For illustrative purposes, in Fig. 2 we plot the energy and angular dependence of the electron cooling rate, which is the total rate of relaxation and recombination processes due to phonon emission. For convenience we count an angle from the b -axis, where the superconducting gap is zero. The gap increases with angle and reaches the value of ϵ at the critical angle. For electron energy $\epsilon = T$, recombination processes contribute to the cooling rate more than relaxation processes. As a result, due to the recombination coherent factor the cooling rate goes up slightly with angle. At energy level $\epsilon = 3T$, the contribution of relaxation processes dominates, and the cooling rate goes down with angle. At $\epsilon = 2T$, the electron cooling rate is practically independent of angle. We will present the energy flux

from the hot electron subsystem to the equilibrium phonons as $C_q(\theta - T_{ph})/\tau_{e-ph}^d$. Averaging the electron-phonon relaxation time over electron states in the nodal region, we find: $\tau_{e-ph}^d = c\tau_{e-ph}^n(0)$, where $c = 0.39$ for the Eliashberg function with quadratic frequency dependence. Therefore, the evolution of the electron temperature will have a form analogous to Eq. 3.6,

$$C_q \frac{d\theta}{dt} = -\frac{C_q}{\tau_{e-ph}^d}(\theta - T_{ph}) + \frac{I_0}{d}. \quad (5.9)$$

Taking into account Eqs. 5.4, 5.6, 5.8 and 5.9, we find the responsivity of the kinetic inductance detector,

$$\frac{\delta L_k}{L_k(0)I_0V} = \frac{0.65}{T_c} \frac{\tau_{e-ph}^d}{C_q(T)}. \quad (5.10)$$

Assuming that the phonon momentum relaxation on the film-substrate interface dominates over phonon-electron scattering, we can find the average phonon-electron scattering rate from the energy balance equation (Eq. 2.22). In this case it has a form

$$\tau_{ph-e} = \tau_{e-ph}^d \frac{C_{ph}}{C_q} \simeq \frac{\Delta}{T} \tau_{ph-e}^n. \quad (5.11)$$

Taking the value of $\tau_{ph-e}(T_c) = 65ps$ from Ref. 13, we find from Eqs. 3.10 and 5.11 that in films with thickness $\sim 20nm$ (the phonon escape time is $\sim 1ns$) the steady state nonequilibrium response in the superconducting state takes place in a wide temperature interval up to $0.3T_c$.

6. NOISE CHARACTERISTICS

In this section we consider the noise equivalent power (NEP) for different response mechanisms of a superconducting film to electromagnetic radiation. The noise equivalent power is defined as the noise power normalized by the square root of the frequency band. For a superconducting detector, it may be written as

$$NEP = (NEP_R^2 + NEP_{h\Omega}^2 + NEP_{1/f}^2 + NEP_{rel}^2)^{1/2}, \quad (6.1)$$

where the first term corresponds to the Johnson noise, the second is due to fluctuations of the background radiation, the third is $1/f$ noise, and the fourth describes fluctuations due to relaxation processes in the electron subsystem. One of the advantages of the kinetic inductance detector is that it operates exclusively in the superconducting state; therefore, the Johnson noise is absent. In the resistive detector the Johnson noise strongly depends on the geometry of a sample, and may be essentially suppressed. The $1/f$ noise ordinarily dominates at low frequencies. The main source of noise is presented by the last term in Eq. 6.1. As we discussed in previous sections, a mechanism of photoresponse is determined by a character of electron relaxation. Therefore, the relaxation noise is also closely related to the mechanism of photoresponse. Fundamental connection between fluctuations and relaxation is well known. In our particular case, the relaxation rate of the electron system determines the operating rate of a detector, while fluctuations of the electron distribution function due to relaxation determine its limiting noise characteristic.

Let us discuss the noise characteristics of different detectors in detail. For the bolometric response (see Sec. 3.1), the temperature fluctuations are

$$\langle (\delta T)^2 \rangle = \frac{T^2}{(C_e + C_{ph})V}, \quad (6.2)$$

where V is the volume of the sample. The spectrum width of temperature fluctuations is given by the inverse phonon escape time (Eq. 2.25), and the noise equivalent power for the bolometric detector is given by

$$(NEP_{rel;b})^2 = \frac{4T^2 C_{ph} V}{\tau_{es}}. \quad (6.3)$$

Now we discuss noise characteristics of nonequilibrium detectors. First, we discuss the nonequilibrium detector operating just below the superconducting transition, $0.97T_c < T < T_c$. In this case the photoresponse is governed by the dynamics of the order parameter. The characteristic time of the detector is the order parameter relaxation time (Eq. 2.21). The

order parameter fluctuations are

$$\langle (\delta\Delta)^2 \rangle = \frac{T_c^2}{\nu(0)V(T_c - T)}. \quad (6.4)$$

The spectrum of these fluctuations is limited by the inverse order parameter relaxation time.

Therefore, the noise equivalent power is given by

$$(NEP_{rel;\Delta})^2 = \frac{4T^2 C_e V}{\tau_\Delta} \frac{T}{T_c - T}. \quad (6.5)$$

In the temperature interval $0.9T_c < T < 0.97T_c$, the nonequilibrium photoresponse in high- T_c superconductors and in ordinary superconductors with short electron mean free path is described by a shift of the electron temperature. Here the spectrum band of the electron temperature fluctuations is the inverse electron-phonon relaxation time τ_{e-ph} . Fluctuations of the electron temperature are given by

$$\langle \delta\theta^2 \rangle = \frac{\theta^2}{C_e V}, \quad (6.6)$$

and the corresponding noise equivalent power is

$$(NEP_{rel;\theta})^2 = \frac{4T^2 C_e V}{\tau_{e-ph}}. \quad (6.7)$$

Now we consider the nonequilibrium response at low temperatures. In ordinary superconductors it is governed by a shift of the chemical potential of the quasiparticles (see Eq. 4.15). Fluctuations of the chemical potential of the quasiparticles in the film are

$$\langle \Delta\mu^2 \rangle = \frac{(T)^2}{n_{eqv} V}, \quad (6.8)$$

where n_{eqv} is the equilibrium quasiparticle concentration (Eq. 2.18). Taking into account Eq. 4.16, which expresses the shift of the chemical potential under the radiation, we obtain the noise equivalent power,

$$(NEP_{rel;\mu})^2 = 8\pi^2 \frac{\Omega^2}{r^2} \frac{\beta\nu(0)V\Delta^3 T}{(p_F u)^2} \left(1 + \frac{\tau_{es}}{\tau_{ph-e}^{s,>}}\right)^{-1} \exp\left(-\frac{2\Delta}{T}\right). \quad (6.9)$$

If the phonon trapping is negligible ($\tau_{es} < \tau_{ph-e}^{s, >}$), the spectrum of the chemical potential fluctuations is determined by the inverse recombination time (Eqs. 2.15 and 2.17). The strong phonon trapping ($\tau_{es}/\tau_{ph-e}^{s, >} \gg 1$) results in the effective multiplication of nonequilibrium quasiparticles (Eq. 4.20), in this case NEP may be presented as

$$(NEP_{rel;\mu})^2 = 4\Delta^2 \frac{n_{eqv} V}{\tau_l}, \quad (6.10)$$

and the spectrum of fluctuations is limited by the inverse quasiparticle lifetime, τ_l^{-1} (Eq. 4.19).

As we have discussed in Sec. 6, the response of high- T_c superconductors at low temperatures is likely to be described by the nonequilibrium electron temperature, and the decay time of photoresponse is approximately the same, as the electron-phonon scattering time in the normal state. The noise equivalent power may be expressed as

$$(NEP_{rel;d-wave})^2 = \frac{4T^2 C_q V}{\tau_{e-ph}^d}, \quad (6.11)$$

where C_q is the quasiparticle heat capacity (Eq. 5.4) and τ_{e-ph}^d is the average quasiparticle relaxation time (see Eq. 5.9).

We summarize characteristics photoresponse and parameters of superconducting detectors in Tab. 5. We also point out limitations of film thickness to observe a nonequilibrium response in steady-state measurements. In the next section we compare parameters detectors.

7. LIMITING CHARACTERISTICS OF SUPERCONDUCTING DETECTORS

The two basic parameters of superconducting detectors are the characteristic time τ_D and the detectivity $D^* = S^{1/2}(NEP)^{-1}$, where S is the operating square of the detector. They

are mutually connected, and in the frame of a definite detection mechanism, improvement of τ_D results in deterioration of D^* and vice versa. The characteristic times of different detection mechanisms and corresponding detectivities were discussed in previous sections. Here we evaluate numerically these characteristics and plot them in D^* versus τ_D coordinates (Fig.2).

It is important to note that the responsivity of a detector is determined by the change of macroscopic characteristics (such as the resistivity, the kinetic inductance, the magnetic flux, *etc*), which in turn are governed by change of the electron states due to radiation and energy relaxation. On the other hand, the limiting characteristics of a detector are defined only by the energy relaxation mechanism of the electron subsystem. That gives us a convenient basis for comparison of all resistive and inductive detectors.

1. Slow bolometers on the base of conventional superconductors were designed over many years and the limiting parameters have been reached. On Fig.2 we present parameters of the sensitive bolometer made from thermally isolated *Al* film⁶⁷: $NEP = 1.7 \cdot 10^{-15} W/Hz^{1/2}$ and $\tau = 10^{-1} s$. According to Eqs. 2.25 and 6.3, for the bolometric detector the parameter $I = D^* \tau^{-1/2}$ is independent on the effective thermal conductivity between a film and a substrate, and the parameter I is determined only by the heat capacity of the sensitive element. For the bolometer from Ref. 67 the value of I is $4.1 \cdot 10^{15} cm/J$. Because the heat capacities and the values of the Kapitza resistance at the interface do not significantly change from one material to another, the dotted line at Fig. 2 with $I = 4.1 \cdot 10^{15} cm/J$ approximately presents the limiting parameters of bolometers, operating at helium temperatures. Note that for fast bolometers with the characteristic time of $10^{-5} - 10^{-8} s$ the limiting parameters have not yet been reached, and obtained values of I are two orders of magnitude smaller than for slow bolometers.

2. Now we consider nonequilibrium detectors working in the resistive state near the superconducting transition. Detectors made of thin films of ordinary superconductors (*Al*,

Nb, *MoRe*, *NbN*) have characteristic times in the range $10^{-8} - 0.5 \cdot 10^{-10}$ s, corresponding to the electron-phonon scattering time τ_{e-ph}^n . The measured detectivity of these detectors⁶⁸ D^* turns out to be $10^{10} - 0.5 \cdot 10^{12} W^{-1} cm Hz^{1/2}$, that is in a good agreement with Eq. 6.6. We present on Fig. 2 the parameters of the *Nb*-detector.

3. Recently fast bolometric response of high- T_c superconductors with a nanosecond characteristic time has been intensively studied. As we discussed, in this case the energy relaxation is governed by phonon escape through a film-substrate interface. The phonon transparency coefficient for various substrates (*MgO*, *Al₂O₃*, *LaAlO₃*, *NdGaO₃* and *ZrO₂*) varies from 0.04 to 0.1. With *YBaCuO* heat capacity $0.9 J cm^{-3} K^{-1}$ we get the detectivity $D^* = 4 \cdot 10^7 W^{-1} cm Hz^{1/2}$.

4. As we have discussed in Sec. 3.3, the nonequilibrium detector based on *YBaCuO*, operating near the transition, will have a picosecond characteristic time. Both factors, increase of the operating temperature and strong electron-phonon interaction result in a short electron-phonon relaxation time, which is $\sim 1 ps$ at liquid nitrogen temperatures. According to Eq. 6.6 the detectivity of this detector is $D^* = 0.7 \cdot 10^7 W^{-1} cm Hz^{1/2}$ and $I = 10^{13} cm/J$. As seen, the last parameter is improved with respect to the bolometric response of high- T_c superconductors, because only the electron subsystem with relatively small heat capacity is heated by radiation.

5. Now let us consider a low temperature nonequilibrium detector made from a conventional superconductor. To be specific, we evaluate the parameters of the detector on the base of *Nb* film with a thickness $\sim 100 \text{ \AA}$ and the boundary phonon transparency $K \approx 0.1$. If the operating temperature changes from 1K to 3K, according to Eq. 4.18 the characteristic time, determined by the quasiparticle lifetime (Eq. 6.16), varies from 10ms to 40ns. Using Eq. 6.10 we find that in this temperature interval the detectivity changes from $\approx 2 \cdot 10^{16} W^{-1} cm Hz^{1/2}$ to $2 \cdot 10^{12} W^{-1} cm Hz^{1/2}$.

6. Finally, we discuss the low temperature *YBaCuO* nonequilibrium detector. Lack of

reliable experimental data does not allow us to predict its parameters more exactly than it is shown as region 6 in Fig. 2. The upper boundary corresponds to the operating temperature of 1K, the low boundary corresponds to 10K. The right boundary of the region has been drawn on the base of data from Ref. 69, where it was found that the low temperature electron-phonon relaxation rate in YBaCuO is approximately the same as in ordinary metals. The left boundary has been obtained using data from Ref. 5, these results show strong interaction between electrons and thermal phonons in high- T_c superconductors.

As seen from Fig. 2, the parameters of nonequilibrium detectors may be changed in wide ranges, and ultrafast or sensitive detectors may be realized. Using the nonequilibrium response, basic parameters of a detector may be significantly improved with respect to characteristics of superconducting bolometers and other detectors.

8. CONCLUSIONS

We analyzed the photoresponse of ordinary BCS-superconductors and high- T_c cuprates at low temperatures and near the superconducting transition. On the base of this analysis, we calculated limiting characteristics (responsivity, operating time, NEP) of superconducting detectors. Our main results are:

1. Near the superconducting transition the photoresponse of ordinary superconductors with small electron mean free path is well described by the two-temperature nonequilibrium heating model. This model also explains the basic features of photoresponse of high- T_c cuprates, in particular, the biexponential photoresponse decay has the same origin in new and traditional superconductors. However, the details of fast electron-phonon relaxation in cuprates at nitrogen temperatures are still unclear, and further improvement of photoreponse measurements will be necessary to provide more accurate data in a range of 1-100ps.

2. Our calculations show that due to the exponentially-small quasiparticle heat capacity and exponentially-large recombination time, the low-temperature kinetic-inductance response of ordinary superconductors is very promising for applications in sensitive detectors.

3. Using d-wave pairing model, we considered low-temperature photoresponse in cuprates. We conclude that due to small-angle character of electron-phonon scattering, the energy relaxation of quasiparticles in nodal regions is approximately the same as in the normal state. The difference originates only from the superconducting coherent factors in the scattering amplitude, and this difference turns out to be small in an essential energy interval $\epsilon \sim T$. Taking into account that the heat capacity of quasiparticles in nodal regions is significantly smaller than the electron heat capacity in the normal state, we can use the low temperature photoresponse of a superconductor with nodes for applications in the fast and sensitive detectors.

4. Phonon relaxation in a bulk d-wave superconductor is strongly anisotropic. However in thin films, due to frequent diffusion phonon scattering from interfaces, the effective phonon relaxation time is averaged over the wavevector direction and, as a result, it is significantly enhanced over its value in the normal state. Comparing the phonon escape time and the phonon-electron scattering time in a superconductor with nodal regions, we conclude that the phonon heat sink condition ($\tau_{es} < \tau_{ph-e}$) may be satisfied for temperatures up to $0.3 T_c$. Therefore, in this temperature range the bolometric effect may be suppressed in thin films. Recent measurements^{70,57} show the absence of bolometric tails in transient response at low temperatures and support this conclusion.

5. Nonequilibrium superconducting detectors are suitable for many applications. Using nonequilibrium photoresponse, one can essentially improve the operating time and NEP compare to characteristics of superconducting bolometers (see Fig. 2).

ACKNOWLEDGMENTS

The work is supported by the grant from US Army Advanced Technology Directorate and US Office of Naval Research. The authors are very grateful to N. Bluzer and J. Wilkins for stimulating discussion.

REFERENCES

1. A.V. Sergeev, A.D. Semenov, P. Kouminov et. al., Phys. Rev. B **49**, 9091 (1994).
2. P.L. Richards, J. Appl. Phys. **76**, 1 (1994).
3. E.M. Gershenzon, G.N. Goltsman, A.D. Semenov and A.V. Sergeev, Sol. St. Comm., **76**, 493 (1990).
4. N. Bluzer, Phys. Rev. B **44**, 10222 (1991).
5. E.M. Gershenzon, G.N. Goltsman, I.G. Gogidze, A.D. Semenov and A.V. Sergeev, Physica C, **185-189**, 1372 (1991).
6. M. Johnson, Appl. Phys. Lett., **59**, 1371 (1991).
7. A.D. Semenov, G.N. Goltsman, I.G. Gogidze, A.V. Sergeev, E.M. Gershenzon, P.T. Lang and K.F. Renk, Appl. Phys. Lett. **60**, 903 (1992).
8. A. Ghis, J.C. Vilegier, S. Pfister, M. Nail and Ph. Gibert, Appl. Phys. Lett. **63**, 551 (1993).
9. L.Shi, G.L. Huang, C. Lehane, D. Kim, H.S. Kwok, J. Swiatkiewicz, G.C. Xu and P.N.Prasad, Phys. Rev. B **48**, 6550 (1993).
10. A.D. Semenov, I.G. Goghidze, G.N. Goltsman, A.V. Sergeev and E.M. Gershenzon, Appl. Phys. Lett. **63**, 681 (1993).
11. L. Shi, G.L. Huang, C. Lehane et. al., Appl. Phys. Lett. **63**, 2830 (1993).
12. F.A. Hegmann and J.S. Preston, Phys. Rev. B **48**, 16023 (1993).
13. M. Lindgren, V. Trifonov, M. Zorin et. al., Appl. Phys. Lett. **64**, 3036 (1994).
14. F.A. Hegmann, R.A. Hudhes and J.S. Preston, Appl. Phys. Lett. **64**, 3172 (1994).

15. M. Danerud, D. Winkler, M. Lindgren, M. Zorin et. al., Appl. Phys., **76**, 1902 (1994).
16. A.M. Kadin, M. Leung, A.D. Smith and J.M. Murduck, Appl. Phys. Lett., **57**, 2847 (1989).
17. A. Frenkel, M.A. Saifi, T. Vencatesan et. al., J. Appl. Phys., **67**, 3054 (1990).
18. A. Frenkel, Phys. Rev. B **48**, 9717 (1993).
19. G.M. Eliashberg, Zh. Eksp. Teor. Phys. **52**, 1254 (1971).
20. C.S. Owen and D.J. Scalapino, Phys. Rev. Lett. **28**, 1559 (1972).
21. D.E. Prober, Appl. Phys. Lett. **62**, 2119 (1993).
22. M. Lindgren, M.A. Zorin, V. Trifonov et al., Appl. Phys. Lett. **65**, 3398 (1995).
23. E.N. Grossman, D.G. McDonald and J.E. Sauvageau, IEEE Trans. Magn. **27**, 2677 (1991).
24. N. Bluzer and M. Forrester, Optical Engineering **33**, 697 (1994).
25. A. Schmid, *Localization, Interaction, and Transport Phenomena* edited by B. Kramer, G. Bergman, and Bruynseraede, Springer-Verlag **61**, Berlin, Heidelberg, New York, Tokyo, p. 212 (1985).
26. M.Yu. Reizer and A.V. Sergeev, Zh. Eks. Teor. Fiz. **90**, 1056 (1986) [Sov. Phys. JETP **63**, 616 (1986)].
27. Constant λ is defined as $\frac{d\Sigma_{e-ph}}{d\epsilon}$, where Σ_{e-ph} is the electron self-energy due to the electron-phonon interaction. See e.g. A.A. Abrikosov, L.P. Gorkov and I.D. Dzyaloshinski, *Methods of Quantum Field Theory in Statistical Physics*, Dover Publications, Dover, N.Y. (1963).

28. A.A. Abrikosov, L.P. Gorkov and I.D. Dzyaloshinski, *Methods of Quantum Field Theory in Statistical Physics*, Dover Publications, Dover, N.Y. (1963)
29. B.L. Altshuler and A.G. Aronov, *Modern Problems in Condensed Matter Science* edited by A.L. Efros and M. Pollac, North Holland, Amsterdam, N.Y., 1 (1985).
30. S.B. Kaplan, C.C. Chi, D.N. Langenberg et.al., *Phys. Rev. B* **14**, 4854 (1974).
31. M.Yu. Reizer, *Phys. Rev. B* **39** 1602 (1989).
32. A. Schmid and G. Shon, *J. Low Temp. Phys.*, **20**, 207 (1975).
33. A.V. Sergeev, E.E. Aksaev, I.G. Gogidze et. al., in *Phonon Scattering in Condensed Matter*, edited by M. Meissner and R.O. Pohl (Springer, N.Y., 1993), p 405.
34. J.C. Culbertson, U. Strom, S.A. Wolf et. al., *Phys. Rev. B*, **39**, 12359 (1989).
35. G.L. Carr, M. Quijada, D.B. Tanner et. al., *Appl. Phys. Lett.*, **57**, 2725 (1990).
36. R.J. Stoner and H.J. Maris, *Phys. Rev. B* **48**, 16373 (1993).
37. C.D. Marshall, A. Tokmakoff, I.M. Fishman, C.B. Eom, J.M. Phillips and M.D. Fayer, *J. Appl. Phys.* **73**, 850 (1993).
38. S. Zeuner, H. Lengfellner, J. Bertz, K.F. Renk and W. Pretll, *Appl. Phys. Lett.* **61**, 973 (1992).
39. J.-P. Maneval, F. Chibane and R.W. Bland, *Appl. Phys. Lett.* **61**, 339 (1992).
40. E.M. Gershenzon, G.N. Goltsman, V.D. Potapov and A.V. Sergeev, *Soll. St. Comm.* **75**, 639 (1990).
41. A.J. Leggett, *Physica B* **199-200**, 291 (1994).
42. C.G. Smith and M.N. Wybourne, *Solid State Commun.* **57** 411 (1986).

43. J.F. DiTusa, K.Lin, M. Park et al., Phys. Rev. Lett. **68** 1156 (1992).
44. K. Chun and N.O. Birge, Phys. Rev. B **49** 2959 (1994).
45. G. Bergman, Phys. Rep. **107**, 1 (1984).
46. C.Y. Wu and J.J. Lin, Phys. Rev. B **50** 385 (1994), Europhys. Lett. **29** 141 (1995).
47. P.W. Watson and D.G. Naugle, Phys. Rev. B **51** 685 (1995).
48. D. Belitz and M.N. Wybourne, Phys. Rev. B **51** 689 (1995).
49. E.M. Gershenzon, M.E. Gershenzon, G.N.Goltsman et.al., Zh. Eksp. Teor. Fiz. **97** , 901 (1990) (Sov. Phys. JETP. **70**, 505 (1990)).
50. N. Bluzer, Phys. Rev. B **46**, 1033 (1992).
51. M. Johnson., Phys. Rev. Lett. **67**, 374 (1991).
52. M.E. Gershenzon, V.N. Gubankov and Yu.E. Zhuravlev, Zh. Eks. Teor. Fiz. **85**, 287 (1983) [Sov. Phys. JETP **58**, 167 (1983)].
53. B.J. Dalrymple, S.A. Wolf, A.C. Enrlich and D.J. Gillespie, Phys. Rev. B, **33**, 7514 (1986).
54. E.M. Gershenzon, M.E. Gershenzon, G.N.Goltsman et.al., Pis'ma Zh. Eksp. Teor. Fiz. **46** , 226 (1987) (Sov. Phys. JETP Lett. **46**, 285 (1987)).
55. A.D. Semenov, R.S.Nebosis, M.A. Heusinger and K.F. Renk, Physica C **235-240** 1971 (1994).
56. A.V. Sergeev, Inelastic Electron-Boundary Scattering: Electron Kapitza Conductivity and Dephasing Rate, Bulletin of APS, March Meeting 1995.
57. F.A. Hegmann, D. Jacobs-Perkins, S.H. Moffat et al., Appl. Phys. Lett. (1995), will be published.

58. D.C. Mattis and J. Bardeen, Phys. Rev. **111**, 412 (1958).
59. R.A. Vardanyan and B.I. Ivlev, Zh. Exsp. Teor. Fiz. **65**, 2315. (1973).
60. K. Kitazawa, Physica C **235-240** XXIII (1994).
61. D.A. Wollman, D.J. Van Harlingen, W.C. Lee, D.M. Ginsberg and A.J. Leggett, Phys. Rev. Lett. **71** 2134 (1993).
62. D. Pines, Physica B **199-200** 300 (1994).
63. Ye Sun and K. Maki, Phys. Rev. B **51** 6059 (1995).
64. W.N. Hardy, D.A. Bonn, D.C. Morgan, R. Liang and K. Zhang, Phys. Rev. Lett. **70**, 3999 (1993).
65. H. Won and K. Maki, Phys. Rev. B **49** 1397 (1994).
66. S.M. Quinlan, D.J. Scalapino and N. Bulut, Phys. Rev. B **49** 1470 (1994).
67. J. Clarke, G.I. Hoffer, P.L. Richards, N.H. Yeh, J. Appl. Phys. **48**, 4865 (1977).
68. E.M. Gershenzon et al., Sov. Phys. TP **34**, 195 (1989).
69. I. Iguchi, K. Nukui and K. Lee, Phys. Rev. B **50**, 457 (1994).
70. Y.S. Lai, Y.Q. Liu, W.L. Cao et al., Appl. Phys. Lett **66** 1135 (1995).

FIGURE CAPTIONS

Fig. 1. The angular and energy dependence of the electron relaxation rate in a nodal region of a d-wave superconductor at $T = 0.1\Delta$. Here ϕ is the angle between the quasiparticle momentum and the a -axis ($\Delta = 0$ at $\phi = \pi/4$; if $2(\phi - \pi/4) > \epsilon/\Delta$, the quasiparticle states are absent).

Fig. 2. Detectivity D^* and operating time τ_D of different superconducting detectors.

TABLE CAPTIONS

Tab. 1. Thermophysical characteristics of YBaCuO-film/substrate interface: the sound velocity of a substrate (u_s), the phonon scattering time in the substrate ($\tau_{ph,s}$), the phonon transparency coefficients K_{f-s} and K_{s-f} (Ref. 1), a critical width of a strip or a strip structure W_c (Eq. 3.1), and a time of phonon return to the film τ_R (Eq. 2.26).

Tab. 2. Summary of photoresponse relaxation times in thin Nb films: τ_1 is the decay time of the nonequilibrium response (τ_1 is independent on the film thickness), τ_2 is the decay time of the bolometric response (τ_2 is proportional to the film thickness). In Ref. 49 the critical thickness was determined from dependence of a decay time on the film thickness (see Eq. 3.9). The electron-electron scattering time for 20nm-film is calculated from Eq. 2.13.

Tab. 3. Summary of picosecond and nanosecond times of biexponential photoresponse decay in YBaCuO thin films.

Tab. 4. The quasiparticle multiplication coefficient r and lifetime extending $\eta = \tau_l/\tau_R$ in different regimes.

Tab. 5. Characteristics of photoresponse and parameters of superconducting detectors.

Here K_{f-s} is the transparency of a film/substrate interface, $l_{ph}^n = u\tau_{ph-e}$ is the phonon mean free path in the normal state of the film, $l_{ph}^{s,<} = u\tau_{ph-e}^{s,<}$ is the mean free path of low-energy phonons in the superconducting state, θ is the electron temperature (Eqs. 3.7 and 5.9), μ is the quasiparticle chemical potential (Eq. 4.16), C_e and C_{ph} are electron and phonon heat capacities, n_{eqv} is the equilibrium quasiparticle concentration (Eq. 2.18), C_q is the quasiparticle heat capacity of a d-wave superconductor (Eq. 5.4), r is the quasiparticle multiplication coefficient (see Tab. 4), τ_{es} is the time of phonon escape from the film (Eq. 2.25), $\tau_{ph-e}^{s,>}$ is the high-energy phonon scattering time in the superconducting state, $\tau_{e-ph}^n(0)$ is the scattering time of an electron at the Fermi surface (Eqs. 2.1-2.11), a, b and c are constants of the order of 1 (Eqs. 3.7 and 5.9).

Fig 1

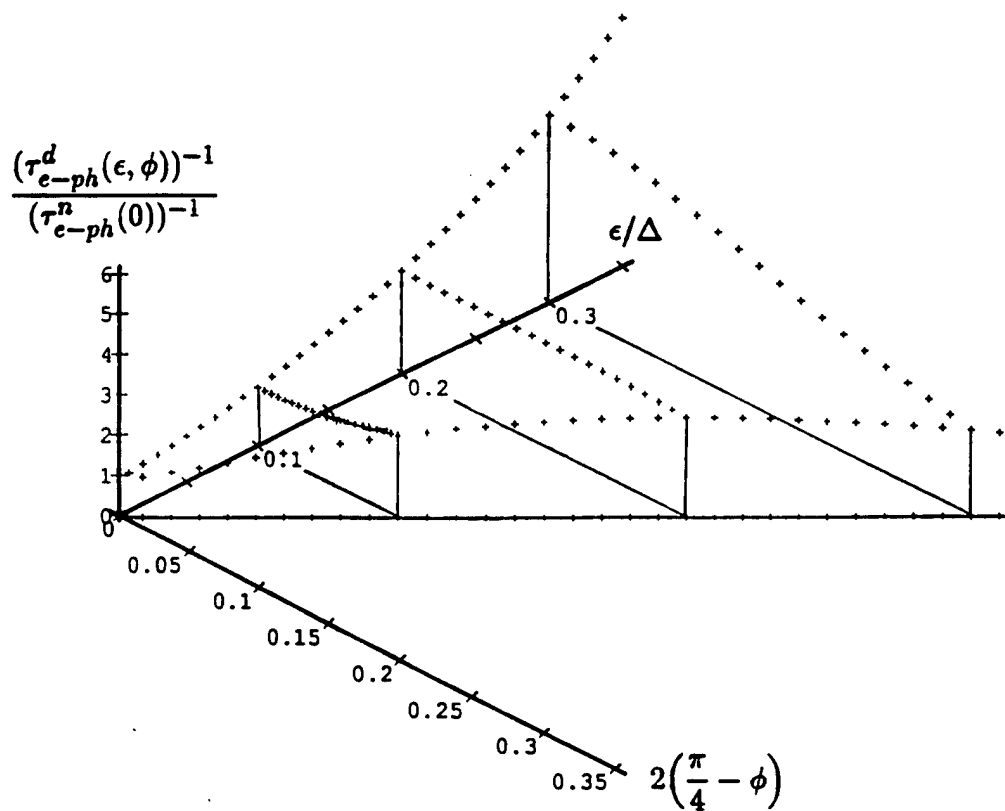


Fig. 1

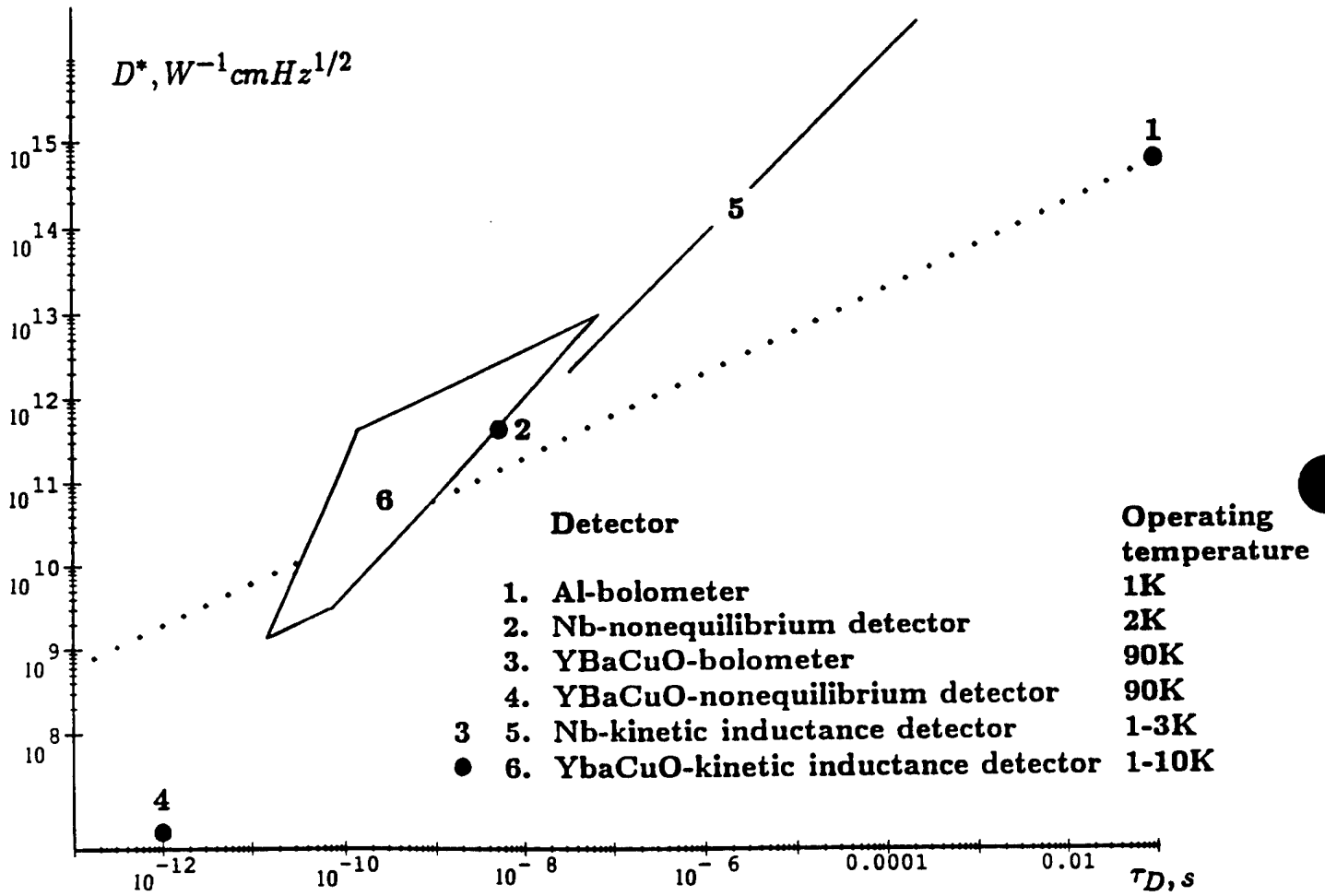


TABLE 1

Substrate	u_s (10^5 cm s^{-1})	$\tau_{ph,s}$ (ps)	$10^2 K_{f-s}$	$10^2 K_{s-f}$	W_c (μm)	τ_R (ns)
Al_2O_3	7.9	230	4.7	2.5	70	370
MgO	5	160	9.6	5.0	16	64
$LaAlO_3$	3	42	4.5	5.9	2.1	12
$NdGaO_3$	3	40	4.5	5.9	2.3	14
ZrO_2	3	1.4	-	-	$<< 0.1$	0.1

TABLE 2

Operating temperature (K)	Film thickness (nm)	$\tau_1(\tau_{e-ph})$ (ns)	$\tau_2(\tau_{es}, \tau_{dif})$ (ns)	Critical thickness(nm)	τ_{e-e} (ps)	Reference
1.6	6 and 20 100	5 absent	absent 12	68	14	49
4.2	6 and 20 100	0.9 absent	absent 3	33	5.2	49
6.7	20	0.43	3.2 - 6.0	< 20	3.3	51
9.2	20 and 40	< 0.8	> 5	< 20	2.2	50

TABLE 3

Thickness (nm)	λ (μm)	τ_1 (ps)	τ_2 (ns)	Reference
1000	500	not measured	40	34
300	2000	100(T=1.6K)	not measured	3
48, 168, 320	1-100	not measured	4, 22, 50	35
70	0.63	< 200	2	5
80	0.66	< 100	1.7	6
20	9.4	< 150	not measured	4
15, 30, 50	1	40, 100, 140	not measured	9
30-260	532	< 500	2-30	12
30	1.06	< 29	7	7
40	0.63 and 1.54	< 20	3.9	8
47-200	820	< 16	not measured	14
50, 60	0.8 and 10,6	1.8*	1.9-4.0	13,15

TABLE 4

Relaxation time hierarchy	Multiplication coefficient, r .	Lifetime extending, η .
$\tau_{es}(d) < \tau_{ph-e}^{s,>}(2\Delta) < \tau_{ph-ph}(2\Delta)$	$\frac{\Omega}{\Delta} \frac{\tau_{es}}{\tau_{ph-e}^{s,>}(2\Delta)}$	1
$\tau_{ph-e}^{s,>}(2\Delta) < \tau_{es}(d) < \tau_{ph-ph}(2\Delta)$	$\frac{\Omega}{\Delta}$	$\frac{\tau_{es}}{\tau_{ph-e}^{s,>}(2\Delta)}$
$\tau_{ph-ph}(\omega > 2\Delta) < \tau_{ph-e}^{s,>}(\omega > 2\Delta)$	$1 + \frac{a\Omega^3}{\epsilon_F \omega_D^2}$	1

TABLE 5

Response	Temperature range	Film parameters	Governing parameter	Responsivity r_R, r_L	Operating time τ_D	Detectivity D^*
Bolometric	$T \leq T_c$	$d > K_{f-s} l_{ph}^n$	T	$r_R = \left(\frac{1}{\delta T_c}\right) \frac{\tau_{es}}{C_{ph}}$	$\tau_b = \frac{C_e + C_{ph}}{C_{ph}} \tau_{es}$	$\left(\frac{\tau_{es}}{4T^2 C_{ph} V}\right)^{1/2}$
Non-equilibrium	$0.97T_c \leq T \leq T_c$	$d < K_{f-s} l_{ph}^n$	Δ	$r_R = \left(\frac{1}{\delta T_c}\right) \frac{\tau_{e-ph}}{C_e}$	$\tau_\Delta \sim \frac{T}{\Delta} \tau_{e-e}^n$	$\left(\frac{\tau_\Delta}{4T^2 C_e V} \frac{T_c - T}{T_c}\right)^{1/2}$
	$0.8T_c \leq T \leq 0.97T_c$	$d < K_{f-s} l_{ph}^n$	θ	$r_{=R} = \left(\frac{1}{\delta T_c}\right) \frac{\tau_{e-ph}}{C_e}$	$\tau_{e-ph} = ab \tau_{e-ph}^n(0)$	$\left(\frac{\tau_{e-ph}}{4T^2 C_e V}\right)^{1/2}$
	$T \leq 0.4T_c$, s-pairing	$d < K_{f-s} l_{ph}^{s, <}$	μ	$r_L = \frac{\tau_l r}{\Omega n_{eqv} \Delta} \exp(-\Delta/T)$	$\tau_l = \tau_R \left(1 + \frac{\tau_{es}}{\tau_{ph-e}^n}\right)$	$\left(\frac{\tau_l r}{4\Omega n_{eqv} \Delta V}\right)^{1/2}$
	$T \leq 0.4T_c$, d-pairing	$d < \frac{\Delta}{T} K_{f-s} l_{ph}^n$	θ	$r_L = \frac{0.65 \tau_{e-ph}^d}{T_c} \frac{C_q}{C_q}$	$\tau_{e-ph}^d = c \tau_{e-ph}^n(0)$	$\left(\frac{\tau_{e-ph}^d}{4T^2 C_q V}\right)^{1/2}$

Superconducting quantum detectors

Nathan Bluzer

Westinghouse Advanced Technology
Laboratories
Winterson and Nursery Roads, MS 3D12
Linthicum, Maryland 21090

Martin G. Forrester

Westinghouse Science and Technology
Center
1310 Beulah Road, Code S52
Pittsburgh, Pennsylvania 15235-5098

Abstract. The discovery of high-temperature superconductors (HTS) spawned many potential applications, including optical detectors. Realizing viable superconducting detectors requires achieving performance superior to competing and more mature semiconductor detector technologies, and quantum detector technologies in particular. We review why quantum detectors are inherently more sensitive than thermal or bolometric detectors. This sensitivity advantage suggests that for operation at cryogenic temperatures, we should be developing only quantum superconducting detectors. Accordingly, we introduce and describe the structure and the operation of a superconducting quantum detector with a superconducting quantum interference device (SQUID) readout circuit. The superconducting quantum detector, consisting of a superconducting loop, produces a photosignal in response to photoinduced changes in the superconducting condensate's kinetic inductance. The superconducting quantum detector is designed to operate only in the superconducting state and not in the resistive or transition states.

Subject terms: infrared technology; superconducting sensors; bolometric detectors; quantum detectors.

Optical Engineering 33(3), 697-703 (March 1994).

1 Introduction

The discovery of high-temperature superconductivity (HTS) by Bednorz and Muller¹ in 1986 evoked much excitement and a rush to find applications for the new discovery. One of the first proposed applications was for making optical detectors, and infrared detectors in particular. This proposed application was natural because infrared detectors operate at liquid nitrogen temperatures, just like high-temperature superconductors. Enomoto and Murakami² made the earliest photoresponse measurements using granular $\text{BaPb}_{0.7}\text{Bi}_{0.3}\text{O}_3$ and reported encouraging results. Soon, many more papers³⁻⁵ were published reporting on the photoresponse of different detector structures made in HTS materials. However, the photoresponse mechanism was not clearly identified nor was the ultimate expected detector performance. After much examination, it was shown⁶ that the reported photoresponse signals were consistent with a bolometric response. This was a very discouraging turn of events because the sensitivity of bolometric detectors is far less than the sensitivity of quantum detectors.

However, because of inherent limitations in semiconductor-based quantum detectors, the search for a superior superconductor-based quantum detector persists. Specifically, the main improvements over semiconductor-based detectors sought are a broadband photoresponse and operation at very

high speeds. Typically, semiconductors consume more power at higher operating speed, thus the desire to include high-speed signal processors with the detectors is incompatible with cooling constraints. Furthermore, broadband sensing, at very long infrared wavelengths, with semiconducting quantum detectors demands much lower operating temperatures than 77 K. HTS offers two attractive potentials: first, superconducting electronics is the only technology offering high-speed performance at low power, and second, the small energy gap in HTS materials offers the possibility of broadband photodetection. For these reasons the development of HTS broadband superconducting detectors is being actively pursued.

In this paper, we report on the progress attained toward realizing HTS superconducting quantum detectors. We begin by reviewing the inherent sensitivity advantage of quantum detectors over bolometric detectors in Sec. 1.1. This is followed by a description of the limitations of the conventional superconducting detectors, given in Sec. 1.2. Finally, Sec. 2 describes our novel approach to realizing a superconducting quantum detector.

1.1 Sensitivity of Bolometers and Quantum Detectors

Bolometers operate as thermal equilibrium devices, whereas quantum detectors operate as nonequilibrium devices. The performance of each detector category is ultimately limited by the detector's noise level. Photon shot noise is the ultimate sensitivity limit of an ideal detector. For very low photon flux levels, the detector's noise level sets the sensitivity limit. Here we review the operation of each detector category and provide expressions for the sensitivity limit of each. It be-

Paper IRT-37 received July 24, 1993; revised manuscript received Sep. 2, 1993; accepted for publication Sep. 12, 1993. This paper is a revision of a paper presented at the SPIE conference on Infrared Technology XIX, July 1993, San Diego, Calif. The paper presented there appears (unrefereed) in SPIE Proceedings Vol. 2020. © 1994 Society of Photo-Optical Instrumentation Engineers. 0091-3286/94/\$6.00.

comes evident that quantum detectors are more sensitive than bolometric detectors.

In bolometers, photosignals are produced when the photoabsorbed photons' energy is quickly transferred into thermalized phonons, thereby changing the lattice's temperature. The transfer process of the photons' energy into the lattice is very fast relative to the bolometric detector's response time. Although photoabsorption in a bolometer occurs via intermediate quantum excitations of electrons or phonons, the lifetime of these intermediate excitations is very short and the excitation energy is quickly thermalized to produce a change in the lattice's temperature. Thus, the signal levels in a bolometric detector correspond to the change in the value of the lattice's temperature T . Similarly, the sensitivity^{7,8} of a bolometer is limited by the thermal fluctuations in the lattice's temperature ΔT^2 . For an object with heat capacity C connected to its surroundings by a thermal conductance G , the object's temperature change ΔT is related to its power exchange $W(t)$ with the surroundings by

$$C \frac{d\Delta T}{dt} + G\Delta T = W(t) \quad (1)$$

Using this expression and integrating over all frequencies,⁷ the mean-square value of the power flow from the body ΔW_T^2 can be expressed as

$$\Delta W_T^2 = 4k_B T^2 G \Delta f, \quad (2)$$

where Δf is the frequency band of interest. The smallest value for the object's power fluctuations with its surroundings occurs for the smallest value of conductance G , or the conductance of free space $4T^3\sigma A_D$, where σ is the Stefan-Boltzmann constant and A_D is the surface area of the object. Incorporating both equations, the mean-square value^{6,7} of the power flow from the body into free space is

$$\Delta W_T^2 = 16A_D k_B \sigma T^5 \Delta f. \quad (3)$$

The resolution or sensitivity of a bolometric detector is limited to the value of the power fluctuations with the surroundings, and this limit cannot be reduced by readout circuits.

In quantum detectors, photoabsorption efficiently channels the photons' energy directly into the production of quantum excitations, which may have relatively long lifetimes, creating a nonequilibrium. The nonequilibrium consists of an excess population of excited states over the thermal equilibrium population. The signal and the noise in quantum detectors correspond to the excess nonequilibrium population and the fluctuations therein, respectively. Thus for a given lattice temperature, different nonequilibrium levels exist, unlike in bolometric detectors. The sensitivity of a quantum detector is limited by the larger of (1) the minimum electronic noise in the detector ΔW_{QE} or (2) the photon radiation shot noise ΔW_{QP} . These noise quantities (ΔW_{QE} , ΔW_{QP}) are expressed as an average power fluctuation in the quantum detector^{6,7} as

$$\Delta W_{QE} = 4k_B T \Delta f, \quad (4a)$$

$$\Delta W_{QP} = \left[\Delta f A_D \left(\frac{hc}{\lambda_c} \right)^2 \int_0^{\lambda_c} \frac{2\pi c \lambda^{-4} d\lambda}{\exp(hc/\lambda k_B T) - 1} \right]^{1/2}, \quad (4b)$$

where c is the speed of light, λ is the wavelength, λ_c is the cutoff response of the detector, and h is Planck's constant. It should be evident from the integral in Eq. (4b) that the photon radiation shot noise in the quantum detector is band limited by the cutoff wavelength λ_c . In bolometric detectors, there is no spectral band limiting and hence the photon noise is significantly higher. Evaluating at 77 K, the noise power expressions for bolometric and quantum detectors (operating at a 30-Hz frame rate), we find that the noise power $(\Delta W_T^2)^{1/2}$ in a bolometric detector is significantly higher than the noise power in a quantum detector, each detector being 10^{-4} cm^2 in area. The bolometer's noise power $(\Delta W_T^2)^{1/2}$ is calculated to be 10^{-13} W , for a scene and a detector operating temperature of 77 K. The Johnson noise power (ΔW_{QE}) for a quantum 10^{-4} cm^2 detector operating at 77 K is $1.4 \times 10^{-19} \text{ W}$. Additionally, the radiation shot noise for 3 to 5 μm (8 to 12 μm) operation is 10^{-19} W (10^{-15} W). Combining the radiation shot noise with the detector's Johnson noise in quadrature, it becomes evident that the noise in quantum detectors is much less than the noise in bolometric detectors. These calculations clearly illustrate that at liquid nitrogen temperatures, quantum detectors are inherently more sensitive than thermal detectors. This preference for bolometric versus quantum detectors is independent of the specific detector signal generation mechanism, e.g., polarizability, resistivity, reflectivity, etc. Note that in addition to minimizing the noise levels in a detector, the signal levels need to be maximized to facilitate the performance of the readout circuits. The photosignal levels in bolometric detectors are maximized with minimum values for C and G , which ultimately puts severe restrictions of the operating frame rate of bolometric detectors. In quantum detectors, the photosignal levels are maximized with maximum values for the excitation lifetimes and much higher operating frame rates are possible.

1.2 Conventional Superconducting Detectors

Like semiconductors, superconducting detectors can be grouped into two main categories: quantum and bolometric (or thermal) detectors. Several different detectors have been realized in low- and high-temperature superconductors and they can be classified into the categories mentioned. Other exotic mechanisms of detection, such as photon-induced vortex-antivortex nucleation and photon-enhanced flux-flow, have been proposed⁹ but are not well understood vis-à-vis the four detector categories enumerated below.

1. Thermal detectors, where the energy from incident photons changes some temperature-dependent property of the material, such as resistance. Transition edge bolometers have been realized in low-temperature superconductor (LTS) and HTS materials, and their sensitivity is limited by the thermal energy fluctuations of the lattice and the photon flux. These detectors provide attractive performance especially for long-wave ($>20 \mu\text{m}$) detection where semiconductors require liquid helium operating temperatures.
2. Josephson-effect-based detectors, which make use of the nonlinear interaction between the incident photon's electromagnetic field and the high-frequency oscillating currents and voltages in a biased Josephson junction to perform millimeter-wave mixing and direct detec-

tion. These devices are particularly useful for millimeter- and submillimeter-wave detection.

3. Quasiparticle tunneling devices, such as superconductor-insulator-superconductor (S-I-S) mixers and direct detectors, where the incident photons are absorbed by quasiparticles, allowing tunneling events that would otherwise be energy forbidden to affect the junctions current-voltage (I-V) characteristics.
4. Pair-breaking detectors, where incident photons with energy larger than the energy gap break Cooper pairs, leading to changes in such macroscopic parameters as the superconducting gap and the kinetic inductance. Because of the difficulty of making S-I-S structures in HTS, this fourth detector category has received the most attention and is described in the following.

The fourth category is the least developed from a historical and practical standpoint. It can provide thermal as well as quantum detectors critically depending on the material parameters such as quasiparticle recombination time, which is not relevant to the other categories described. In HTS materials, the quasiparticle lifetime and the theory for predicting it are unknown. What is accepted is the existence of Cooper pairs in HTS with a minimum energy 2Δ required to break them. Thus, a basic mechanism of a superconducting quantum detector is to have photons with energy greater than 2Δ to break Cooper pairs and create excess quasiparticles.

To efficiently detect the excess quasiparticle population produced by photon depairing one must measure a property that is sensitive to all such quasiparticles. These include the voltage across a series of superconductive weak links, the microwave surface resistance of the superconductor, and the kinetic inductance of the superconductor.

Approaches pursued previously included the measurement, in granular HTS films, of the voltage signal induced by laser radiation, caused by local suppression of the gap, and thus the intergranular critical current in the film. However, in such a situation, only those quasiparticles created within a distance of order of the coherence length from a grain boundary are effective in reducing the intergranular critical current, and thus producing a voltage signal. The area efficiency of such a detector goes (in two dimensions) as the ratio of the coherence length to the grain size squared $(\xi/L_g)^2$, which for a typical granular YBCO film might be of order 10^{-7} . This is an unacceptably poor area efficiency (equivalent to a very poor effective quantum efficiency) and it is incompatible with a high-performance detector.

Using microwave circuits we can measure changes in the microwave reflectivity¹⁰ and resonator Q produced with photoabsorption. These detector approaches are sensitive to the entire quasiparticle or superconducting condensate population. Such techniques are not practical for detector array development because the size of the microwave readout circuits is incompatible with the small size of detectors, about $50 \times 50 \mu\text{m}^2$.

Another method sensitive to the entire quasiparticle or condensate population monitors the kinetic inductance of a superconducting film incorporated into a superconducting quantum interference device (SQUID) loop. The period of the threshold characteristic of gate current I_g versus control current I_c is given by Φ_0/L , where Φ_0 is the flux quantum

and L is the sum of the geometrical and kinetic inductances of the SQUID loop.¹¹ Thus, biasing at fixed values of I_c and I_g in the voltage state, the voltage will be a sensitive function of the kinetic inductance, and thus of the excess quasiparticle population. The disadvantage of such a scheme is that the SQUID must operate in the voltage state, and a calculation of the sensitivity of such a detector based on the measured noise characteristics of even the best dc SQUIDs yields extremely poor detectivity.

A more practical technique, and one that is also sensitive to all the quasiparticle's produced, is to measure the kinetic inductance \mathcal{L} of the condensate in the superconductor under irradiation. The kinetic inductance is a measure of the inertia of the Cooper pairs in a superconductor and is proportional to the reciprocal of the Cooper pair density n (see Sec. 2). With this approach, the detector is maintained in the superconducting current state (low noise) and changes in its kinetic inductance are monitored as a change in the magnetic field, as detailed in Sec. 2.

2 Quantum Superconducting Kinetic Inductance Detectors

The description of the quantum superconducting kinetic inductance detector (QSKID) illustrated in Fig. 1 is given in this section. We include the basis for the approach selected, the QSKID structure, the operating principle, and projected performance. Finally, we present an integrated QSKID with a SQUID readout circuit.

2.1 Detector Approach

Realizing a viable QSKID requires meeting several important technical objectives. First and foremost, the detector operation and structure needs to demonstrate a quantum response. The quantum response needs to occur with low electrical noise realizable in a zero-resistance superconducting state. Maximum photoresponse is desirable and is obtainable with a maximum quasiparticle lifetime. The readout circuit of the QSKID is to be simple, specifically a SQUID circuit. The

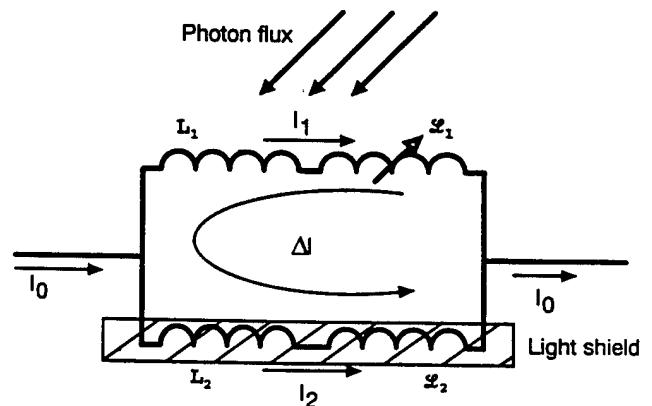


Fig. 1 QSKID structure, represented here by its equivalent circuit with magnetic L and kinetic \mathcal{L} inductances, consists of a superconducting loop biased with a dc current I_0 . The bias current splits between branch 1 and 2 of the superconducting loop producing branch currents I_1 and I_2 , respectively. For identical branches, i.e., with the same kinetic and magnetic inductance, current I_1 is equal to current I_2 . Changing the kinetic inductance by photodepairing in only one branch gives rise to a circulating photocurrent ΔI , producing a detectable magnetic field.

QSKID structure compatible with the aforementioned objectives includes

1. no Josephson junctions or weak links in the detector structure, thus facilitating manufacturability
2. maximum photoresponse amplitude
3. noise-equivalent power (NEP) superior to thermal detectors facilitated by operation in the zero-resistance superconducting state
4. broadband response, UV to far infrared ($\lambda_C > 20 \mu\text{m}$)
5. detector structure compatible with a 100% fill factor.

From a manufacturability point of view it is undesirable to use Josephson junctions or weak-link-based detectors. First, the coherence length in high T_C materials is too short for making Josephson junctions, and making reliable weak links in high T_C materials is very difficult. Second, the required weak-link area for each detector makes a large focal plane impractical. In high T_C , the coherence length ξ is very small ($< 2 \text{ nm}$) and for a detector to be detected it needs to be absorbed within a coherence length of the junction. Because a typical detector is about $50 \times 50 \mu\text{m}$ in area, many weak links would be needed to provide a 100% fill factor. The weak links would have to be separated by about 2 nm and span the detector width. An alternative is a vertical geometry where a single weak link per detector is used and it is oriented perpendicular to the incident photons. Neither geometries are technologically practical if we recognize that a typical focal plane is expected to have thousands of detectors. The total cross-sectional area of the weak links would grow to greater than $1 \times 1 \text{ cm}^2$. Such a detector array would need to satisfy demanding critical current uniformity requirements. Junctions with a nonuniform critical current density distribution would have significant fractions of areas with zero current flow, because of the small Josephson penetration depth, resulting in insensitive regions.

The second issue deals with maximizing the photoresponse amplitude. It has been mentioned earlier that the QSKID's responsivity is directly proportional to the lifetime of the quasiparticle excitations. The quasiparticle lifetime is minimized as the temperature increases toward T_C , thereby reducing the photoresponsivity. Quasiparticle lifetime reduction occurs because as the temperature increases, so does the number of quasiparticles and therefore the likelihood of finding two with opposite momentum to recombine into a Cooper pair. Making use of phonon-trapping phenomena and operating well below T_C , the quasiparticle lifetime and thus the photoresponse amplitude are maximized.

The third objective is the use of a detector structure not operating in the voltage state. Satisfying this criterion is important to achieve low operating power and minimum noise operation. If we operate high T_C detectors in a voltage state (with a gap voltage of about 20 mV) and at a bias current of 10 mA , the power consumed by each detector is about 0.2 mW . With thousands of detectors, this becomes a significant and an intolerable load on the refrigerator. Furthermore, given the low resistance of superconductors operating in a voltage state, the current shot noise would be too large, leading to poor sensitivity. Using voltage readout circuits, to take advantage of the small voltage noise, is unacceptable because of refrigeration requirements. Very low noise voltage sem-

iconducting readout circuits consume too much power to be compatible with large, low-power focal plane arrays. Thus if low power and low noise operation are sought the detector needs to remain in the zero-resistance superconducting state.

The fourth and fifth objectives are important from an operational point of view. HTS materials have a small energy gap and therefore are expected to respond from x rays to far infrared ($\lambda_C > 20 \mu\text{m}$). The need for a high fill factor detector structure is to simply maximize the detector quantum efficiency and performance.

A QSKID structure has been formulated¹² to satisfy the objectives raised in this section. The detector structure is illustrated in Fig. 1, where a single square superconducting loop forms the detector. No weak links are used, and the detector is made simply of a thin film patterned into a square loop. The output signal is a magnetic flux produced by the circulating current in the square loop. Details on the operation of this QSKID are given next.

2.2 QSKID Structure and Operation

In this section, the operation of the QSKID is described and the responsivity is computed. First, the operating constraints are computed. Next, a photon flux is used to cause a perturbation to the quiescent operating condition from which the responsivity is computed.

The current division between the QSKID's two branches is adjusted to minimize the total energy of the detector. The total energy (E) of the QSKID is made up of the magnetic field contribution (E_M) and the kinetic energy (E_K) of the supercurrent. For the QSKID structure in Fig. 1, the input current I_0 (less than the critical current) is divided between the two branches yielding currents I_1 and I_2 . The total magnetic field energy E_M stored in the magnetic inductances L_1 and L_2 , of branches 1 and 2, respectively, is

$$E_M = \frac{1}{2} L_1 I_1^2 + \frac{1}{2} L_2 I_2^2. \quad (5)$$

The kinetic energy E_K of the supercurrent I_0 flowing in branches 1 and 2, expressed in terms of the Cooper pair volume density n , the Cooper pair velocity v , the Cooper pair mass $2m$, the pair's electronic charge $2e$, the length of each branch ℓ , and the cross section of each branch A is

$$E_K = (n_1 A_1 \ell_1) m v_1^2 + (n_2 A_2 \ell_2) m v_2^2. \quad (6)$$

Recognizing that $I_1 = 2n_1 A_1 e v_1$ and $I_2 = 2n_2 A_2 e v_2$, we can recast Eq. (6) to obtain an expression for E_K in terms of I_1 and I_2 as

$$E_K = \frac{1}{2} \mathcal{L}_1 I_1^2 + \frac{1}{2} \mathcal{L}_2 I_2^2. \quad (7)$$

The recasting of Eq. (6) in terms of supercurrents I_1 and I_2 instead of v_1 and v_2 results in a form similar to Eq. (5) for the magnetic energy E_M . The two coefficients \mathcal{L}_1 and \mathcal{L}_2 provide a convenient form for expressing the kinetic energy of the supercurrent in terms of currents I_1 and I_2 . Because the forms of Eqs. (5) and (7) are similar, the coefficients \mathcal{L}_1 and \mathcal{L}_2 are labeled as kinetic inductances in correspondence to the magnetic inductance label given to L_1 and L_2 in Eq. (5). Equations for the kinetic inductances, associated with

the kinetic energy of the supercurrent flow in a rectilinear geometry QSKID, are defined as

$$\mathcal{L} = \left(\frac{\ell}{A} \right) \frac{m}{2e^2 n} \quad (8)$$

The kinetic inductance is a function of the detector's geometry and is inversely proportional to the Cooper pair density n . Combining Eqs. (5) and (7), the QSKID's total energy E becomes

$$E = \frac{1}{2} (L_1 + \mathcal{L}_1) I_1^2 + \frac{1}{2} (L_2 + \mathcal{L}_2) I_2^2 \quad (9)$$

Division of current $I_0 = I_1 + I_2$ between branches 1 and 2 (in Fig. 1) into I_1 and I_2 is according to the minimum energy constraint, or

$$\frac{\partial E}{\partial I_1} = \frac{\partial E}{\partial I_2} = (L_1 + \mathcal{L}_1) I_1 - (L_2 + \mathcal{L}_2) I_2 = 0 \quad (10)$$

The QSKID's minimum energy criterion and its quiescent operating condition require the current division between the two branches to satisfy

$$(L_1 + \mathcal{L}_1) I_1 = (L_2 + \mathcal{L}_2) I_2 \quad (11)$$

A photoresponse occurs in the QSKID when one branch, branch 1, for example, is exposed to a photon irradiance E_p sufficiently energetic to break Cooper pairs. As Cooper pairs are broken, the kinetic inductance \mathcal{L}_1 will increase [see Eq. (8)]. A change in the kinetic inductance of $\delta \mathcal{L}_1$ in branch 1 changes by ΔI_1 the current flowing in branch 1, or equivalently, produces a circulating current ΔI_1 in the QSKID loop. Taking the differential of Eq. (11), an expression for the photoresponse current is obtained. The induced current ΔI_1 is expressed in terms of the changes in the kinetic inductance $\delta \mathcal{L}_1$ of branch 1 as

$$\Delta I_1 = -I_1 \frac{\delta \mathcal{L}_1}{(L_1 + \mathcal{L}_1 + L_2 + \mathcal{L}_2)} \quad (12)$$

Note that the photoresponse current ΔI_1 can also be computed from fluxoid conservation requirements, and the results are the same as given by Eq. (12), derived from minimum energy requirements. Specifically, in a superconductor the condensate described by a wave function that in general can be expressed by a complex quantity $\psi(x) = \sqrt{n(x)} e^{j\varphi}$. At any given point x inside the superconductor the density of Cooper pairs is given by $n(x)$, where $n(x) = \psi^*(x)\psi(x)$. Writing out explicitly the current density in a superconductor using the canonical momentum, we obtain

$$\nabla \varphi = \frac{2\pi}{\Phi_0} \left(\mathbf{A} + \frac{m}{2e^2 n} \mathbf{J}_s \right) \quad (13)$$

where $\Phi_0 = h/2e$, \mathbf{A} is the vector potential, and \mathbf{J}_s is the supercurrent density. The closed loop of the detector is made from a superconducting film thinner than the magnetic penetration depth. Thus the supercurrent \mathbf{J}_s does not vanish anywhere inside the QSKID loop, Γ , and the \mathbf{J}_s term in Eq. (13)

cannot be made equal to zero. Because the superconductor's wave function $\psi(x)$ is single valued, a superconducting current flowing in a closed loop Γ (see Fig. 1) has a phase φ that can only change by $2\pi N$, where N is an integer. Performing the closed loop line integration on Eq. (13), we obtain

$$\int_{\Gamma} \mathbf{B} \cdot d\mathbf{S} + \oint_{\Gamma} \frac{m}{2e^2 n} \mathbf{J}_s \cdot d\boldsymbol{\ell} = N\Phi_0 \quad (14)$$

where \mathbf{B} is the magnetic field inside the detector's square loop and \mathbf{S} is the area enclosed by the curve Γ . Completing the integration in Eq. (14) and making use of Eq. (8), we obtain the expression

$$L_1 I_1 - L_2 I_2 + \mathcal{L}_1 I_1 - \mathcal{L}_2 I_2 = N\Phi_0 \quad (15)$$

Taking the differential I_1 in Eq. (15) relative to the changes in the kinetic inductance $\delta \mathcal{L}_1$ produces the same result as given by Eq. (12), derived from minimum energy requirements. The magnetic field $\mathbf{B}_{\text{QSKID}}$ produced by the circulating current ΔI is a measure of the absorbed photon irradiance E_p .

2.3 QSKID Responsivity

The QSKID's responsivity \mathfrak{R} in webers per watt is expressed in terms of the incident photon irradiance E_p . The change in the kinetic inductance $\delta \mathcal{L}_1$ caused by this irradiance is

$$\delta \mathcal{L}_1 = \left(\frac{\partial \mathcal{L}_1}{\partial n_1} \right) \left(\frac{\partial n_1}{\partial E_p} \right) E_p = -\frac{\mathcal{L}_1}{n_1} \left(\frac{\eta \tau_{\text{eff}}}{d} \right) E_p \quad (16)$$

where n_1 , η , τ_{eff} , and d are, respectively, the Cooper pair density, the number of Cooper pairs broken by each photon, the effective quasiparticle lifetime, and the detector thickness. The optical power P incident on the detector with an optical area A_D is simply the product of three terms:

$$P = A_D E_p h\nu \quad (17)$$

The QSKID's responsivity \mathfrak{R} in webers per watt is computed by combining Eqs. (12), (16), and (17) to yield

$$\begin{aligned} \mathfrak{R}(\text{webers/watt}) &= (L_1 + L_2) \frac{\partial I_1}{\partial P} = \\ &= I_1 \left(\frac{L_1 + L_2}{L_1 + \mathcal{L}_1 + L_2 + \mathcal{L}_2} \right) \\ &\times \left(\frac{\eta}{A_D n_1 d} \right) \left(\frac{\mathcal{L}_1 \tau_{\text{eff}}}{h\nu} \right) \end{aligned} \quad (18)$$

The responsivity is expressed as a product of four factors. The first factor is simply the bias current I_1 flowing through the branch illuminated by the photon irradiance. This is exactly given by Eq. (11), and for a balanced detector it is equal to $I_0/2$. The second factor in Eq. (18) is that the ratio of inductances is equal to about unity, because the kinetic inductances are smaller in value than the magnetic inductances. The third factor in Eq. (18) is a ratio of the number of Cooper pairs broken by a photon divided by the total number of Cooper pairs in the detector. For a 0.1-eV phonon and a YBCO QSKID $50 \times 50 \mu\text{m}$ in area 50 nm thick with a Cooper

pair density of $7 \times 10^{20} \text{ cm}^{-3}$, this term can be estimated equal to 10^{11} . Combining all these approximations, the expression for the responsivity reduces to

$$\mathfrak{R}(\text{webers/watt}) \cong 0.5 \times 10^{11} I_0 \tau_{\text{eff}} \mathcal{L}_1. \quad (19)$$

It is evident that the responsivity is directly proportional to the QSKID bias current I_0 , the effective quasiparticle lifetime τ_{eff} , and the kinetic inductance \mathcal{L}_1 . Substituting reasonable values for $I_0 \approx 1 \text{ A}$ and $\mathcal{L}_1 \approx 2 \text{ nH}$, the responsivity simplifies to $\mathfrak{R} \approx 700 \tau_{\text{eff}}$. Because I_0 is below the superconductors critical current, no power is dissipated by the QSKID. The estimated quasiparticle lifetime (see Sec. 2.4) is greater than $10 \text{ } \mu\text{s}$ at 10 K considering phonon trapping effects in the film. For these values, the responsivity conservatively computes to about 10^{-4} Wb/W at 10 K . This can readily be detected by a SQUID circuit.

2.4 Quasiparticle Lifetime

The photoresponse¹³ of YBCO and Nb were measured with the transient photoimpedance response (TPR) method¹⁴ to observe the nonequilibrium photoresponse¹⁵ of superconductors, and in particular to estimate the duration of the nonequilibrium excitation's lifetime. Laser pulses of 300 fs at 665 nm were used to study nonequilibrium excitation lifetimes from the photoinduced impedance transient that appears as a voltage signal across the films. From the amplitude and temporal dependence of the TPR signal, the thermalization process was studied in superconductors in the normal, transition, and superconducting states. The temporal dependence of the thermalization process forms the basis for our rough estimation of quasiparticle lifetime and the viability of the QSKID.

The TPR photoresponse clearly demonstrated that the duration of the photoinduced nonequilibrium was dominated by extrinsic quasiparticle lifetime effects. Specifically, phonon trapping in the thin-film samples significantly increased the quasiparticle recombination lifetime over intrinsic values. This was particularly evident from TRP measurement in the normal state where the signals were bolometric in origin and phonon trapping governed the photoresponse lifetime. Phonon trapping in thin films ($< 80 \text{ nm}$) resulted in thermalization lifetimes much greater than several nanoseconds. These lifetimes were longer than anticipated from a simple acoustic boundary mismatch model by at least an order of magnitude. A nonideal boundary between substrate and thin film and the slower velocity expected for energetic Debye phonons in YBCO help to explain the observed long thermalization lifetimes. It is important to stress that, in the superconducting state, the quasiparticle lifetime will be also governed by phonon trapping, and we infer from the data that their lifetime will be much larger than 10 ns . Clearly the net recombination of quasiparticles cannot occur faster than the escape time for phonons from the film into the substrate or the anharmonic phonon decay lifetime. The normal state measurements put a lower limit on the phonon escape time. However in the superconducting state the phonon trapping time is further lengthened by quasiparticle excitations.

In the superconducting state, the excess energy being thermalized is shuttled back and forth between creating phonons and exciting quasiparticles. This excess energy can be removed from the film only by phonon emission into the sub-

strate or anharmonic phonon decay. The energy stored in quasiparticles cannot be removed from the film via quasiparticle emission into the substrate because of their different band gap structures. Thus during the time the excess energy is stored in quasiparticle excitations no excess energy escapes into the substrate. At lower temperatures, typically the quasiparticle generation lifetime τ_B is much shorter than the quasiparticle recombination lifetime τ_R . Therefore, the excess energy is, most of the time, in the form of excited quasiparticles. Because the excess energy can escape into the substrate only through phonons, the storage of this excess energy in the form of quasiparticles effectively increases the phonon trapping time. According to Rothwarf and Taylor,¹⁶ the effective lifetime τ_{eff} for quasiparticle recombination can be related to the phonon trapping time (τ_γ) and the intrinsic quasiparticle generation and recombination lifetimes as

$$\tau_{\text{eff}} = \tau_R + \tau_\gamma \left(\frac{\tau_R}{\tau_B} \right). \quad (20)$$

Because $\tau_R > \tau_B$, the effective recombination time for quasiparticles should be longer than the thermalization time constant τ_γ for the normal state, see Eq. (20). From our measurement of the normal and superconducting state responses, it is evident that quasiparticle lifetimes much longer than 10 ns are likely. Calculations indicate that the quasiparticle lifetimes at 10 K may in fact be much greater than $10 \text{ } \mu\text{s}$.

2.5 QSKID Readout Circuit

The QSKID readout circuit senses the magnetic flux produced by the photoinduced current circulating in the square loop (see Fig. 2). For achieving the highest sensitivity, a SQUID is used to sense the photoinduced magnetic flux. In the detector currently under development, the SQUID is made up of two niobium tunnel junctions. The QSKID structure is equally compatible with a SQUID readout circuit made from YBCO weak links. For best sensitivity, the SQUID readout circuit should be well coupled to the flux produced by the QSKID, and this is achieved by integrating the QSKID and SQUID on a single substrate. The responsivity of the QSKID is about 10^{-4} Wb/W or about $0.5 \cdot 10^{11} \Phi_0/\text{W}$, a quantity readily detected by a SQUID.

3 Conclusions

For operation at cryogenic temperatures, excellent semiconductor quantum detectors are available. Intrinsically, quantum detectors are more sensitive than bolometers. Thus, if superconducting detectors are to displace existing semiconductor-based quantum detectors, they need to offer improved performance, possible only by developing QSKID and not superconducting bolometers. Such a superconducting quantum detector has been introduced and its operation described. The projected responsivity is calculated for a SQUID readout circuit. The QSKID is a broadband detector with a response extending beyond $\lambda \approx 20 \text{ } \mu\text{m}$ and consumes very little power. These performance features are not available with semiconducting detectors. Ongoing developments on the theoretical and experimental front should provide, in the near future, answers to the ultimate performance of the QSKID. The information presented represents a starting point in the development of a new superconducting detector structure.

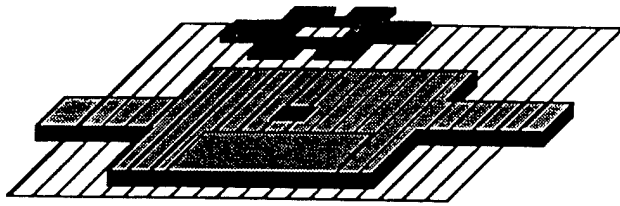


Fig. 2 QSKID with a SQUID readout circuit. The QSKID detector, represented by the bottom square loop, is overlaid by a light shield and an insulator. The topmost layer corresponds to the SQUID readout circuit, drawn enlarged. The actual size of the SQUID readout circuit is much smaller than the size of the QSKID detector.

Acknowledgments

This research and development has been supported by Westinghouse IR&D under task No. Z61601EHAA, the Naval Research Laboratory under contract No. N0014-92-C-2033, and the Ballistic Missile Defence Organization/Innovative Science & Technology Office under contract No. DASG60-92-0140.

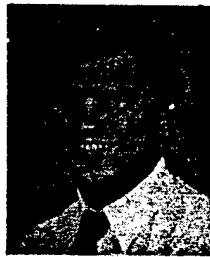
References

1. J. G. Bednorz and K. A. Muller, "Possible high T_c superconductivity in the Ba-La-Cu-O system," *Z. Phys. B* **64**, 189-193 (1986); "Peculiarities of the Ba-La-Cu-O system—The new approach to high- T_c superconductivity," *Rev. Mod. Phys.* **60**, 585-600 (1988).
2. Y. Enomoto and T. Murakami, "Optical detector using superconducting $\text{BaPb}_{0.7}\text{Bi}_{0.3}\text{O}_3$," *J. Appl. Phys.* **59**(11), 3807-3814 (1986).
3. H. S. Kwok, J. P. Zheng, and Q. Y. Ying, "Nonthermal optical response of Y-Ba-Cu-O thin films," *Appl. Phys. Lett.* **54**, 2473-2475 (1989).
4. M. Leung, P. R. Broussard, J. H. Claassen, M. Osofsky, S. A. Wolf, and U. Strum, "Optical detection in thin granular films of Y-Ba-Cu-O at temperatures between 4.2 and 100 K," *Appl. Phys. Lett.* **51**, 2046-2049 (1987).
5. W. S. Brocklesby, D. Monroe, A. F. J. Levi, M. Hong, S. H. Liou, J. Kwo, C. E. Rice, P. M. Mankiewicz, and R. E. Howard, "Electrical response of superconducting $\text{YBa}_2\text{Cu}_3\text{O}_{7.8}$ to light," *Appl. Phys. Lett.* **54**, 1175-1177 (1989).
6. M. G. Forrester, M. Gottlieb, J. R. Gavaler, and A. I. Braginski, "Optical response of epitaxial and granular films of $\text{YBa}_2\text{Cu}_3\text{O}_{7.8}$ at temperatures from 25 K to 100 K," *IEEE Trans. Magnet.* **25**, 1327-1330 (1989).
7. R. A. Smith, F. E. Jones, and R. P. Chasmar, *The Detection and Measurement of Infra-red Radiation*, p. 206, Clarendon Press, Oxford (1958).
8. P. W. Kruse, L. D. McGlauchlin, and R. B. McQuistan, *Elements of Infrared Technology: Generation, Transmission, and Detection*, p. 354 John Wiley & Sons, New York (1962).
9. A. M. Kadin, M. Leung, A. D. Smith, and J. M. Murruck, "Nonbolometric infrared detection in thin superconducting films via photo-production of fluxon pairs," *IEEE Trans. Magnet.* **27**, 1540-1543 (1991).
10. R. Kaplan, W. E. Carlos, and E. J. Cukauskas, "Microwave detected optical response of $\text{YBa}_2\text{Cu}_3\text{O}_{7-x}$ thin films," *J. Appl. Phys.* **67**(9), 4212-4216 (1990).

11. E. K. Track, M. Radparvar, and S. M. Faris, "Modulation of the penetration depth of Nb and NbN films by quasiparticle injection," *IEEE Trans. Magnet.* **25**, 1096-1099 (1989).
12. N. Bluzer, "Multispectral superconductive quantum detector," U.S. Patent No. 5,179,072 (Jan. 12, 1993) and "Multispectral superconductive quantum detector," U.S. Patent No. 5,185,527 (Feb. 9, 1993).
13. N. Bluzer, "Temporal relaxation of nonequilibrium in YBCO measured from transient photoimpedance response," *Phys. Rev. B* **44**, 10222-10232 (1991); "Temporal relaxation of photoinduced nonequilibrium in niobium," *Phys. Rev. B* **46**, 1033-1042 (1992).
14. N. Bluzer, "Temporal relaxation of photoinduced nonequilibrium in superconductors," *J. Appl. Phys.* **71**, 1336-1348 (1992).
15. N. Bluzer, "Biexponential decay and delay artifacts in the photoresponse of superconductors," *IEEE Trans. Appl. Supercond.* **3**(1), 2869-2872 (1993).
16. A. Rothwarf and B. N. Taylor, "Measurements of recombination lifetime in superconductors," *Phys. Rev. Lett.* **19**, 27-30 (1967); also see W. H. Parker, "Modified heating theory of nonequilibrium superconductors," *Phys. Rev. B* **12**, 3667-3672 (1975).



Nathan Bluzer is a senior advisory physicist at the Westinghouse Advanced Technology Laboratories, Linthicum, Maryland. He received his BS degree in electrical engineering with honors and a PhD degree in solid state physics from the University of Maryland, College Park. He was a visiting scholar at Stanford University studying high-temperature superconductivity. For more than 20 years Bluzer has had a key role in the research and development of high-speed CCDs, imaging CCDs, radiation hard CCDs, multiplexers, and detectors for IR sensors. The Maryland Academy of Sciences has recognized his original work and awarded him Maryland's 1990 Outstanding Young Engineer Award. Currently, he is responsible for the development of multispectral superconducting detectors. Bluzer has published more than 40 papers and has 30 U.S. patents granted and/or pending. He is a member of TB π , a fellow of the IEEE, and a life member of APS.



Martin G. Forrester received his BS in physics from the Massachusetts Institute of Technology in 1981 and his PhD in physics from Harvard University in 1987, completing his thesis on the properties of 2-D arrays of Josephson junctions. Since joining the staff of the Cryoelectronics Group at the Westinghouse Science and Technology Center in 1987, he has worked in the area of IR and digital electronic applications of superconductivity. His work has included the investigation of the response of high-temperature superconductors to visible and IR radiation, and in particular the understanding of the response in the context of thermal versus non-equilibrium models. He is currently pursuing the development of high-temperature superconducting Josephson junctions for both IR and digital circuit applications. Dr. Forrester has authored 30 papers on superconducting materials and devices. He is a member of the Materials Research Society and the American Physical Society.

Superconducting Quantum Detectors in YBCO

Nathan Bluzer¹ and Martin G. Forrester²

Received 31 July 1993

The discovery of high-temperature superconductors has led to great efforts to find potential applications, including the development of photon detectors. We review the limitations of the different approaches proposed for realizing superconducting photon detectors. The structure and operation of a new quantum superconducting kinetic inductance detector (QSKID) with a SQUID readout circuit is described. The QSKID is made from a superconducting loop where the photosignals are generated in response to photoinduced changes in the condensate's kinetic inductance. The QSKID operates in the zero-resistance superconducting state, thereby circumventing Johnson noise.

KEY WORDS: HTS; photodetector; quantum detector; kinetic inductance.

1. INTRODUCTION

The discovery of high-temperature superconductivity (HTS) by Bednorz and Muller [1] in 1986 evoked proposals for making IR photon detectors in HTS. These proposals were offered because IR detectors, like HTS, operate at liquid-nitrogen temperatures. Enomoto and Murakami [2] made photoresponse measurements on granular $\text{BaPb}_{0.7}\text{Bi}_{0.3}\text{O}_3$ and reported encouraging results. Soon, more papers [3–5] followed, reporting on the photoresponse of different HTS detector structures. After much analysis, it was recognized [6] that the reported photoresponse signals were consistent with a bolometric process. This was discouraging because the sensitivity [7,8] of bolometric detectors is less than the sensitivity of quantum detectors. However, because of technological limitations in semiconducting quantum detectors, the search for a superior superconducting quantum detector continues. In this paper, we report on the limitations of different published approaches toward realizing HTS superconducting detectors and an approach to realizing a HTS quantum detector.

¹Westinghouse Advanced Technology Laboratories, Winterson and Nursery Roads, Linthicum, Maryland 21090.

²Westinghouse Science and Technology Center, 1310 Beulah Road, Pittsburgh, Pennsylvania 15235-5098.

2. CONVENTIONAL SUPERCONDUCTING DETECTORS

Semiconducting and superconducting detectors can be grouped into two main categories: quantum and bolometric (or thermal) detectors. The detectors realized in LTS and HTS materials can be classified into the aforementioned categories. Other exotic mechanisms of detection, such as photon-induced vortex-antivortex nucleation, and photon-enhanced flux flow, have been proposed [9] but are not well understood vis-a-vis the four conventional detector approaches enumerated below.

- I. Thermal detectors, where the photoabsorbed energy changes the lattice temperature and some electronic property of the material, such as resistance. LTS and HTS transition edge bolometers have a sensitivity limited by the energy fluctuations of the lattice temperature and the photon flux. These detectors are attractive for very long wavelength ($>20 \mu\text{m}$) applications where semiconductor-based detectors require cooling to liquid-helium temperatures.
- II. Josephson-effect based detectors are particularly useful for millimeter and submillimeter wave detection. These devices use the nonlinear interaction between the incident

photons and the high-frequency oscillating currents and voltage, in a biased Josephson junction, to perform millimeter wave mixing and direct detection.

- III. Quasiparticle tunneling devices such as S-I-S mixers and direct detectors, where the incident photons are absorbed by quasiparticles, allowing tunneling events which would otherwise be energy-forbidden to affect the junction I - V characteristics.
- IV. Pair-breaking detectors, where incident photons (with energy larger than the energy gap) break Cooper pairs, leading to changes in such macroscopic parameters as the superconducting gap and the kinetic inductance. In these detectors photoabsorption is by quantum excitations.

The basic requirement for a superconducting quantum detector are: (1) quantum excitations to create excess quasiparticles by breaking Cooper pairs with photons that have an energy greater than 2Δ , and (2) efficient detection of the excess quasiparticles by measuring a property sensitive to the condensate population. Properties sensitive to the quasiparticle (or condensate) population include the voltage across a series of weak links, the superconductor's microwave surface resistance, or the superconductor's kinetic inductance.

In granular HTS films, the voltage signals are induced by laser radiation that locally suppresses the gap and the intergranular critical current. Only those quasiparticles created within a distance of the order of the coherence length ξ from the grain boundaries produce a voltage signal. The *area efficiency* of a granular HTS detector is expressed (in 2D) as the ratio of the coherence length to the average grain size, L_g , squared. For a typical granular YBCO film, this area efficiency ratio $(\xi/L_g)^2$ is of the order 10^{-7} . This is an extremely poor area efficiency and equivalent to a very poor quantum efficiency, incompatible with high-performance detectors.

The poor area efficiency in granular HTS detectors can be overcome with microwave readout circuits which are sensitive to the entire quasiparticle or condensate population, such as changes in the microwave reflectivity [10] and resonator Q produced with photoabsorption. The microwave readout circuit's size is much larger than a typical pixel size, about $50 \times 50 \mu\text{m}^2$. Thus, such a readout approach is not practical nor compatible with the development of dense two-dimensional arrays.

Another method sensitive to photoinduced changes in the condensate population is the voltage vs. flux signal of the superconducting film incorporated into a SQUID loop. Biasing this SQUID loop in the voltage state, photodepairing changes the condensate's kinetic inductance, resulting in a voltage signal, derived from the SQUID's periodicity with flux. The period of the SQUID's threshold characteristic with applied flux is given by Φ_0/L , where Φ_0 is the flux quantum and L is the total inductance, equal to the sum of the geometrical and kinetic inductances in the SQUID loop [11]. Such a detector must operate in the voltage state, and calculations reveal a sensitivity severely limited by the SQUID's noise characteristics, resulting in poor detectivity.

To realize sensitive (low-noise) detectors, it is critical that the LTS or HTS detectors operate in the current and not voltage state. This detector needs to be sensitive to photoinduced changes in the condensate, e.g., sensitive to the condensate's kinetic inductance \mathcal{L} . With such an approach, the detector remains in the superconducting current state (low noise), and changes in its kinetic inductance are monitored as a change in the magnetic field, as detailed in the next section.

3. QUANTUM SUPERCONDUCTING KINETIC INDUCTANCE DETECTORS

A viable QSKID needs to operate in the superconducting current state to achieve low-noise performance. For maximum photoresponse, long quasiparticle photoexcitation lifetimes are necessary. The QSKID's read-out circuit must be simple, specifically a SQUID circuit. The QSKID structure compatible with the aforementioned objectives includes: (a) no weak links, facilitating low noise and manufacturability, (b) maximum photoresponse and NEP by operation in the zero-resistance superconducting state, (c) multispectral response from UV to the far infrared ($\lambda_c > 20 \mu\text{m}$), and (d) structure compatible with a 100% fill factor. Meeting these objectives is necessary to produce a viable QSKID with a performance superior to competing semiconductor quantum detectors. Such a detector structure has been formulated [12] and is schematically illustrated in Fig. 1 by a single superconducting loop. No weak links are used, and the output signal is the magnetic flux produced by the circulating current in the loop. Details on the QSKID's operation are given next.

The division of current $I_0 < I_c$ into currents I_1 and I_2 satisfies an energy minimum [12,13] and the single-valuedness for the condensate wave function,

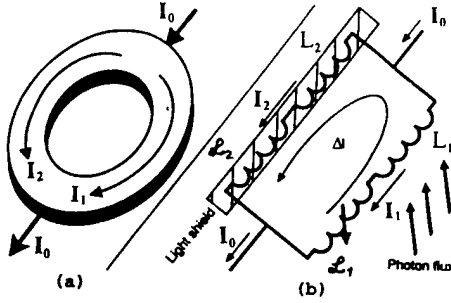


Fig. 1. The QSKID (a) and its equivalent circuit (b) consists of superconducting loop biased with a dc current I_0 , with magnetic (L) and kinetic (\mathcal{L}) inductances. Bias current I_0 splits between branches 1 (I_1) and 2 (I_2) of the superconducting loop. For identical branches $I_1 = I_2$. Photodepairing only in branch 1 changes the kinetic inductance ($\delta\mathcal{L}_1$) and gives rise to a circulating photocurrent ΔI , producing a detectable magnetic field. A small SQUID placed (not shown) over the opening in the QSKID detects the photoinduced magnetic flux.

expressed by a complex quantity $\psi(x) = \sqrt{n(x)} e^{i\phi}$. We calculate the current division by requiring a single-valued $\psi(x)$, and the result is consistent with energy minimization requirements. At any point x inside the superconductor, the density of Cooper pairs is given by $n(x)$, where $n(x) = \psi^*(x)\psi(x)$. Writing out explicitly the condensate's phase gradient $\nabla\phi$, we obtain

$$\nabla\phi = \frac{2\pi}{\Phi_0} \left(\bar{A} + \frac{m}{2e^2 n} \bar{J}_s \right) \quad (1)$$

where, $\Phi_0 = h/2e$, \bar{A} is the vector potential, and \bar{J}_s is the supercurrent density. In superconducting films thinner than the London penetration depth, the supercurrent \bar{J}_s does not vanish anywhere inside the QSKID loop, and $\psi(x)$ is single-valued. The line integral in Eq. (1), after some simplifications, yields

$$\int_S \bar{B} \cdot d\bar{S} + \oint \frac{m}{2e^2 n} \bar{J}_s \cdot d\bar{l} = N\Phi_0 \quad (2)$$

where \bar{B} is the magnetic field inside the detector's loop and \bar{S} is the area enclosed by the integration curve. Completing the integration in Eq. (2), we obtain

$$L_1 I_1 - L_2 I_2 + \mathcal{L}_1 I_1 - \mathcal{L}_2 I_2 = N\Phi_0 \quad (3)$$

where the four coefficients $\mathcal{L}_1(L_1)$ and $\mathcal{L}_2(L_2)$ are the kinetic (magnetic) inductances of branch 1 and 2, respectively. The kinetic inductance of each branch expressed in terms of the Cooper pair's mass ($2m$), charge ($2e$), the branch length (l), with cross sectional

area (a) is

$$\mathcal{L} = \left(\frac{l}{a} \right) \frac{m}{2e^2 n} \quad (4)$$

In a QSKID with a symmetrical geometry shielded from external fields and not subjected to any illumination, the net enclosed flux is zero [the right side of Eq. (3) is zero] and no current circulates, $I_1 = I_2 = I_0/2$. Illuminating only branch number 1 in Fig. 1 changes $\delta\mathcal{L}_1$. The change in $\delta\mathcal{L}_1$ that will produce a circulating current ΔI , obtained by taking the differential of Eq. (3), is

$$\Delta I_1 = -I_1 \frac{\delta\mathcal{L}_1}{(L_1 + \mathcal{L}_1 + L_2 + \mathcal{L}_2)} \quad (5)$$

The circulating current ΔI produces a magnetic field \bar{B}_{QSKID} and flux $\Phi = \Delta I(L_1 + L_2)$, which is a measure of the absorbed photon flux Φ_{ph} . The QSKID's responsivity \mathfrak{R} (Webers/watt) (dependent on the flux Φ_{ph} , changes in \mathcal{L}_1 , and number of broken pairs n_1) is

$$\delta\mathcal{L}_1 = \left(\frac{\partial\mathcal{L}_1}{\partial n_1} \right) \left(\frac{\partial n_1}{\partial \Phi_{\text{ph}}} \right) \Phi_{\text{ph}} = -\frac{\mathcal{L}_1}{n_1} \left(\frac{\eta \tau_{\text{eff}}}{d} \right) \Phi_{\text{ph}} \quad (6)$$

where n_1 , η , τ_{eff} , and d are, respectively, the Cooper pair density, the number of pairs broken by a photon, the effective quasiparticle lifetime, and the detector thickness. The incident power P on the detector, with an optical area A_λ , is

$$P = A_\lambda \Phi_{\text{ph}} h\nu \quad (7)$$

Combining Eqs. (5) and (6), multiplying by $(L_1 + L_2)$, and dividing by 7, the computed QSKID's responsivity \mathfrak{R} (Webers/watt) becomes

\mathfrak{R} (Webers/watt)

$$= I_1 \left(\frac{L_1 + L_2}{L_1 + \mathcal{L}_1 + L_2 + \mathcal{L}_2} \right) \left(\frac{\eta}{A_\lambda n_1 d} \right) \left(\frac{\mathcal{L}_1 \tau_{\text{eff}}}{h\nu} \right) \quad (8)$$

The first factor is the bias current I_1 flowing through the illuminated branch, and for a balanced detector it is equal to $I_0/2$. The second factor, the ratio of inductances, is equal to about unity, because $\mathcal{L}_1 \approx L_1$ and $\mathcal{L}_2 \approx L_2$. The third factor, for a 0.1-eV photon and a YBCO QSKID $50 \mu\text{m} \times 50 \mu\text{m}$ in area and 160 nm thick with a Cooper pair density of $\approx 10^{20} \text{ cm}^{-3}$, is estimated to be 2×10^{-11} . Combining all these, the expression for the responsivity reduces to

$$\mathfrak{R} \text{ (Webers/watt)} \cong 10^8 I_0 \tau_{\text{eff}} \mathcal{L}_1. \quad (9)$$

The responsivity is proportional to the QSKID bias current I_0 , the effective quasiparticle lifetime τ_{eff} , and the kinetic inductance \mathcal{L}_1 . Substituting values for $I_0 \approx 0.1$ A and $\mathcal{L}_1 \approx 2$ nH, the responsivity simplifies to $\mathfrak{R} \approx 0.02 \tau_{\text{eff}}$. Since I_0 is below the superconductor's critical current, no power is dissipated by the QSKID. The estimated quasiparticle lifetime [14,15] is about 10 msec at 10 K, considering phonon trapping effects in the film. For these values the responsivity conservatively computes to about 10^{-4} Webers/Watt at 10 K. This can readily be detected by a SQUID circuit with a sensitivity of $\approx 10^{-21}$ Webber/ $\sqrt{\text{Hz}}$.

The QSKID read-out circuit senses the magnetic flux produced by the photoinduced current circulating in the loop (see Fig. 1). A SQUID is used to sense the photoinduced magnetic flux. In the QSKID under development, the SQUID is made up of two niobium tunnel junctions or YBCO weak links. For best sensitivity, the SQUID read-out circuit should be well coupled to the flux produced by the QSKID, integrating the QSKID and SQUID on a single substrate. The responsivity of the QSKID is about 10^{-4} Webers/Watt or about 0.5×10^{11} Φ_0 /Watt, a quantity readily detected by a SQUID, yielding an NEP $\approx 10^{-17}$ Watt/ $\sqrt{\text{Hz}}$.

4. CONCLUSIONS

Excellent semiconductor quantum detectors are available for operation at cryogenic temperatures. Intrinsically, quantum detectors are more sensitive than bolometers. Thus, if superconducting detectors are to replace existing semiconducting quantum detectors, they need to offer improved performance, possible only by developing QSKID and not superconducting bolometers. A superconducting quantum detector, with a SQUID read-out circuit, is

introduced and its operation is described. The QSKID projected responsivity is calculated. The QSKID is a multispectral detector with a response extending beyond $\lambda \approx 20$ μm and consumes very low power.

ACKNOWLEDGMENTS

This research was supported by Westinghouse IR&D under task Z61601EHAA, the Naval Research Laboratory under tasks No. N0014-92-C-2033, and the Ballistic Missile Defence Organization/Innovative Science & Technology Office under task No. DASG60-92-0140.

REFERENCES

1. J. G. Bednorz and K. A. Muller, *Z. Phys. B* **64**, 189 (1986); *Rev. Mod. Phys.* **60**, 585 (1988).
2. Y. Enomoto and T. Murakami, *J. Appl. Phys.* **59**, 3807 (1966).
3. H. S. Kwok, J. P. Zheng, and Q. Y. Ying, *Appl. Phys. Lett.* **54**, 2473 (1989).
4. M. Leung, P. R. Broussard, J. H. Claassen, M. Osofsky, S. A. Wolf, and U. Strum, *Appl. Phys. Lett.* **51**, 2046 (1987).
5. W. S. Brocklesby, D. Monroe, A. F. J. Levi, M. Hong, S. H. Liou, J. Kwo, C. E. Rice, P. M. Mankiewicz, and R. E. Howard, *Appl. Phys. Lett.* **54**, 1175 (1989).
6. M. G. Forrester, M. Gottlieb, J. R. Gavalier, and A. I. Braginski, *IEEE Trans. Magn.* **MAG-25**, 1327 (1989).
7. R. A. Smith, F. E. Jones, and R. P. Chasmar, *The Detection and Measurement of Infra-red Radiation* (Oxford University Press, New York, 1958), p. 206.
8. P. W. Kruse, L. D. McGlauchlin, and R. B. McQuistan, *Elements of Infrared Technology: Generation, Transmission, and Detection* (J. Wiley, New York, 1962), p. 354.
9. A. M. Kadin, M. Leung, A. D. Smith, and J. M. Murduck, *IEEE Trans. Magn.* **27**, 1540 (1991).
10. R. Kaplan, W. E. Carlos, and E. J. Cukauskas, *J. Appl. Phys.* **67**, 4212 (1990).
11. E. K. Track, M. Radparvar, and S. M. Faris, *IEEE Trans. Magn.* **MAG-25**, 1096 (1980).
12. N. Bluzer, United States Patents 5,179,072 and 5,185,527.
13. N. Bluzer and M. G. Forrester, Proceedings of the SPIE conference, San Diego, California, July 11-16, 1993.
14. N. Bluzer, *Phys. Rev. B* **44**, 10222 (1991); N. Bluzer, *Phys. Rev. B* **46**, 1033 (1992).
15. N. Bluzer, *J. Appl. Phys.* **71**, 1336 (1992); *IEEE Trans. Appl. Supercond.* **3**, 2869 (1993).

Quantum Detectors in Superconducting YBCO*

Nathan Bluzer

Westinghouse Advanced Technology Labs., Winterson & Nursery Rds., Linthicum, MD 21090 USA

Martin G. Forrester

Westinghouse Science and Technology Center, 1310 Beulah Rd., Pittsburgh, PA 15235 USA

Abstract---A superconducting quantum detector structure in YBCO is described with a directly coupled SQUID read out circuit. The detector geometry is optimized for maximum photoresponse with the use of a serpentine pattern. The serpentine pattern reduces quasiparticle diffusion effects and maximizes the photoinduced changes in the kinetic inductance. The operation of this sensor is analyzed in terms of geometry and quasiparticle lifetime to obtain expressions for the signal and noise of this detector. The background limited infrared performance of this detector is calculated to be about 5×10^{-17} NEP. The photoresponse is expected to be limited by the superconducting energy gap, about 30-40 μ m.

I. INTRODUCTION

Since the discovery of High Temperature Superconductivity (HTS) by Bednorz and Muller [1] many proposals were offered for fabricating Infrared (IR) detectors in HTS. Enomoto and Murakami [2] measured the photoresponse in $\text{BaPb}_{0.7}\text{Bi}_{0.3}\text{O}_3$ and reported encouraging results. Many more photoresponse measurements were reported on HTS, however it was shown by Forrester et al. [3] that the results reported were consistent with a bolometric and not a quantum (or photon) detector response. This was disappointing for it has been long recognized that theoretically above 1K quantum detectors offer superior sensitivity over bolometric detectors [4]. Hence the expectation of replacing semiconductor based quantum detectors by bolometric superconductor based detectors was unreasonable. If superconducting detectors are to compete with semiconducting quantum detectors, superconducting detector structures are needed which provide photon noise limited performance.

At Westinghouse we have been pursuing, for several years, the development of superconducting quantum detectors. The superconducting quantum detectors are intended for imaging applications. In such applications the detector integration times are from several μ sec to several msec long. And thus we alleviate the need for very fast readout circuits and very fast photoresponse

measurements to short laser pulses. The detectors are intended to operate in the superconducting current state (zero voltage) under static nonequilibrium conditions and in the Meissner state (below H_{C1}), to circumvent noise from fluxoid formations and movement. The detectors' performance is dependent on the quasiparticle lifetimes and these lifetimes are maximized as the detectors' operating temperature is lowered significantly below the superconducting transition temperature T_C . Additionally, the approach selected [5] does not use weak-links in the detector structure and thereby maximizes the quantum efficiency, and reduce the fabrication difficulties associated with making weak-links in YBCO. Weak-link based detectors are only sensitive to photoexcitations that occur within several coherence lengths ξ from the weak-link. Thus for good quantum efficiency, many weak-links need within each detector pixel because $\xi \approx 1.5$ nm is many times smaller than the typical detector pixel, 25-100 μ m. The use of many weak-links for each detector imposes severe fabrication yield problems as well as sensitivity issues. Hence we have selected a simpler detector and readout approach for realizing superconducting quantum sensors.

II. SUPERCONDUCTING SENSOR

The superconducting quantum detector we are developing are based on the condensate's kinetic inductance and the changes in this kinetic inductance produced by photodepairing of Cooper pairs. Generically, the structure of Quantum Superconducting Kinetic Inductance Detector (QSKID) is shown in Fig. 1, where a thin (less than a London penetration depth) superconducting closed loop, operating in the current and Meissner states, divides a DC current $I_0 = I_L + I_R$ into a left branch current I_L and a right branch current I_R . The current division satisfies the Hamiltonian's minimum energy conditions [5][6] and is expressed by Equation 1 as:

$$L_L I_L = L_R I_R \quad (1)$$

Where the L_L and L_R are the total inductance terms for the left and right branches, respectively. The total inductance of a branch includes: the geometrical (or

* Manuscript received October 17, 1994. This work was supported by: the Naval Research Labs. under contract # N0014-92-C-2033, Innovative Science and Technology Office through the Army contract # DASG60-92-0140, and Westinghouse IR&D under task Z61601EHAA.

magnetic field) self inductance, the interbranch mutual inductance, and the kinetic inductance. For example, the total left branches inductance $L_L = L_{LG} - L_{LM} + L_{LK}$ includes the geometrical self inductance L_{LG} , the mutual inductance between the left and right branches (with negative coupling) L_{LM} , and the kinetic inductance L_{LK} .

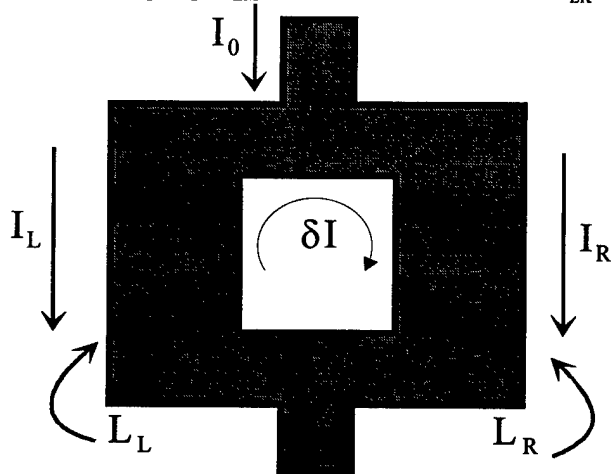


Figure 1. The generic diagram of a QSKID consisting of a superconducting loop dividing a DC current I_0 into I_L and I_R . Only one branch, the left, e.g., is exposed to a photon flux while the other is shielded. Changes in the kinetic inductance of the exposed branch causes a circulating current δI .

A photon flux Ψ on the left branch breaks up Cooper pairs and produces a decrease in the Cooper pair density ρ_L . The kinetic inductance $L_{LK} = [I_L m_{CP}] / [S_L q_{CP}^2 \rho_L]$ is inversely dependent on ρ_L , the length of the left branch I_L , the mass of a Cooper pair m_{CP} , the cross sectional area of the left branch S_L , and the Cooper pair charge q_{CP} squared. With photoabsorption the Cooper pair density in the exposed branch decreases and the kinetic inductance increases by ΔL_{LK} . The signal δI developed with photoabsorption in the left branch is calculated by taking the differential of Eq. 1 to obtain:

$$\delta I = \frac{\Delta L_{LK}}{(L_L + L_R)} \frac{I_0}{2} \quad (2)$$

The photoinduced signal δI depends on the QSKID geometry and quasiparticle lifetime and these are addressed below.

A. Detector Structure

With a serpentine geometry shown in Fig. 2 the performance of the QSKID is improved over the simple superconducting loop shown in Fig. 1. The improvements occur because for a given photon flux Ψ the change in ΔL_{LK} is larger and because improved isolation is achieved between the illuminated and masked branches

A serpentine geometry QSKID with N vertical segments in each branch, has the lengths of the left and right branches I_{SL} and I_{SR} increased about N times over a nonserpentine QSKID. For the QSKID in Fig. 2, $I_{SL} / I_L \approx 7$ and $I_{SR} / I_R \approx 7$. A similar scaling occurs for the left and right cross sectional areas S_{SL} and S_{SR} resulting in $S_{SL} / S_L \approx S_{SR} / S_R \approx 7$. Also the bias current I_0 decrease by a factor of 7, to provide a desirable reduction for operating integrated circuits. The serpentine geometry results in a significant increase in the kinetic inductance relative to the geometrical inductance. Combining all these factors, we calculate that for the serpentine QSKID under a given photon flux Ψ , the signal δI increases approximately 7 fold.

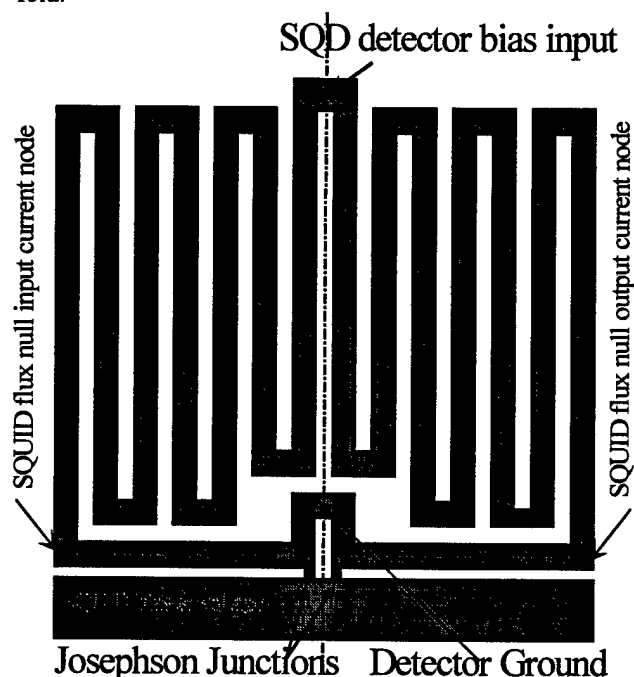


Figure 2. The YBCO superconducting quantum detector is shaped into a serpentine pattern with the directly coupled SQUID readout circuit located at the bottom. The photon flux only illuminates the left half of the serpentine patterned detector.

An additional benefit with the serpentine structure is interbranch isolation to maintain maximum signal. With photoillumination L_{LK} and the quasiparticle population increase. Interbranch quasiparticle and Cooper pair diffusion between the illuminated and the masked branches will reduce the signal. Interbranch diffusion is facilitated with quasiparticle having long lifetimes and this occur by phonon trapping and low temperature operation. For YBCO, the quasiparticle diffusion length is estimated to be: $2\mu\text{m}$ for 1nsec, $10\mu\text{m}$ for 10nsec, and $60\mu\text{m}$ for 1usec lifetimes respectively. These diffusion lengths are significant relative to the QSKID pixel size. A serpentine structure significantly increase the interbranch

path lengths and thereby resulting in improved interbranch isolation, i.e. less signal loss.

B. Detector's Photoresponse

Photoabsorption in the left branch of the serpentine QSKID in Fig. 2 produces a change in the inductance L_{1L} . The photoresponse is calculated in terms of the change in L_{1L} using the electrical equivalent circuit in Fig. 3. The equivalent circuit includes two loops each supplied with a DC current generator. The top loop, supplied by current I_0 , represents the serpentine detector structure. Below it, a second loop, supplied by a DC current I_{SQ} , represents the detector's SQUID readout circuit. Each inductor in the equivalent circuit includes: the self, the mutual, and the kinetic inductance terms associated with the structure in Fig. 2. The equivalent circuit is symmetrical and the left (right) side inductors and weak links are indicated by a subscript which includes the letter L (R).

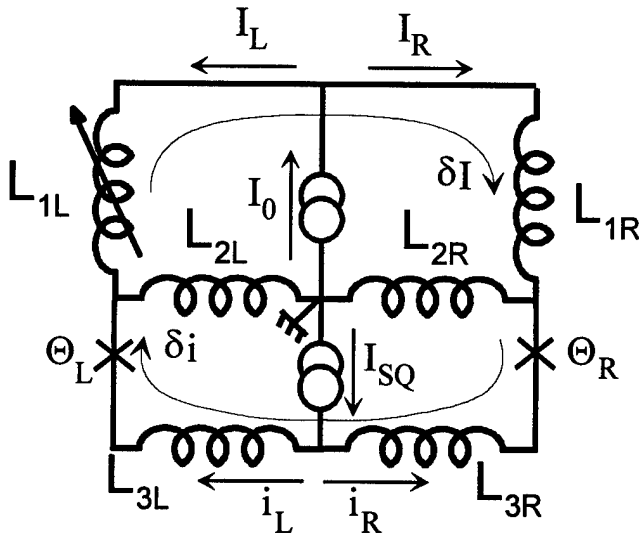


Figure 3. Equivalent circuit diagram for a directly coupled SQUID readout circuit to a YBCO superconducting quantum detector. There are two DC bias currents, one for the detector I_0 , and one for the SQUID readout device I_{SQ} .

The photoresponse is calculated by relating the photoinduced currents in the detector δI with the SQUID current δi . Before illumination, and under initial conditions, currents δI and δi are set equal to zero. Minimum energy conditions [5][6], represented by Eq. 1, yield the equilibrium conditions equation as:

$$I_L[L_{1L} + L_{2L}] + i_L L_{2L} = I_R[L_{1R} + L_{2R}] + i_R L_{2R} \quad (3)$$

The total SQUID loop inductance ($L_{2L} + L_{2R} + L_{3L} + L_{3R}$) is designed to be small to achieve good critical current modulation with flux. For QSKID with a large serpentine geometry results in $L_{1L} \gg L_{2L}$ and $L_{1R} \gg L_{2R}$. Therefore,

currents i_L and i_R are shunted to ground primarily through L_{2L} and L_{2R} , respectively, and we can neglect the flow of currents i_L and i_R through L_{1L} and L_{1R} . Integrating around the SQUID loop and requiring a zero or a multiple of 2π , the phase change, we obtain an equation for the SQUID under equilibrium conditions, i.e.

$$\frac{\Phi_0}{2\pi} \Theta_L + L_{3L} i_L + L_{2L} [I_L + i_L] = \frac{\Phi_0}{2\pi} \Theta_R + L_{3R} i_R + L_{2R} [I_R + i_{LR}] \quad (4)$$

Where Φ_0 is a fluxoid, Θ_L and Θ_R represent the phase shift across the left and right weak links.

With the application of a flux Ψ , photodepairing increases L_{1L} by δL and establishes new static conditions with currents δI and δi circulating in the detector and SQUID loops, respectively. Making the following substitutions in Eq. 3: $I_L = I_L + \delta I$, $I_R = I_R + \delta I$, $L_{1L} = L_{1L} + \delta L$, $i_L = i_L + \delta i$, $i_R = i_R + \delta i$, and keeping only first order terms, the nonequilibrium equation for the detector is:

$$\delta L I_L = \delta I [L_{1R} + L_{2R} + L_{1L} + L_{2L}] - \delta i [L_{2R} + L_{2L}] \quad (5)$$

Incorporating the same substitutions into Eq. 4 and keeping only the first order terms, the nonequilibrium equation for the SQUID becomes:

$$\frac{\Phi_0}{\pi} \delta \Theta + \delta i [L_{3R} + L_{3L} + L_{2L} + L_{2R}] = \delta I [L_{2R} + L_{2L}] \quad (6)$$

Eq. 5 is readily solved by recognizing that since $L_{1L} \gg L_{2L}$ and $L_{1R} \gg L_{2R}$ the last term can be neglected, and we obtain a solution similar to Eq. 2. Similarly, Eq. 6 is solved by recognizing that when operating in the voltage state, the leading term is the smallest since on average $\delta \Theta \approx 0$ and the phase angle across the weak link remains very close to $\pi/2$. Combining Eq. 5 and 6 we obtain a relationship between the SQUID and detector signal currents, specifically,

$$\delta i = \delta I \frac{[L_{2R} + L_{2L}]}{[L_{3R} + L_{3L} + L_{2L} + L_{2R}]} \quad (7)$$

The signal coupling efficiency between the QSKID's δI and the SQUID's δi is optimized by making the relative sizes of $[L_{3R} + L_{3L}] \ll [L_{2L} + L_{2R}]$. The detector

geometry, illustrated in Fig. 2, is designed for achieving a maximum coupling efficiency

The SQUID's voltage signal, produced by the QSKID's signal δI , is obtained from the RSJ model [7] [8] in the limit as the weak link's shunting capacitance C goes to zero. The SQUID's average output voltage signal δV , with weak links that each have an equivalent shunting resistance of R , is:

$$\delta V = \frac{\alpha R}{\sqrt{\alpha^2 - 1}} \frac{[L_{2R} + L_{2L}]}{[L_{3R} + L_{3L} + L_{2L} + L_{2R}]} \delta I \quad (8)$$

where $\alpha = I_{SQ}/2I_C$ and I_C is equal to the weak link's critical current. The sensitivity of the QSKID is examined next.

C. Detector's Sensitivity

Since the mechanism of HTS is not well understood, it is difficult to provide accurate predictions of static nonequilibrium phenomena in these materials. However, using the BCS model and the Rothwarf-Taylor equations, sensitivity predictions have been made. An extensive analysis has been made [9] [10] and here we shall only give highlights of these results

The noise in the QSKID, due to fluctuations in the Cooper pair population, is calculated to be much less than the Johnson noise in voltage state SQUID. The QSKID sensitivity is limited by: the current noise in the SQUID readout circuit. This noise can be minimized by using SQUIDS that have a smaller I_C and a larger loop inductance, but at the cost of noise rounding in the SQUID's I-V characteristics.

The photoresponse was modeled for Background (photon noise) Limited Infrared Performance (BLIP) where the photon noise is larger than the detector and readout circuit noises, added in quadrature. Hence, the ultimate performance level is achieved by minimizing the detector and the readout circuit noises. For BLIP, the photogenerated quasiparticle population needs to be larger than the thermal equilibrium quasiparticle population. Also, the detectors responsivity, dependent on the quasiparticle lifetime, needs to be maximized to overcome readout circuit noise. The δI is maximized by operating the detector at lower temperatures (30K e.g.) and utilizing phonon trapping to realize large effective quasiparticle lifetimes. In YBCO Pair Breaking (PB) phonon are trapped because anisotropy naturally confines the movement of PB phonons in the ab plane. Such phonon trapping is limited by anharmonic decay lifetime of PB phonons into non-pair breaking phonons.

We have calculated the BLIP sensitivity of a $100 \times 100 \mu\text{m}$ QSKID with a directly coupled SQUID readout circuit. The calculated sensitivity, for a $100 \mu\text{m}$ square detector operating in a 30Hz bandwidth, in terms of Noise Equivalent Power is about 10^{-16} - 10^{-17} Watts. This calculated level of performance is limited by the detector's SQUID readout circuit. The QSKID projected spectral response is limited by the Cooper pair binding energy, predicted for YBCO to be about $30 \mu\text{m}$

III. CONCLUSIONS

A QSKID structure with a directly coupled SQUID readout circuit were described and the performance analyzed. The operation of this sensor structure is based on photoinduced changes in the QSKID kinetic inductance. A serpentine pattern is used for maximizing the photoresponse. The detectors sensitivity is limited by the current noise in the directly coupled SQUID readout circuit. The predicted BLIP NEP is 10^{-16} - 10^{-17} Watts with a cut-off wavelength between 30 - $40 \mu\text{m}$. The predicted performance makes the QSKID attractive and competitive particularly for detection at very long IR wavelength of cold objects.

IV. REFERENCES

- [1] J. G. Bednorz and K. A. Muller, "Possible high T_C superconductivity in the Ba-La-Cu-O system," *Z. Phys. B.* vol. 64, pp 189-193, 1988.
- [2] Y. Enomoto and T. Murakami, "Optical detector using superconducting $\text{BaPb}_{0.7}\text{Bi}_{0.3}\text{O}_3$," *J. Appl. Phys.* vol. 59 No. 11, pp 3807-3814, 1986.
- [3] M. G. Forrester, M. Gottlieb, J. R. Gavaler, and A. I. Braginski, "Optical response of epitaxial and granular films of $\text{YBa}_2\text{Cu}_3\text{O}_{7.8}$ at temperatures from 25 and 100K," *IEEE trans. Magnet.* vol. 25, pp 1327-1330, 1989.
- [4] R. A. Smith, F. E. Jones, and R. P. Chasmar, *The Detection and Measurement of Infra-red Radiation*, Clarendon Press, Oxford 1958, pp 206-215.
- [5] N. Bluzer, "Multispectral superconducting quantum detector," U.S. Patent No. 5,179,072 (Jan. 12 1993) and 5,185,527 (Feb. 9, 1993).
- [6] N. Bluzer, and M. G. Forrester, "Superconducting quantum detectors" *J. Optical Engr.* vol. 33, No. 3, pp 697-703, March 1994; N. Bluzer and M. G. Forrester, "Superconducting quantum detectors in YBCO," *J. of Superconductivity*, vol. 7 No. 2, pp 395-398, 1994.
- [7] W. C. Stewart, "Current-voltage characteristics of Josephson junctions," *Appl. Phys. Lett.*, vol. 12, pp. 277-280, 15 April 1968.
- [8] D. E. McCumber, "Effects of ac impedance on the dc voltage-current characteristics of superconducting weak link junctions," *J. Appl. Phys.*, vol. 39, pp 3113-3118, June 1968.
- [9] N. Bluzer, "Quantum Superconducting Kinetic Inductance Detectors," unpublished.
- [10] A. V. Sergeev and M. Yu. Reizer, "Nonequilibrium Superconducting Detectors of Electromagnetic Radiation", unpublished.